Horizontal and vertical propagation of mountain waves from New Zealand into the polar night jet

Benedikt Ehard

München 2017

Horizontal and vertical propagation of mountain waves from New Zealand into the polar night jet

Benedikt Ehard

Dissertation
an der Fakultät für Physik
der Ludwig–Maximilians–Universität
München

vorgelegt von
Benedikt Ehard
aus Roth

München, den 03.03.2017

Erstgutachter: Prof. Markus Rapp
Zweitgutachter: Prof. Riwal Plougonven
Tag der mündlichen Prüfung: 04.05.2017

Zusammenfassung

Diese Dissertation untersucht die horizontale Ausbreitung von Gebirgswellen aus mittleren Breiten in der Südhemisphäre. Hierfür werden bodengebundene Temperaturmessungen eines Rayleigh Lidars analysiert, die in Lauder, Neuseeland, während des südhemisphärischen Winters durchgeführt wurden. Zuerst werden vier gebräuchliche Methoden zur Extraktion von Schwerewellen aus mittelatmosphärischen Temperaturmessungen mittels Lidar evaluiert und miteinander verglichen. Es stellt sich heraus, dass sich ein Butterworthfilter am besten eignet, wenn Gebirgswellen analysiert werden sollen. Als nächstes wird untersucht inwiefern das integrierte Vorhersagesystem (IFS) des europäischen Zentrums für mittelfristige Wettervorhersage (ECMWF) die Dynamik der mittleren Atmosphäre auflöst. Der mittlere thermische Zustand der Atmosphäre über Neuseeland wird dabei bis in 60 km Höhe korrekt simuliert, wohingegen die simulierten Schwerewellen nur bis in 45 km Höhe mit den Messungen übereinstimmen. Dies ist vor allem auf die Schwammschicht des ECMWF IFS zurückzuführen, die oberhalb von 45 km kleinskalige Fluktuationen in den Simulationen dämpft. Zum Schluss wird untersucht, ob die Gebirgswellen, die am 31. Juli und 1. August 2014 von dem Lidar beobachtet werden, sich horizontal ausbreiteten. Durch Kombination von Daten des bodengebundenen Rayleigh-Lidars, des ECMWF IFS und von Satelliten, sowie unter Zuhilfenahme von Ratracing Simulationen, kann gezeigt werden, dass die Gebirgswellen zu Beginn der hier analysierten Periode in der unteren Stratosphäre brechen. Zu einem späteren Zeitpunkt können die Gebirgswellen in größere Höhen propagieren und breiten sich auch horizontal Richtung Südosten aus. Ferner wird abgeschätzt, dass der Schwerewellenimpulsfluss der horizontal propagierenden Gebirgswellen in 70 km Höhe um eine Größenordnung größer ist als das klimatologische Mittel. Dies zeigt, dass der Impulsfluss von Gebirgswellen aus Neuseeland über mehrere Breitengrade hinweg transportiert werden kann.

Abstract

This thesis examines the horizontal propagation of mountain waves originating at mid-latitudes in the southern hemisphere. For this purpose, ground-based Rayleigh lidar temperature measurements are analyzed, which were conducted at Lauder, New Zealand, during austral winter. In a first step, four common methods of extracting gravity waves from middle atmospheric lidar temperature measurements are evaluated and compared to each other. It is found that the application of a Butterworth filter is suited best, if mountain waves are the focus of the study. Secondly it is evaluated in how far the integrated forecast system (IFS) of the European Centre for Medium-Range Weather Forecasts (ECMWF) resolves middle atmospheric dynamics. The mean thermal state of the atmosphere above New Zealand is thereby correctly simulated up to 60 km altitude, whereas the simulated gravity waves agree with the observations only up to 45 km altitude. This is attributed to the sponge layer of the ECMWF IFS, which dampens small scale fluctuations within the model above 45 km altitude. In a last step, it is analyzed whether mountain waves observed by the lidar on 31 July and 1 August 2014 propagated horizontally. By combining the Rayleigh lidar data with ECMWF IFS data, satellite data and raytracing simulations, it is found that in the beginning of the here analyzed period the mountain waves break in the lower stratosphere. Later, the mountain waves can propagate to higher altitudes and exhibit horizontal propagation towards the southeast. It is estimated, that the gravity wave momentum flux of the horizontally propagating mountain waves at 70 km altitude is an order of magnitude larger than the climatological mean. This shows, that the gravity wave momentum flux of mountain waves originating at New Zealand can be transported over several degrees latitude.

Publications

Parts of the results presented in this thesis have been published in the following two articles:

- Ehard, B., B. Kaifler, N. Kaifler, and M. Rapp (2015), Evaluation of methods for gravity wave extraction from middle-atmospheric lidar temperature measurements, *Atmos. Meas. Tech*, doi:10.5194/amt-8-4645-2015.

  B. Ehard conducted the lidar measurements, implemented and tested the different filtering methods, analyzed the results and wrote the paper. B. Kaifler supplied the lidar temperature profiles. B. Kaifler and N. Kaifler build the lidar and conducted part of the lidar measurements. B. Kaifler, N. Kaifler and M. Rapp supervised the study.

- Ehard, B., B. Kaifler, A. Dörnbrack, P. Preusse, S. Eckermann, M. Bramberger, S. Gisinger, N. Kaifler, B. Liley, J. Wagner and M. Rapp (2017), Horizontal propagation of large amplitude mountain waves in the vicinity of the polar night jet, *J. Geophys. Res., 121*, doi:10.1002/2016JD025621.

  B. Ehard conducted the lidar measurements, analyzed the lidar, the ECMWF and the raytracing data, interpreted the results and wrote the paper. B. Kaifler supplied the lidar temperature profiles. P. Preusse helped to set up the raytracing simulations. S. Eckermann provided the AIRS data, which were visualized by M. Bramberger. A. Dörnbrack, B. Kaifler and S. Gisinger contributed in writing the paper. A. Dörnbrack, B. Kaifler and M. Rapp supervised the study.

Contents

1 Introduction

The Earth's atmosphere is divided into four layers: the troposphere, which comprises the lowermost 10 km, the stratosphere, which roughly ranges from 10 km to 50 km altitude, the mesosphere (50 km to 90 km) and the thermosphere, which is located above 90 km altitude. The middle atmosphere comprises the stratosphere and the mesosphere and ranges from about 10 to 90 km altitude. The dynamics of the middle atmosphere are largely influenced by atmospheric wave motions (e.g. *Becker*, 2011). The horizontal scales of these waves range from the planetary scale down to a few kilometers. Planetary scale waves are referred to as planetary waves, or Rossby waves. They are driven by the conservation of potential vorticity. Smaller scale waves with horizontal wavelengths of 1000 km to 1 km are called gravity waves, because the restoring force of these waves is buoyancy and hence gravity. Both types of waves are responsible for several phenomena in the middle atmosphere, such as the Brewer-Dobson circulation (e.g. *Cohen et al.*, 2014), the quasi-biennial oscillation (e.g. *Baldwin et al.*, 2001) or the formation of the cold polar summer mesopause (e.g. *Fritts and Alexander*, 2003). In the mesosphere, gravity waves have a larger influence on the dynamics than planetary waves. This is due to the reason that planetary waves are generally not able to propagate through the stratosphere (*Charney and Drazin*, 1961), whereas gravity waves are able to propagate to mesospheric altitudes.

Sources of atmospheric gravity waves are mainly located within the troposphere. They comprise flow over topography, convection, atmospheric jet-front systems and spontaneous imbalance (e.g. *Fritts and Alexander*, 2003; *Plougonven and Zhang*, 2014, and references therein). Gravity waves do not only transport energy but also momentum. This momentum is transferred to the background atmosphere at the altitude of dissipation, or during phases of transience (*Bölöni et al.*, 2016). As a consequence, a so called gravity wave drag is exerted on the background atmosphere which in turn accelerates the mean flow and changes the dynamical and thermal structure of the background atmosphere. As gravity waves propagate upward within the atmosphere, their amplitude increases exponentially due to the decreasing density, in the absence of wave dissipation. As a result gravity waves become more likely to overturn, break and exert gravity wave drag on the background atmosphere the higher up they propagate. Hence, gravity waves constitute an important coupling mechanism between the troposphere, where most gravity waves are exited, and the middle atmosphere (*Holton and Alexander*, 2000).

If global models are to generate a realistic representation of the middle atmosphere, they have to include a representation of the gravity wave drag. A realistic middle atmosphere in global modeling is of interest, because not only exists a coupling of the troposphere to the middle atmosphere, but also because the middle atmosphere can influence tropospheric weather regimes (e.g. *Baldwin and Dunkerton*, 2001; *Gerber et al.*, 2012; *Kidston et al.*, 2015). The representation of gravity waves is a challenge for global atmospheric models, because the horizontal scale of gravity waves ranges from about 1000 km to 1 km. While the larger scale gravity waves can be resolved by most global models, the smaller scale gravity waves cannot be resolved explicitly because such a fine horizontal resolution requires too large computational resources. Especially global climate models with their coarser resolution (several hundred kilometers) compared to weather prediction models (a few kilometers) struggle in resolving the gravity wave spectrum. As a consequence, the effects of gravity waves on the middle atmospheric circulation have to be parametrized (*Alexander et al.*, 2010).

Due to the limited available computational power, several simplifications are made by these parametrizations. One simplification is the approximation that the gravity waves propagate purely vertically in a single column. This is partly motivated by satellite observations which show the formation of so called gravity wave "hotspots" in the stratosphere, that is to say, regions with enhanced gravity wave activity. These regions are located directly above mountainous regions, such as the southern Andes, the Scandinavian mountain ridge, or the South Island of New Zealand, or above major convective regions such as the tropics or the North American Great Plains during summer (e.g. *Wu and Eckermann*, 2008; *Gong et al.*, 2012; *Hoffmann et al.*, 2013). Another simplification of gravity wave parametrization schemes is that the waves propagate instantaneously from their source region to the altitude of dissipation. Additionally, the gravity wave spectrum at the source altitude is largely unknown. For an in-depth discussion of different parametrization schemes, the reader is referred to the study by *McLandress* (1998).

One important shortcoming of current global models within the middle atmosphere is the problem of the missing gravity wave drag at 60° S (*McLandress et al.*, 2012). This missing gravity wave drag causes the polar night jet to exhibit too large horizontal wind speeds in the southern hemisphere. Additionally there is not enough downwelling in the southern hemispheric wintertime middle atmosphere, which in turn results in a too cold Antarctic stratosphere during wintertime. This problem is well known as the "cold pole bias" (e.g. *Hamilton et al.*, 1999).

During recent years, several studies have investigated the cause of this missing gravity wave drag at 60° S. For example *Alexander and Grimsdell* (2013) and *Hoffmann et al.* (2016) showed that several small islands located in the vicinity of 60° S can be responsible for a significant amount of gravity wave drag within the middle atmosphere. Because these islands are generally underrepresented in gravity wave parametrizations, a proper

treatment of those could improve the representation of the middle atmosphere in global models. Another possible contribution to the missing drag is an underrepresentation of non-orographic sources, such as storm tracks (e.g. *Hendricks et al.*, 2014; *Hindley et al.*, 2015).

McLandress et al. (2012) furthermore speculated that the horizontal propagation of orographic gravity waves, so called mountain waves, could also contribute to the missing drag at 60° S. Such a horizontal propagation cannot be simulated by current gravity wave parametrization schemes due to the single column approximation. On the other hand *Dunkerton* (1984), *Sato et al.* (2009), *Sato et al.* (2012) and *Jiang et al.* (2013) examined simulations, which showed that mountain waves can propagate horizontally over large distances.

Following these studies, this thesis evaluates the following hypothesis:

Mountain waves originating at New Zealand can propagate horizontally away from their source region into the polar night jet.
This horizontal propagation results in a cross-meridional transport of gravity wave momentum flux.

Differing from the above mentioned studies, the occurrence of horizontal propagation is not investigated with the help of simulations alone, but by also analyzing ground-based Rayleigh lidar measurements conducted at Lauder, New Zealand (45.0° S, 169.7° E), during the DEEPWAVE campaign (Deep Propagating Wave Experiment, *Fritts et al.*, 2016). Rayleigh lidar measurements provide temperature profiles with a high vertical and temporal resolution throughout the middle stratosphere up to the mesopause region. Consequently, Rayleigh lidar measurements have been used to study middle atmospheric gravity waves for the last three decades (e.g. *Chanin and Hauchecorne*, 1981; *Gardner et al.*, 1989; *Wilson et al.*, 1991; *Whiteway and Carswell*, 1995; *Duck et al.*, 2001; *Rauthe et al.*, 2008; *Yamashita et al.*, 2009; *Alexander et al.*, 2011; *Kaifler et al.*, 2015a).

Gravity wave signatures are extracted from lidar measurements by subtracting background profiles from the individual measurement profiles. However, all of the previously named studies have used different methodologies to extract gravity waves from their lidar measurements, without comparing their methodology to previous studies. Thus, before the lidar measurements are evaluated, the first question investigated in this thesis is

1) **Which method is most suitable to extract signatures of gravity waves from Rayleigh lidar temperature measurements?**

This question is examined by evaluating four commonly used methods of extracting gravity wave signatures from Rayleigh lidar temperatures. At first synthetic data is used to determine the spectral response of each of the four methods. Afterwards, the four methods are applied to observational data and the results are compared to each other.

Another problem which arises in the interpretation of the lidar measurements is connected to the measurement geometry of the ground-based lidar: Since all the measurements are taken in a strictly vertical column ranging from about 30 km to 80 km altitude, the question of horizontal propagation cannot be assessed by solely analyzing the lidar measurements. A possibility to assess the horizontal propagation of mountain waves is to combine lidar and modeling data. For this purpose data from the integrated forecast system (IFS) of the European Centre for Medium-Range Weather Forecasts (ECMWF) is used. The second question which arises in this context is

2) To what extent are middle atmospheric dynamics resolved by the ECMWF IFS?

In order to assess this question, the mean temperature profile and the middle atmospheric gravity waves simulated by the ECMWF IFS are compared to Rayleigh lidar observations above New Zealand. Motivated by an upgrade of the horizontal resolution of the ECMWF IFS, which fell in the time frame of another gravity wave campaign, two sets of ECMWF IFS simulations with different horizontal resolutions are compared to coinciding Rayleigh lidar observations above Sodankylä, Finland. The differences between both sets of ECMWF IFS simulations are further investigated by examining specific testruns conducted with the ECMWF IFS.

The third part of this thesis focuses on a specific case where the ECMWF IFS closely matches the mountain wave signatures observed by the lidar above New Zealand. In particular, the following question is investigated:

3) Do the large amplitude mountain waves exited above New Zealand during 31 July and 1 August 2014 propagate towards the south?

The Rayleigh lidar temperature measurements during those two days are analyzed to characterize the temporal and vertical evolution of the wave event. ECMWF IFS data is used to characterize the ambient conditions in the troposphere and lower stratosphere. Raytracing simulations are conducted in order to examine the propagational pathways of the mountain waves. Finally, the results are compared to satellite measurements and ECMWF IFS data.

This thesis is structured as follows: Chapter 2 gives a brief introduction of the theory of atmospheric gravity waves. Furthermore the raytracing technique and the Rayleigh lidar technology are described. In Chapter 3 the suitability of different methods for

extracting gravity waves from Rayleigh lidar temperature measurements is evaluated. The gravity waves resolved by the ECMWF IFS are compared to lidar measurements above New Zealand in Chapter 4. Chapter 5 focuses on the lidar measurements on 31 July and 1 August 2014 and the question of the propagational pathway of the mountain waves during this event. Finally, a summary is given in Chapter 6.

2 Theory and Methods

2.1 Gravity waves

Atmospheric gravity waves owe their name to the gravitational force which counteracts the buoyancy of an air parcel and thereby enables wave motions of such an air parcel. In the following the theory to describe linear atmospheric gravity waves will be shown, as well as aspects of wave energy propagation and the effect these gravity waves have upon the global mean circulation. Further information on the theory of internal waves can be found for example in *Sutherland* (2010) or *Nappo* (2002).

2.1.1 The gravity wave dispersion relation

The linear theory for atmospheric gravity waves is derived by starting from the basic conservation laws of fluid dynamics: The conservation of momentum, described by the Navier-Stokes equation (Eq. 2.1); conservation of mass, described by the continuity equation (Eq. 2.2); and the conservation of internal energy (Eq. 2.3). Here the equations are derived in Cartesian coordinates $\vec{x} = (x, y, z)$ and the notation of *Fritts and Alexander* (2003) is adapted:

$$\frac{\partial \vec{u}}{\partial t} + \vec{u} \cdot \nabla \vec{u} + f\left(\vec{e_z} \times \vec{u}\right) = -\frac{1}{\rho}\nabla p - g\vec{e_z} + \vec{D} \tag{2.1}$$

$$\frac{\partial \rho}{\partial t} + \nabla \cdot (\rho \vec{u}) = 0 \tag{2.2}$$

$$\frac{d\theta}{dt} = Q \tag{2.3}$$

Here, $\vec{u} = (u, v, w)$ is the three dimensional velocity vector, f is the Coriolis parameter, ρ the atmospheric density, p the pressure, g Earth's gravitational acceleration and θ is the potential temperature. The vector $\vec{e_z} = (0, 0, 1)$ is the unity vector in the vertical, and $\vec{D}$ and Q denote additional forcing terms. The potential temperature θ is the temperature an air parcel has if it is moved down adiabatically from an altitude with pressure $p(z)$ and temperature $T(z)$ to a reference pressure p_0. It is defined as

$$\theta = T(z)\left(\frac{p_0}{p(z)}\right)^{\frac{R}{c_p}}, \tag{2.4}$$

with the gas constant for dry air R and the heat capacity of dry air under constant pressure c_p.

Equations 2.1–2.4 can be used to describe a large variety of fluid motions, as they yield a set of six equations for the six unknown atmospheric variables u, v, w, p, ρ and θ. However, these equations can be simplified if one wants to describe gravity wave motions.

First of all, it can be assumed that the atmosphere is in hydrostatic balance, thus $\partial p/\partial z = -\rho g$. Second, a Reynolds decomposition is carried out, meaning that an atmospheric variably b can be written as $b = b_0 + b'$, where b_0 denotes the mean state and b' denotes the wave perturbation around the mean state. Making the WKB assumption[1], which assumes that the mean flow varies only slowly over one wavelength or period, it is possible to drop all temporal derivatives of the mean flow b_0. Further, it is assumed that the mean vertical wind w_0 is zero – a good approximation in most atmospheric problems – and that p_0, ρ_0 and θ_0 depend solely on altitude.

With these assumptions at hand one can assume plane wave solutions b' for all atmospheric variables of the form

$$b' = \tilde{b}\left(\vec{x}, t\right) \exp\left[i\left(kx + ly + mz - \omega t\right) + \frac{z}{2H_\rho}\right], \tag{2.5}$$

with the amplitude function $\tilde{b}$, wavenumbers k, l, m, the frequency in a fixed reference frame ω, called the extrinsic frequency, and the atmospheric density scale height $H_\rho = RT/g$. Solving the resulting equation system and omitting acoustic wave solutions, one ends up with the gravity wave dispersion relation[2]:

$$\hat{\omega}^2 = \frac{N^2\left(k^2 + l^2\right) + f^2\left(m^2 + \frac{1}{4{H_\rho}^2}\right)}{k^2 + l^2 + m^2 + \frac{1}{4{H_\rho}^2}} \tag{2.6}$$

$$\text{with} \quad N^2 = \frac{g}{T_0}\left(\frac{dT_0}{dz} + \frac{g}{c_p}\right). \tag{2.7}$$

Here $\hat{\omega} = \omega - ku_0 - lv_0$ is the Doppler-shifted frequency in the reference frame moving with the mean flow of the atmosphere, also called the intrinsic frequency[3], and N is the buoyancy frequency, also called the Brunt-Väisälä frequency. The intrinsic frequency of vertically propagating wave solutions is confined to the range $N > \hat{\omega} > |f|$. Using a typical stratospheric value of $N = 0.02\,\mathrm{s}^{-1}$ and a Coriolis parameter for mid-latitudes of $f = 10^{-4}\,\mathrm{s}^{-1}$, the intrinsic period $\hat{\tau} = \frac{2\pi}{\hat{\omega}}$ ranges between 5 min and 17 h.

[1] Named after Wentzel, Kramers and Brillouin.

[2] A more detailed derivation of the dispersion relation can be found in Chapter 2 of *Fritts and Alexander* (2003) and is thus omitted at this point.

[3] As $w_0 = 0$, the term mw_0 is missing in the definition of $\hat{\omega}$.

One interesting phenomenon can be seen from the dispersion relation, the so called "critical level filtering", which occurs when $\hat{\omega}$ goes to zero. Thus, the extrinsic frequency can be written as $\omega = ku_0 + lv_0$, or in the horizontal plane $\omega = k_h u_{0,h}$, with the horizontal wavenumber $k_h = \sqrt{k^2 + l^2}$ and the horizontal wind $u_{0,h} = \sqrt{u_0^2 + v_0^2}$. Thus, the extrinsic horizontal phase velocity $c_{p,h} = \omega / k_h$ is equal to the horizontal velocity at a critical level. Furthermore it can be shown that the vertical wavenumber m goes to infinity in the vicinity of a critical level. At the same time the amplitude of the waves grows, until the wave overturns and breaks. Thus, waves with a horizontal phase speed $c_{p,h}$ are filtered out at the altitude level, where $c_{p,h} = u_0$, while waves with a different phase speed can propagate through this critical level. Hence, the term "critical level filtering".

2.1.2 Transport of energy

Atmospheric gravity waves transport wave energy along their propagational pathway. In the atmosphere, the horizontally averaged rate of change of the wave energy can be expressed as

$$\frac{\partial \langle E \rangle}{\partial t} + \frac{\partial \langle F_E \rangle}{\partial z} = -\varrho_0 \langle {u_h}' w' \rangle \frac{du_{0,h}}{dz} \,, \tag{2.8}$$

with the local mean density ϱ_0, the vertical energy flux $\langle F_E \rangle = c_{g,z} \langle E \rangle$ and the brackets $\langle \rangle$ denoting the horizontal averaging (cf. *Sutherland*, 2010, Eq. 3.92).

It can be seen that in a flow with vertically constant $u_{0,h}$, Equation 2.8 simplifies to the statement that the energy changes only if the vertical energy flux is divergent. However, as the horizontal wind is generally not constant, the right hand term remains in Equation 2.8, which is also called the "energy production term". Thus, one arrives at the conclusion that wave energy is actually not conserved for atmospheric gravity waves.

However, Equation 2.8 can be modified in a way that a general conservation law can be derived. Then, the conserved quantity is the wave action $\langle A \rangle = \langle E \rangle / \hat{\omega}$ (*Bretherton and Garrett*, 1969) and Equation 2.8 becomes

$$\frac{\partial \langle A \rangle}{\partial t} + \frac{\partial \langle F_A \rangle}{\partial z} = 0 \,. \tag{2.9}$$

Thus, it can be said that wave action only changes when the vertical flux of wave action $\langle F_A \rangle$ is divergent, which is the case for example when the waves are dissipated. On the contrary, if the wave energy changes, one cannot say with absolute certainty if the waves are dissipated or not, as a change of wave energy could also simply be associated with a vertical shear of the horizontal wind.

When analyzing measurements, the wave action is seldom used. One of the reasons is that most measurement systems cannot determine ω. In addition, and even more importantly, Equation 2.9 is only valid for one individual wave. In the case of a superposition of gravity waves – which is generally the case in the atmosphere – the wave action would have to be determined for each individual gravity wave. Since the separation of an observed wave field into individual waves proves to be very challenging, the wave action is generally not used when analyzing observations of gravity waves in the middle atmosphere.

A more feasible approach is to examine the average gravity wave potential energy density (e.g. *Wilson et al.*, 1991; *Whiteway et al.*, 1997; *Rauthe et al.*, 2008)

$$E_p = \frac{1}{2}\frac{g^2}{N^2}\overline{\left(\frac{T'}{T_0}\right)^2}, \tag{2.10}$$

where the overline denotes averaging over a certain time or altitude range. Thus, E_p is a statistical quantity which describes the average wave field and not a single wave. This makes it relatively easy to estimate E_p from observational data. In the theoretical case of a single wave propagating purely vertically in an atmosphere with a constant and uniform background wind, E_p per unit mass increases exponentially with altitude due to the decrease in atmospheric density. In this "simple atmosphere" case, altitude ranges where a single gravity wave is dissipated or reflected, can be identified by a deviation from the exponential growth of E_p with altitude. Since this is the standard approach for analyzing lidar data, it is also used in this thesis in order to ensure comparability with other studies.

2.1.3 Transport of momentum

Besides energy, gravity waves also transport momentum. This momentum is extracted from the atmosphere at the wave source and is deposited in the atmosphere where the wave is dissipated or breaks. Similar to Equation 2.9 one can derive an equation which states that the horizontal mean flow is accelerated where the vertical flux of horizontal momentum is divergent. As gravity wave sources are mostly tropospheric sources and wave breaking and dissipation occurs often in the middle atmosphere, gravity waves constitute an important coupling mechanism between the lower atmosphere and the middle atmosphere (e.g. *Holton and Alexander*, 2000; *Becker*, 2011, and references therein).

The first quantitative description of the effect of gravity wave momentum deposition on the middle atmospheric mean flow was given by *Lindzen* (1981) utilizing the concept of critical level filtering: At mid-latitudes, the zonal wind profile (Fig. 2.1a) is mostly westerly, with increasing westerly winds up to around 50 km altitude. Thus, vertically

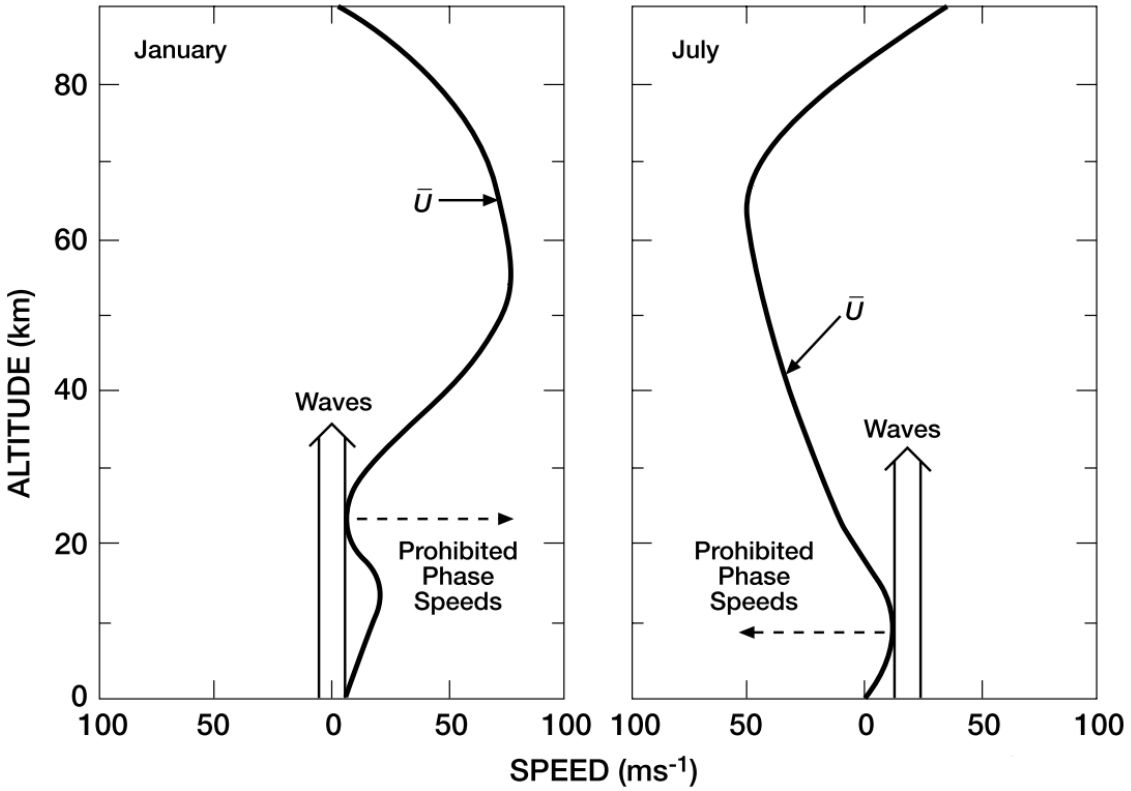

Figure 2.1: Zonal mean wind speed at mid-latitudes in the northern hemisphere during winter (left panel) and summer (right panel) and its effect on vertical wave propagation. Taken from *Brasseur and Solomon* (2005), after *Lindzen* (1981). See text for details.

propagating gravity waves with ground based horizontal phase speeds between the minimum and the maximum zonal wind speed experience a critical level, resulting in the gravity waves being filtered out by the wind within the stratosphere. Gravity waves with easterly phase speeds on the other hand, can reach the middle atmosphere, where they will become unstable and break. As breaking gravity waves act to accelerate the mean flow towards their horizontal phase speed (*Lindzen*, 1981), these breaking waves cause a westward forcing of the mean flow. Thereby they act to weaken the eastward mesospheric jet and cause a reversal of the mesospheric winds during wintertime. In the summer hemisphere, the zonal wind is easterly (Fig. 2.1b). Hence, gravity waves with westerly phase speeds can reach the mesosphere and exert an eastward forcing on the middle atmospheric mean flow.

In the atmosphere, such a forcing of the mean flow is influenced by the Coriolis force as well. Hence, a westward (eastward) forcing of the mean flow induces an additional poleward (equatorward) forcing component. Thus, the mean flow diverges over the

summerpole and converges over the winterpole. Associated with this divergence and convergence is an upwelling motion over the summerpole, which – due to adiabatic expansion of air – results in low temperatures at the polar summer mesopause, and a downwelling motion over the winterpole, which heats the winter mesopause. Thus, the cold polar summer mesopause is an atmospheric feature which arises due to the momentum transport of atmospheric gravity waves.

2.2 Raytracing

The three dimensional propagation of a wave through a background medium can be described by ray theory. Thereby a single wave is described as one ray which propagates through space and time. In principal the same formalism can be applied to internal waves in the atmosphere or the ocean, as well as for acoustic or electromagnetic waves. In the following the fundamental theory for raytracing is derived, which is then applied to the special case of atmospheric gravity waves. A detailed description of the theory of ray tracing can be found e.g. in *Lighthill* (1978, pp. 317).

2.2.1 Ray theory

Assuming that the investigated system allows for plane wave solutions b' of the form

$$b' = \tilde{b}\left(\vec{x}, t\right) \exp\left[i\varphi\left(\vec{x}, t\right)\right], \tag{2.11}$$

with the amplitude $\tilde{b}$ and the phase function φ, then the wave frequency ω and the wave numbers k_i can be defined as

$$k_i = \frac{\partial \varphi}{\partial x_i}, \quad \text{and} \quad \omega = -\frac{\partial \varphi}{\partial t}, \tag{2.12}$$

with the wavevector $\vec{k} = (k_1, k_2, k_3)$.

Using the symmetry of second derivatives (Schwarz's theorem), one can then eliminate the phase function φ, which yields

$$\frac{\partial k_i}{\partial t} + \frac{\partial \omega}{\partial x_i} = 0. \tag{2.13}$$

Assuming that the waves have a general dispersion relation of the form

$$\omega = W\left(\vec{k}, \vec{x}, t\right) \tag{2.14}$$

and inserting it into Equation 2.13, it is found that

$$\frac{\partial k_i}{\partial t} + \sum_{j=1,2,3} \frac{\partial W}{\partial k_j} \frac{\partial k_j}{\partial x_i} = -\frac{\partial W}{\partial x_i} \,. \tag{2.15}$$

From equation 2.12 it can also be shown that $\partial k_j / \partial x_i = \partial k_i / \partial x_j$. Thus the previous equation can be written as

$$\frac{\partial k_i}{\partial t} + \sum_{j=1,2,3} \frac{\partial W}{\partial k_j} \frac{\partial k_i}{\partial x_j} = -\frac{\partial W}{\partial x_i} \,. \tag{2.16}$$

The left-hand side of Equation 2.16 can be written as a Lagrangian derivative of k_i:

$$\frac{dk_i}{dt} = \frac{\partial k_i}{\partial t} + \sum_{j=1,2,3} c_{g,j} \frac{\partial k_j}{\partial x_i} \,, \text{ where} \tag{2.17}$$

$$c_{g,j}\left(\vec{k}, \vec{x}, t\right) = \frac{\partial W\left(\vec{k}, \vec{x}, t\right)}{\partial k_j} \,. \tag{2.18}$$

Here, $\vec{c_g}$ denotes the group velocity vector of the wave, which determines the speed and the direction into which the wave energy propagates.

Thus, in total one ends up with the following equations describing the evolution of a wave as it propagates: Three transport equations describing the ray path

$$\frac{dx_i}{dt} = c_{g,i} = \frac{\partial W}{\partial k_i} \tag{2.19}$$

and three equations describing the modification of the wave number along the ray path, the so called refraction equations

$$\frac{dk_i}{dt} = -\frac{\partial W}{\partial x_i} \,, \tag{2.20}$$

with $i = 1, 2, 3$.

However, this equation system misses an equation describing the evolution of ω along the ray. This equation can be derived in a similar manner as Equation 2.20, resulting in the fourth refraction equation

$$\frac{d\omega}{dt} = \frac{\partial \omega}{\partial t} + \sum_{j=1,2,3} c_{g,j} \frac{\partial \omega}{\partial x_j} = \frac{\partial W}{\partial t} \,. \tag{2.21}$$

2.2.2 Raytracing of atmospheric gravity waves

So far, Equations 2.19–2.21 are valid for all kinds of linear waves. One just has to know the specific dispersion relation of the waves in order to derive the associated raytracing equations. Inserting the dispersion relation of atmospheric gravity waves (Eq. 2.6) and taking into account that $\omega = \hat{\omega} + ku + lv$, one ends up with the following set of equations:

$$\frac{dx}{dt} = u + \frac{k\left(N^2 - \hat{\omega}^2\right)}{\hat{\omega}\Lambda^2} \tag{2.22}$$

$$\frac{dy}{dt} = v + \frac{l\left(N^2 - \hat{\omega}^2\right)}{\hat{\omega}\Lambda^2} \tag{2.23}$$

$$\frac{dz}{dt} = -\frac{m\left(N^2 - \hat{\omega}^2\right)}{\hat{\omega}\Lambda^2} \tag{2.24}$$

$$\frac{dk}{dt} = -k\frac{\partial u}{\partial x} - l\frac{\partial v}{\partial x} - \frac{1}{2\hat{\omega}\Lambda^2}\left[\frac{\partial\left(N^2\right)}{\partial x}\left(k^2 + l^2\right) - \frac{\partial\left(\alpha^2\right)}{\partial x}\left(\hat{\omega}^2 - f^2\right)\right] \tag{2.25}$$

$$\begin{aligned}\frac{dl}{dt} = &-k\frac{\partial u}{\partial y} - l\frac{\partial v}{\partial y} - \frac{1}{2\hat{\omega}\Lambda^2}\left[\frac{\partial\left(N^2\right)}{\partial y}\left(k^2 + l^2\right) - \frac{\partial\left(\alpha^2\right)}{\partial y}\left(\hat{\omega}^2 - f^2\right)\right] \\ &- \frac{\partial f}{\partial y}\frac{f\left(m^2 + \alpha^2\right)}{\hat{\omega}\Lambda^2}\end{aligned} \tag{2.26}$$

$$\frac{dm}{dt} = -k\frac{\partial u}{\partial z} - l\frac{\partial v}{\partial z} - \frac{1}{2\hat{\omega}\Lambda^2}\left[\frac{\partial\left(N^2\right)}{\partial z}\left(k^2 + l^2\right) - \frac{\partial\left(\alpha^2\right)}{\partial z}\left(\hat{\omega}^2 - f^2\right)\right] \tag{2.27}$$

$$\frac{d\omega}{dt} = k\frac{\partial u}{\partial t} + l\frac{\partial v}{\partial t} + \frac{1}{2\hat{\omega}\Lambda^2}\left[\frac{\partial\left(N^2\right)}{\partial t}\left(k^2 + l^2\right) - \frac{\partial\left(\alpha^2\right)}{\partial t}\left(\hat{\omega}^2 - f^2\right)\right], \tag{2.28}$$

with $\Lambda^2 = k^2 + l^2 + m^2 + \alpha^2$ and $\alpha = \frac{1}{2H_\rho}$.

These equations are implemented in the Gravity wave Regional or Global Ray Tracer (GROGRAT) (*Marks and Eckermann*, 1995; *Eckermann and Marks*, 1996), which is used in the following. Note, that Equations 2.22–2.28 do not account for the spherical geometry of the earth, as described by *Hasha et al.* (2008). Therefore, a version of GROGRAT is used in this thesis, into which the changes suggested by *Hasha et al.* (2008) have been implemented.

Equations 2.22–2.28 specify an initial value problem: If the background fields u, v, α and N^2 are known, one can specify an initial wave with k_0, l_0, m_0 and ω_0 at a specific time and location and calculate where this wave propagates. However, as ω_0 is related to k_0, l_0 and m_0 via the dispersion relation, only three parameters are needed, and the fourth one can be calculated from Equation 2.6 using $\omega = \hat{\omega} + ku + lv$.

After an initial set of wave parameters is specified within an atmospheric background, one can integrate Equations 2.22–2.24 over one timestep in order to determine a new

location $\vec{x}$ of the ray. Thereafter, a new wavevector $\vec{k}$ and frequency ω can be determined by integrating Equations 2.25–2.28. Finally, Equations 2.22–2.24 are integrated over another timestep with the new $\vec{k}$ and ω and the procedure starts over.

So far, the rays would propagate for an infinite amount of time. This is unphysical, since in the real atmosphere wave dissipation and also a breakdown of the WKB assumption[4] can occur.

If the WKB assumption breaks down, the so far derived ray theory is no longer valid and thus the calculated rays become unphysical. The breakdown of the WKB assumption can easily be incorporated into the raytracer by calculating the WKB parameter (Eq.5 in *Marks and Eckermann*, 1995)

$$\delta = \frac{1}{m^2}\left|\frac{\partial m}{\partial z}\right| \approx \left|\frac{1}{c_{g,z}m^2}\frac{dm}{dt}\right|, \tag{2.29}$$

where $c_{g,z}$ denotes the vertical group velocity. If $\delta \geq 1$ the WKB approximation is violated and the integration of the specified ray is terminated.

Wave dissipation is implemented in the ray tracer via treating the wave amplitude as an additional variable which is transported with the group velocity along the rays. Since the wave action A has to be conserved, it is straightforward to use Equation 2.9 for the propagation of the wave amplitude. Without modifying Equation 2.9, wave amplitudes would grow infinitely large. In reality, waves overturn and break if their amplitude becomes too large. If this process happens gradually, it is called wave saturation (e.g. *Warner and McIntyre*, 1996, and references therein). The saturation mechanism can be described by a damping term which is added to Equation 2.9. Thus, the waves can exhibit dissipation by limiting the growth in wave amplitude (further details on the damping scheme can be found in Section 3 of *Marks and Eckermann*, 1995). As a final step, if the wave amplitude falls below a certain threshold, it is assumed that the wave has dissipated completely. In this case, the ray integration is terminated.

2.3 Lidar

Lidar (light detection and ranging) is an active remote sensing technology which uses a pulsed light source (generally a laser) to measure the distance to a scattering object. By measuring the time between the pulse emission and the received signal, the distance between the lidar and the scattering object can be determined. By measuring the signal strength and the optical properties of the backscattered light (e.g. wavelength, polarization) further information about the scattering object can be derived. Additionally, many lidar systems offer the possibility of a high spatial and

[4]The mean flow varies only slowly over one wavelength or period, cf. Sec. 2.1.1

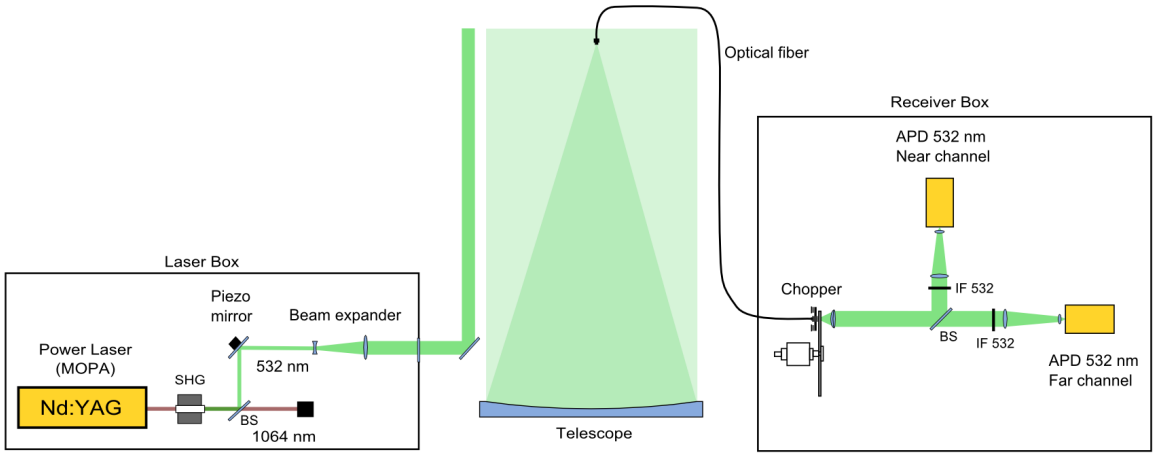

Figure 2.2: Optical setup of the CORAL lidar. MOPA – master oscillator power amplifier, SHG – second harmonic generator, BS – beam splitter, IF – interference filter, APD – avalanche photo diode. Courtesy of B. Kaifler.

temporal resolution. As a consequence, a large variety of lidar systems are applied within atmospheric science. For example, high spectral resolution lidars for aerosol studies, Doppler lidars for measuring atmospheric wind profiles, Raman lidars and differential absorption lidars for trace gas measurements and resonance lidars for measuring processes within atmospheric metal layers. A general overview over lidar technology and different kinds of lidar systems can be found in *Weitkamp* (2005).

2.3.1 The DLR Rayleigh lidar systems

The German Aerospace Center (DLR) currently operates two ground based lidar systems, TELMA and CORAL[5], capable of measuring temperature in the middle atmosphere. As an example, the optical setup of the CORAL lidar is shown in Figure 2.2. Both TELMA and CORAL are equipped with a frequency doubled ND:YAG laser emitting 12 W of optical power with a pulse repetition rate of 100 Hz at a wavelength of 532 nm. A 63 cm diameter telescope with a field of view of 240 µrad collects the backscattered light and focuses it into an optical fiber. The receiver consists of two cascaded avalanche photo diodes which detect the backscattered light in different altitude regions. In order to suppress the atmospheric background, the light passes through interference filters before being focused onto the photo diodes. TELMA has an additional receiving channel for measuring the vibrational Raman transition of nitrogen atoms at a wavelength of 608 nm. The detectors are operated in single-photon counting

[5]The Temperature Lidar for Middle Atmosphere Research (TELMA) and the Compact Rayleigh Autonomous Lidar (CORAL)

mode in which the individual photons are detected with a time resolution of 2 ns. This allows for a wide range of vertical and temporal resolutions when analyzing the data.

2.3.2 Retrieving atmospheric temperature

A Rayleigh lidar such as TELMA and CORAL measures the elastically backscattered light, which is the light scattered towards the emitter without changing its wavelength. Two scattering mechanisms contribute to the elastic backscatter signal: Rayleigh scattering and Mie scattering. Rayleigh scattering occurs when the scattering object is much smaller than the wavelength λ of the scattered light. This is the case for air molecules such as nitrogen or oxygen. The intensity of the backscattered signal in this case is proportional to λ^{-4}. Mie scattering occurs for particles too large for Rayleigh scattering, such as aerosols or cloud droplets. In this case the backscattered light is no longer a simple function of wavelength but depends on the size, shape and composition of the particle as well.

In the absence of aerosols, which is the case in the upper stratosphere and mesosphere, the elastic backscattering signal is purely due to molecular scattering and one can determine the temperature from this signal, as first proposed by *Hauchecorne and Chanin* (1980). Here, one can write the measured signal as a function of altitude (see *Behrendt*, 2005) as

$$S(z) = C\frac{\vartheta(z)\,N(z)}{z^2}\,, \tag{2.30}$$

where C is a constant containing all system parameters, ϑ is the atmospheric transmission and N is the number density of scattering molecules. The factor z^2 arises due to the light being scattered into all directions and not only towards the lidar.

With the hydrostatic equation

$$\frac{dp(z)}{dz} = -\rho(z)\,g\,, \tag{2.31}$$

the ideal gas law

$$p(z) = k_B N(z)\,T(z)\,, \tag{2.32}$$

where k_B is the Boltzmann constant, and keeping in mind that $\rho(z) = N(z)\,M$, where M is the mean molecular mass of the atmospheric constituents, one can integrate the hydrostatic equation and solve for the temperature, yielding

$$T(z) = \frac{z_r^2 S(z_r)}{z^2 S(z)} T(z_r) - \frac{M}{k_B}\int_{z_r}^{z} \frac{\zeta^2 S(\zeta)}{z^2 S(z)} g(\zeta)\,d\zeta\,, \tag{2.33}$$

where z_r is a reference altitude.

In the derivation of Equation 2.33, it was assumed here that the atmospheric transmission of the atmosphere is large and independent of altitude. This approximation is valid in the middle atmosphere in the absence of strong absorption lines, which is the case for most wavelengths in the visible spectrum. As a consequence ϑ (cf. Eq. 2.30) cancels out in the derivation of Equation 2.33. In Equation 2.33 the integration usually would be carried out from infinity to the altitude z. However, the measured signal will always be capped at some altitude, since the signal strength decreases exponentially with altitude due to the exponentially decrease in atmospheric density. This top altitude is set to be the reference altitude z_r.

The integration in Equation 2.33 is carried out top-down. This might seem strange, as an initial seeding temperature $T(z_r)$ at higher altitudes often has a larger uncertainty compared to lower altitudes. However, since the first term in Equation 2.33 is proportional to $1/S(z)$ and $S(z)$ increases exponentially with decreasing altitude, the contribution of the initial temperature $T(z_r)$ to the temperature at an altitude $T(z)$ decreases exponentially with decreasing altitude. It can easily be seen from Equation 2.33, that if the integration is carried out from the bottom to the top, a small uncertainty in the seeding temperature increases exponentially with increasing altitude, rendering the retrieved temperatures unreliable.

The seeding temperature $T(z_r)$ for the top-down integration can be estimated by several methods. The most accurate method is using data from a collocated resonance lidar, which measures the temperature directly via the temperature broadening of an atomic resonance line within a metal layer at mesopause altitudes (e.g. *Rauthe et al.*, 2006). Other possibilities include using satellite measurements taken in close proximity to the lidar (e.g. *Alexander et al.*, 2011) or simply a climatological value from a reference atmosphere (e.g. *Hauchecorne and Chanin*, 1980).

In the case of TELMA and CORAL the seeding temperature is acquired from a satellite observation in close proximity to the lidar, preferably from SABER (Sounding of the Atmosphere using Broadband Emission Radiometry *Remsberg et al.*, 2008) or, if SABER is not available, from MLS (Microwave Limb Sounder *Waters et al.*, 2006). The temperature retrieval first calculates an average temperature profile from the nightly mean measurement profile which is seeded at the top (chosen to be where the signal to noise ratio is equal to 5) with the satellite temperature. It should be kept in mind, that the contribution of the seeding temperature $T(z_r)$ to the measurement uncertainty decreases exponentially with decreasing altitude (cf.. Eq. 2.33). After the initial integration, the time resolution of the retrieved temperature profiles is gradually enhanced, which decreases the reference altitude z_r due to the decreasing SNR. At each new reference altitude z_r the temperature from the previously coarser resolved temperature profile is taken as seeding temperature. By this procedure the contribution of the uncertainty of the seeding temperature is reduced as far as possible, allowing

for the retrieval of temperature profiles with a spatial and temporal resolution of 900 m × 10 min in an altitude range of ≈ 25 km to 85 km. Measurement uncertainties are typically on the order of 2 K to 3 K at 70 km altitude and generally lower than 1 K below 60 km altitude (*Ehard et al.*, 2015). Note, that the lower altitude limit of the temperature profile is due to the presence of aerosols in the lower stratosphere. Hence, the measured Rayleigh signal is no longer a pure function of atmospheric density and the integration method can no longer be applied to derive atmospheric temperature profiles.

An alternative to the integration technique by *Hauchecorne and Chanin* (1980) is an optimal estimation method recently developed by *Sica and Haefele* (2015). This method no longer relies on the seeding by an initial temperature profile. However, as the SNR also decreases at the top of the measurement range, the retrieved temperature profile relies largely on the initially assumed a-priori temperature profile at the top. Thus, the uncertainties at the higher altitudes associated with this method are large as well, and the differences between the integration method and the optimal estimation method are small (cf. Fig. 14, *Sica and Haefele*, 2015). Therefore, the integration technique has been used in this thesis instead of the optimal estimation retrieval.

3 Extracting gravity waves from lidar temperature measurements

The results presented in this chapter have been published by Ehard et al. (2015).

Gravity waves are usually determined from lidar measurements by subtracting an estimated background temperature (density) profile from the measured profiles in order to derive temperature (density) perturbation profiles. Several methods have been developed and used over the last decades. For example *Gardner et al.* (1989), *Rauthe et al.* (2008) and *Ehard et al.* (2014) calculate a nightly mean profile and subtract it from the (time resolved) individual profiles. *Yamashita et al.* (2009) remove a background profile determined by a temporal running mean (in addition to vertical filtering). Perturbation profiles obtained through a fit of polynomial functions to the measured profiles are examined e.g. by *Whiteway and Carswell* (1995), *Duck et al.* (2001) or *Alexander et al.* (2011). *Mzé et al.* (2014) apply a variance method in order to determine perturbation profiles, while *Chane-Ming et al.* (2000) use spectral filtering.

All of these methods are most sensitive to different parts of the gravity wave spectrum. Thus, results from different lidar studies become hardly comparable because one cannot distinguish between variations that are caused by the application of a different methodology to extract gravity wave perturbations and variations that are geophysically induced. *Ehard et al.* (2014) compared values of gravity wave potential energy density E_p from different studies to their results. Due to potential methodological biases it remained unclear whether the differences were in fact of geophysical origin. Hence, they expressed the need for a standardized method to extract gravity wave amplitudes from lidar measurements.

This chapter will evaluate and compare four methods in detail: subtraction of the nightly mean profile, subtraction of temporal running mean profiles, the sliding polynomial fit method proposed by *Duck et al.* (2001) and the application of a Butterworth filter. While the first two methods rely on filtering in time, the latter two methods apply a filter in space to determine wave induced temperature perturbations.

3.1 Methods

Lidar studies usually determine wave induced temperature perturbations $T'(z,t)$ (which are a function of altitude z and time t) from the measured temperature profile $T(z,t)$ by subtracting a background temperature profile $T_0(z,t)$:

$$T'(z,t) = T(z,t) - T_0(z,t)\,. \tag{3.1}$$

$T_0(z,t)$ ideally contains all contribution from radiative and chemical heating and other large scale effects such as planetary waves and tides. Hence, the temperature perturbations $T'(z,t)$ should be solely caused by gravity waves. Estimation of $T_0(z,t)$ is challenging due to the specific shape of the temperature profile with its changes in vertical temperature gradient, e.g. at the stratopause or mesopause.

As described already in Section 2.1.1, the intrinsic period $\hat{\tau}$ of a gravity wave which may be present in $T'(z,t)$ ranges between 5 min and 17 h. It is important to note that the lidar only detects the extrinsic period τ which can be Doppler shifted to larger or smaller values, depending on local wind conditions. Typical vertical wavelengths of gravity waves measured by ground based instruments vary between 1 and 17 km (see *Chane-Ming et al.*, 2000, their Table 2). The spatial scales combined with the temporal scales define the spectral requirements on the methods of extracting gravity wave induced temperature perturbations.

3.1.1 Time-averaged background profiles

A widely applied method is the use of the nightly mean temperature profile as background temperature profile (e.g *Gardner et al.*, 1989; *Rauthe et al.*, 2008; *Ehard et al.*, 2014). Thereby it is assumed that the timescales of phenomena other than gravity waves affecting the temperature profile are considerably larger and the timescales of gravity waves are smaller than the measurement period, which is typically in the range of 3 h to 12 h.

Another common method is to determine background temperature profiles by means of a running mean over a time window which is typically on the order of 3 h (e.g. *Yamashita et al.*, 2009). Temperature variations with timescales larger than the window width are attributed to the background temperature profiles and are therefore not included in the extracted gravity wave spectrum.

3.1.2 Sliding polynomial fit

Duck et al. (2001) proposed a method of extracting temperature perturbations based on a sliding polynomial fit in the spatial domain. The method is sensitive to small

vertical scales and ignores the temporal evolution of waves. The method is based on the assumption that temperature variations with large vertical scales can be attributed either to the climatological thermal structure of the atmosphere (i.e. the different vertical temperature gradients in the troposphere, stratosphere and mesosphere), the advection of colder or warmer air masses, or tides and planetary waves. Only variations with a spatial scale smaller than a certain threshold are identified as gravity waves.

The sliding polynomial fit method was designed to produce a background temperature profile which contains all perturbations with vertical scales larger than 15 km. For each measured temperature profile *Duck et al.* (2001) applied a series of overlapping cubic polynomial fits to each range gate. Each fit was applied to an altitude window with a width of $L_\mathrm{f} = 25\,\mathrm{km}$. A weighted average was computed to reconstruct the background temperature profile from the individual polynomial fits using the weighting function

$$w(z)_i = \begin{cases} \exp\left(\frac{z-(z_{\mathrm{c},i}-\delta)}{\gamma}\right) & \text{if } z \leq z_{\mathrm{c},i} - \delta \\ 1 & \text{if } z_{\mathrm{c},i} - \delta < z < z_{\mathrm{c},i} + \delta \\ \exp\left(-\frac{z-(z_{\mathrm{c},i}+\delta)}{\gamma}\right) & \text{if } z \geq z_{\mathrm{c},i} + \delta\,. \end{cases} \tag{3.2}$$

Here $\delta = 0.5L_\mathrm{f} - L_\mathrm{w}$, L_w is the width of the weighting window, $z_{\mathrm{c},i}$ the center altitude of the individual fit and γ the e-folding width which defines how fast the weighting function decreases. *Duck et al.* (2001) used a weighting window length $L_\mathrm{w} = \frac{L_\mathrm{f}}{3}$ and $\gamma = 3\,\mathrm{km}$. *Duck et al.* (2001) smoothed the resulting background temperature profiles with a 1.5 km boxcar mean. These profiles were then subtracted from the corresponding measured temperature profiles according to Eq. (3.1), yielding the temperature perturbation profiles.

Here the following set of parameters is used: a fit length $L_\mathrm{f} = 20\,\mathrm{km}$, a weighting window length $L_\mathrm{w} = 3\,\mathrm{km}$ and an e-folding width $\gamma = 9\,\mathrm{km}$. These parameters are chosen because they yield the flattest spectral response for the altitude resolution used in this thesis (see Sect. 3.4 for further details). The boxcar smoothing showed to have a negligible effect. Hence, it is not applied.

3.1.3 Spectral filter

Another method which can be applied to vertical profiles is spectral filtering (e.g. *Chane-Ming et al.*, 2000). By applying a high-pass filter to individual temperature profiles, temperature perturbations can be retrieved. In order to yield perturbations caused by gravity waves, a filtering function has to be chosen which has an adequate spectral response.

In this thesis a 5th order Butterworth high-pass filter with a cutoff wavelength $\lambda_c = 15\,\mathrm{km}$ is used. The transfer function is defined as

$$H(\lambda_z) = \left(1 + \left(\frac{\lambda_z}{\lambda_c}\right)^{2n}\right)^{-\frac{1}{2}}, \tag{3.3}$$

where n is the order of the filter and λ_z is the vertical wavelength. The Butterworth filter is chosen due to its flat frequency response in the passband. The filter itself is applied in Fourier space. As the Fourier transformation assumes a cyclic dataset, the upper and lower end of the measured temperature profile are internally connected. This creates an artificial discontinuity which introduces a broad range of frequencies including frequency components that are in the passband of the filter. These frequency components contribute to temperature perturbations at the upper and lower end of the analyzed altitude window and thus artificially enhance gravity wave signatures. In order to mitigate this effect, the dataset is mirrored at the lowest altitude bin and attached to the original dataset before the filtering process. Thereby, the dataset can be cyclic extended without discontinuities at the lower end, where temperature perturbations are smallest and therefore artificial enhancements produce largest relative errors. After the filtering, only the original half of the resulting perturbation profile is retained.

3.2 Application to synthetic data

In order to characterize the different methods regarding their ability to extract gravity wave induced temperature perturbations from middle atmospheric temperature profiles, the methods are applied to a synthetic dataset with known temperature perturbations. These perturbations are added to a fixed, realistic background temperature profile $T_0(z)$. The latter is derived from the mean temperature profile above Lauder, New Zealand (45.0° S, 169.7° E), measured with TELMA from July until end of September (black line in Fig. 3.1a). The particular choice of the background temperature profile does not affect the results as long as the background temperature profile is realistic, smooth and does not contain contributions from gravity waves. For example, with a climatological or a model temperature profile, similar results can be obtained.

Sinusoidal temperature perturbations with exponentially increasing amplitude were added to the background temperature profile according to

$$T_s(z,t) = T_0(z) + T_s'(z,t), \quad \text{with} \tag{3.4}$$

$$T_s'(z,t) = \tilde{T}\cos\left(\frac{2\pi z}{\lambda_z} + \frac{2\pi t}{\tau}\right)\exp\left(\frac{z - z_0}{2H}\right), \tag{3.5}$$

with the amplitude $\tilde{T}$, the vertical wavelength λ_z, the observed period τ the scale height H and the lowest altitude of the analyzed altitude range z_0. An example

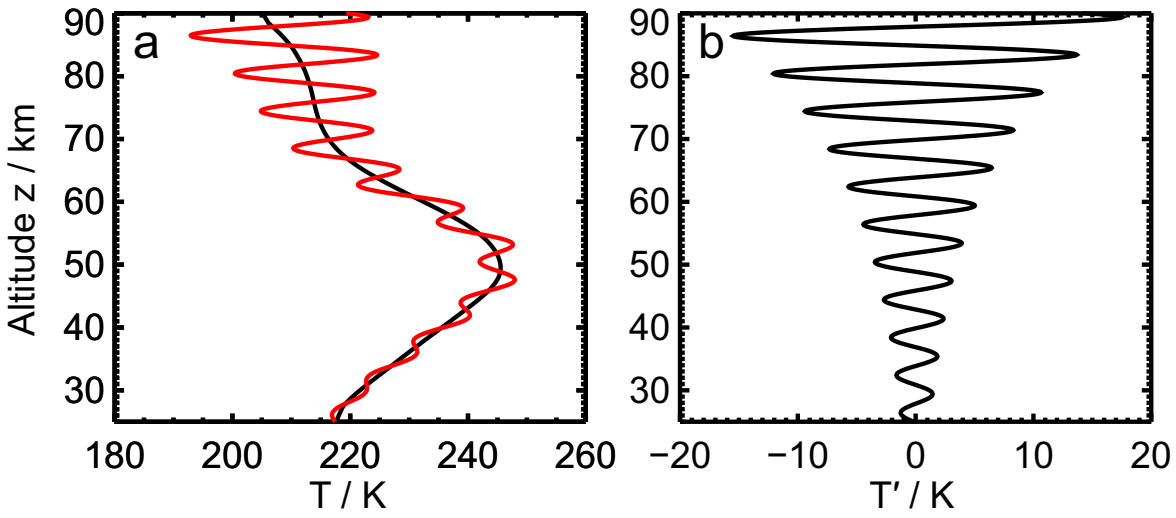

Figure 3.1: (a) Background temperature profile T_0 used for the simulations (black) and perturbed temperature profile T (red). (b) The temperature perturbations T' added to T_0. Temperature perturbations in both panels were constructed using Equation 3.5 with the following set of parameters: $t = 4\,\mathrm{h}$, $\tilde{T} = 1.2\,\mathrm{K}$, $\lambda_z = 6\,\mathrm{km}$, $\tau = 1.9\,\mathrm{h}$, $H = 12\,\mathrm{km}$.

of the perturbed background profile T_s can be seen in Fig. 3.1a (red line) and the corresponding temperature perturbations T'_s in Fig. 3.1b.

For each method, the spectral response $R_m(z)$ was calculated from the ratio between the time averaged absolute values of the determined temperature perturbations $\overline{|T'_m(z,t)|}$ and the synthetic temperature perturbations $\overline{|T'_\mathrm{s}(z,t)|}$ as

$$R_m(z) = \frac{\overline{|T'_m(z,t)|}}{\overline{|T'_\mathrm{s}(z,t)|}} \cdot 100\,\% \,. \tag{3.6}$$

A spectral response larger than 100 % indicates an overestimation of gravity wave amplitude, while a value below 100 % indicates an underestimation of gravity wave amplitude.

All simulations conducted for this thesis use the realistic set of parameters $\tilde{T} = 1.2\,\mathrm{K}$, $H = 12\,\mathrm{km}$ and $z_0 = 25\,\mathrm{km}$. A height resolution of $\Delta z = 0.1\,\mathrm{km}$ was used, while the altitude interval ranged from 25 km to 90 km. A time interval of 8 h, corresponding to the length of an average nighttime measurement period, with a resolution of $\Delta t = 0.5\,\mathrm{h}$ was used. For each simulation either λ_z or τ was kept constant, while the other was varied. The vertical wavelength λ_z was varied from 0.6 km to 20 km in steps of 0.2 km, while the gravity wave period τ was varied from 0.15 h to 14.95 h in steps of 0.1 h.

3.2.1 Constant background temperature

As a first step, simulations were carried out with a constant background temperature profile $T_0(z)$. In order to reduce aliasing effects caused by even multiples of the analyzed time window (8 h), the period of simulated gravity waves was set to $\tau = 1.9$ h while the vertical wavelength λ_z was varied. Figure 3.2 depicts the spectral response of the different methods as a function of vertical wavelength.

The nightly mean method (Fig. 3.2a) and the 3 h running mean method (Fig. 3.2b) both exhibit an almost uniform spectral response at all altitudes and wavelengths. However, the running mean slightly overestimates the extracted temperature perturbations. The sliding polynomial fit method (Fig. 3.2c) shows a reduced spectral response for vertical wavelengths larger than ≈ 13 km. For shorter vertical wavelengths the spectral response is close to 100 % at most altitudes. Vertical wavelengths of ≈ 9 km show a slight reduction in spectral response over the entire altitude range. At the upper and lower 5 km of the analyzed altitude window vertical wavelengths larger than 5 km are strongly damped. The spectral response of the Butterworth filter (Fig. 3.2d) is very similar to the sliding polynomial fit. The main difference is that the Butterworth filter exhibits no underestimation of temperature perturbations at 9 km vertical wavelength.

Figures 3.2e and f show mean extracted temperature perturbations. The blue line (here underneath the green line) depicts the original temperature perturbations added to the background temperature profile. As evident from Fig. 3.2e, the sliding polynomial fit method underestimates temperature perturbations at vertical wavelengths around 9 km. In agreement with the filter design both vertical filtering methods, the sliding polynomial fit and the Butterworth filter, show a decrease in extracted temperature perturbations for vertical wavelengths larger than 13 km. This decrease is almost linear with increasing vertical wavelength. As a consequence, amplitudes are effectively reduced by a factor of 3 at $\lambda_z = 20$ km.

In the first simulation setup the vertical wavelength λ_z was varied, while the period τ was kept constant. Now the period τ is varied while the vertical wavelength is fixed at $\lambda_z = 6$ km (Fig. 3.3). The spectral response of the nightly mean method (Fig. 3.3a) is close to 100 % at all altitudes. Temperature perturbations with periods larger than 10 h are damped and periods around 6 h are slightly underestimated. For $\tau = 15$ h the reduction in amplitude is ≈ 20 % (green line in Fig. 3.3e and f). Like the nightly mean method, the 3 h running mean (Fig. 3.3b) exhibits a uniform spectral response at all altitudes. However, waves with periods longer than 3.5 h are strongly damped. At a period of 6 h temperature perturbations are underestimated by a factor of 2 and for $\tau = 2.5$ h amplitudes are overestimated by ≈ 20 % (orange line in Fig. 3.3e and f). The spectral response of the filter for waves with shorter periods oscillates between over- and underestimation as τ approaches zero. In contrast, the sliding polynomial fit method (Fig. 3.3c) and the Butterworth filter (Fig. 3.3d) both exhibit

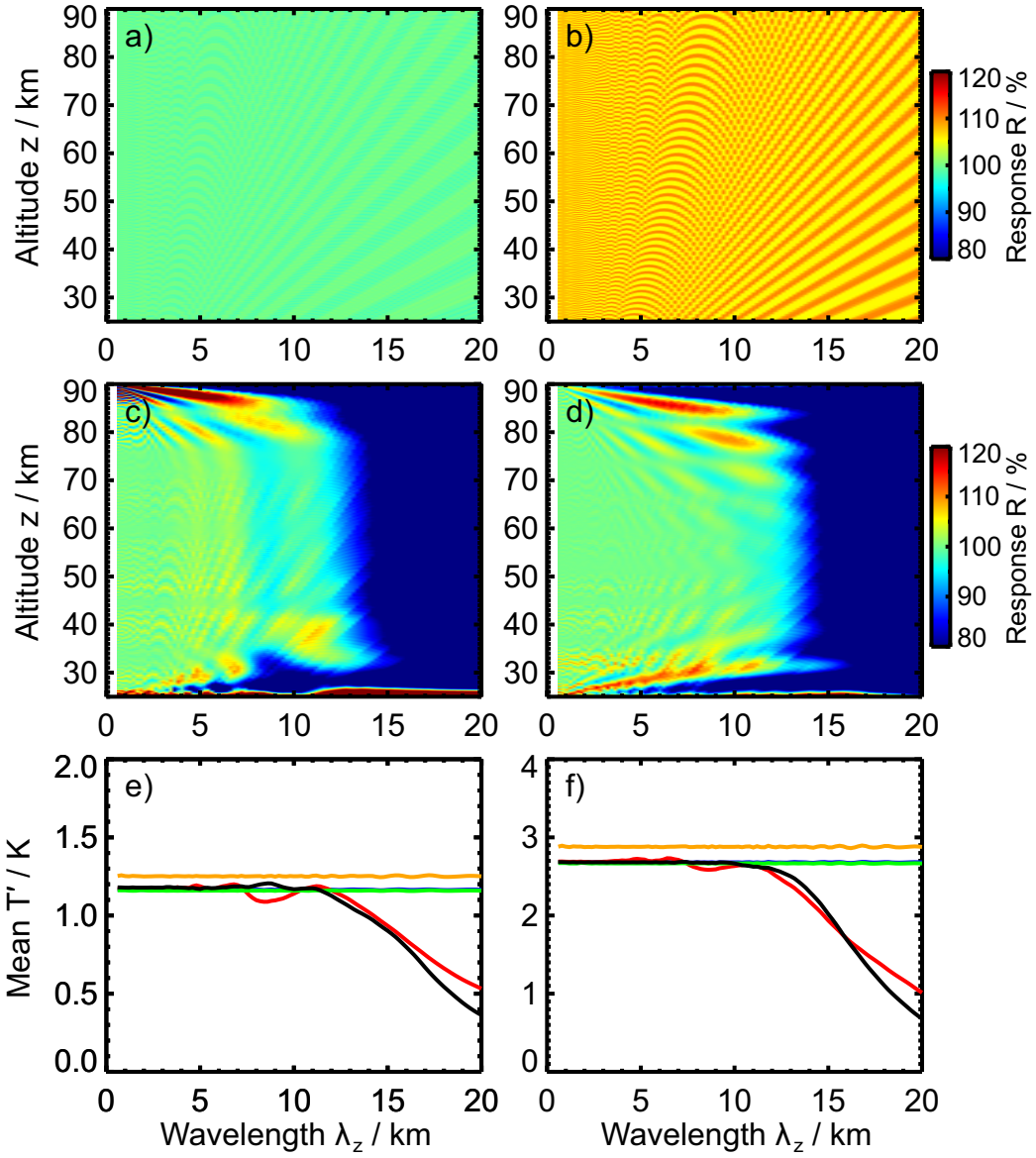

Figure 3.2: Spectral response of different methods of determining temperature perturbations as a function of vertical wavelength λ_z: Nightly mean (a), 3 h running mean (b), sliding polynomial fit (c) and Butterworth filter (d). Panels (e) and (f) depict mean extracted temperature perturbations between 30 km to 40 km (e) and 50 km to 60 km (f) as well as the simulated temperature perturbations (blue line). The different methods are color coded as follows: Nightly mean – green, 3 h running mean – orange, sliding polynomial fit – red, Butterworth filter – black. Please note that the blue line in this case lies exactly underneath the green line. All simulations were carried out with $\tau = 1.9$ h and a background temperature profile constant in time.

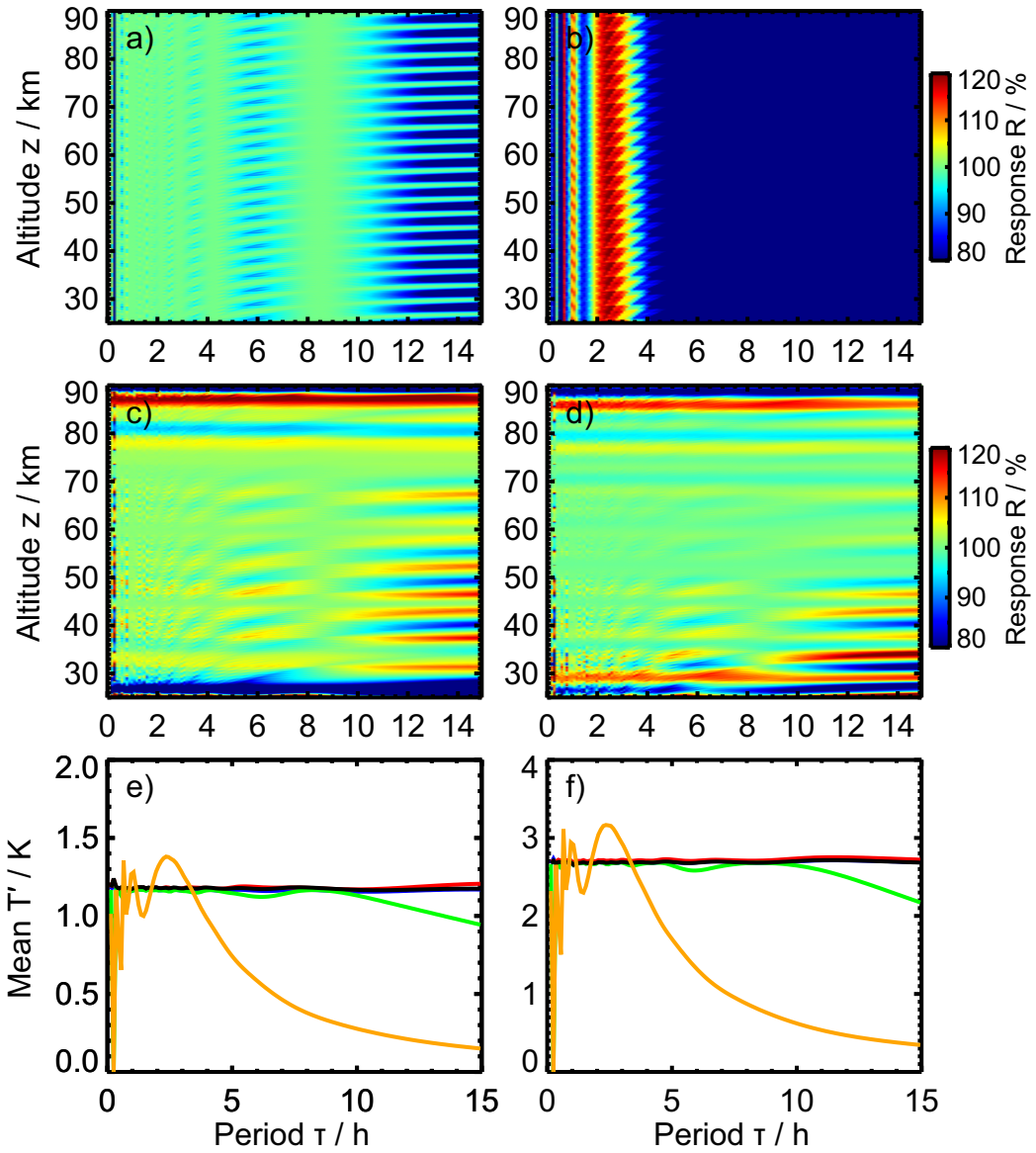

Figure 3.3: Same as Figure 3.2 but as a function of period τ. All simulations were carried out with a fixed vertical wavelength of 6 km and a background temperature profile constant in time. Note that the blue and black lines in panels (e) and (f) are lying on top of each other.

an almost uniform spectral response for most periods. Only for very long periods the spectral response oscillates between over- and underestimation with increasing altitude, indicating a slight phase delay between simulated and extracted temperature perturbations.

3.2.2 Varying background temperature

While in the previous section the simulated background temperature was kept constant, now the influence of a time dependent variation of the background temperature is examined. Slow variations of the form

$$T_0'(z,t) = \alpha\, t\, \sin\left(\frac{2\pi\,(z-z_0)}{60\,\mathrm{km}}\right) \exp\left(\frac{z-z_0}{H_0}\right) \tag{3.7}$$

were added to Eq. (3.4), where $\alpha = 0.5\,\mathrm{K\,h^{-1}}$ is the heating/cooling rate and $H_0 = 65\,\mathrm{km}$ is the scale height of the background temperature variation. This results in a warming of the stratosphere and a cooling of the mesosphere over time, representing a very simplified effect of a propagating planetary wave with a vertical wavelength of 60 km. All other parameters are the same as before.

Filter characteristics are shown for a varying vertical wavelength in Fig. 3.4. Compared to the steady background simulations (e.g. Fig. 3.2), the nightly mean method exhibits an enhanced spectral response around 35 and 65 km altitude (Fig. 3.4a). From Fig. 3.4e it can be determined that the nightly mean method overestimates temperature perturbations by roughly 25 % between 30 and 40 km altitude. No change in spectral response is detected for the 3 h running mean method (Fig. 3.4b), the sliding polynomial fit method (Fig. 3.4c) and the Butterworth filter (Fig. 3.4d).

The filters exhibit similar characteristics if the gravity wave period is varied instead of the vertical wavelength. The nightly mean method (Fig. 3.5a) overestimates temperature perturbations in the same altitude bands as shown for the simulations with varying vertical wavelength (cf. Fig. 3.4a). The filter characteristics of the 3 h running mean method (Fig. 3.5b), the sliding polynomial fit method (Fig. 3.5c) and the Butterworth filter (Fig. 3.5d) are not affected by the varying background temperature.

3.3 Application to measurement data

Rayleigh lidar measurements at Lauder, New Zealand, (45.0° S, 169.7° E) were obtained with the TELMA instrument from mid June to mid November 2014 (*Kaifler et al.*, 2015b). Here, temperature data with a temporal resolution of 10 min and a vertical resolution of 100 m was used. The effective vertical resolution of the temperature data is 900 m due to smoothing of the raw data before processing.

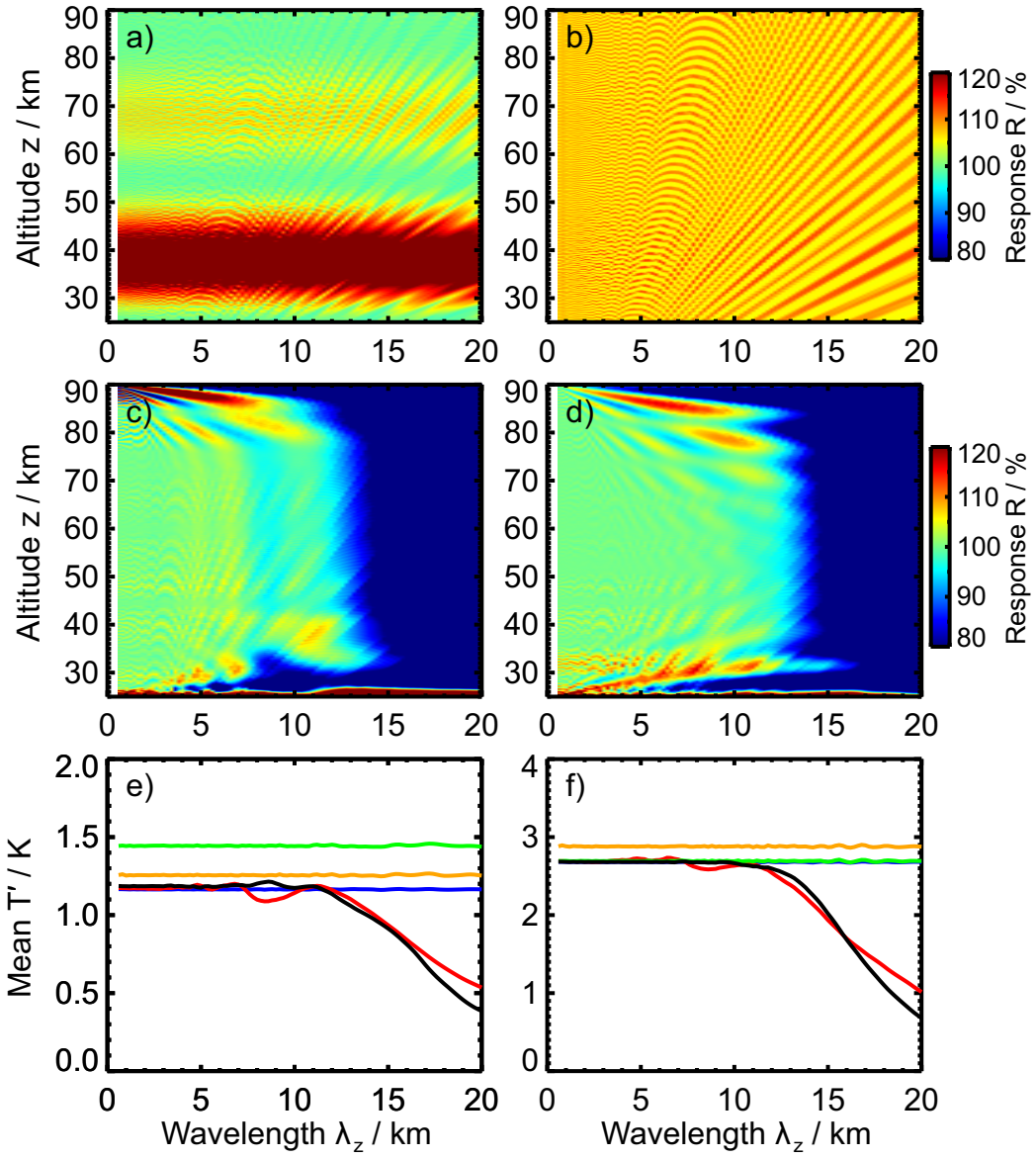

Figure 3.4: Same as Figure 3.2 but with a varying background temperature (see Section 3.2 for details).

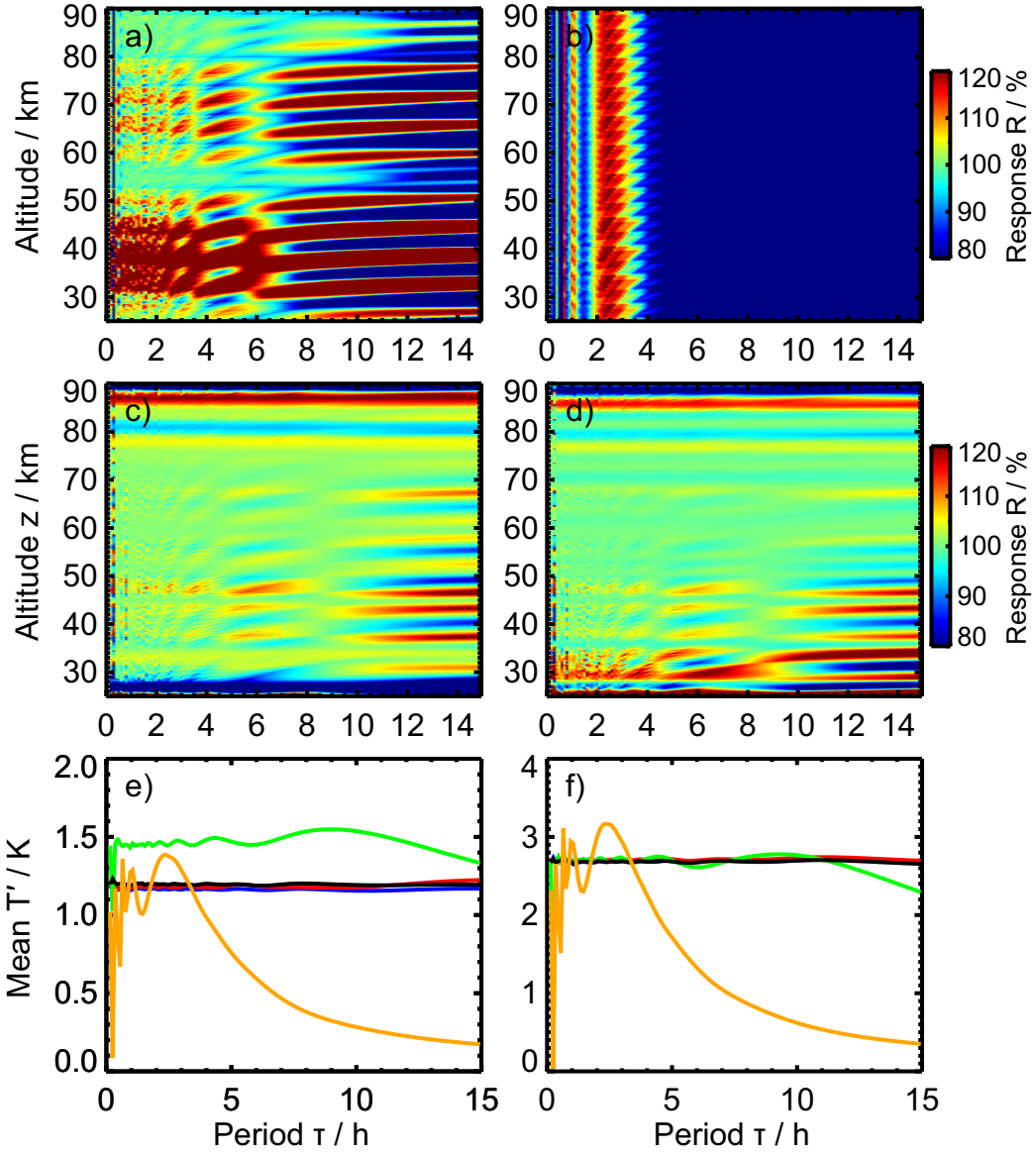

Figure 3.5: Same as Figure 3.3 but with a varying background temperature (see Section 3.2 for details).

3.3.1 Case study: 23 July 2014

A detailed analysis with the four different methods of extracting temperature perturbations is shown for the dataset obtained on 23 July 2014 in Fig. 3.6. This case was chosen because the gravity wave analysis depicts many previously noted characteristics of the four methods.

The main features of the mean temperature profile (Fig. 3.6b) are the stratopause between 45 and 55 km altitude with $T \approx 245$ K and the temperature minimum of approximately 200 K at 73 km altitude below a mesospheric inversion layer. The time evolution of the temperature measurements (Fig. 3.6a) shows an increase of the temperature at the stratopause and a jump in stratopause height around 8.00 UTC. Afterwards, the stratopause descends slowly. The structure of the mesospheric inversion layer varies also over time with the minimum temperature below the inversion layer reaching ≈ 175 K around 14.00 UTC.

The temperature perturbations as determined by the nightly mean method (Fig. 3.6c) exhibit a vertically broad maximum descending from about 80 km altitude down to 50 km altitude over the 12 h measurement period. Temperature perturbations within this descending maximum reach values of up to ± 20 K. Below 50 km altitude temperature perturbations are generally on the order of ± 5 K.

The 3 h running mean method on the other hand (Fig. 3.6d) shows strongly tilted patterns. Below 50 km altitude the phase lines tend to be steeper than above. The magnitude of the temperature perturbations generally increases with altitude from approximately ± 5 K below 60 km altitude to approximately ± 15 K above 60 km altitude.

The sliding polynomial fit method (Fig. 3.6e) and the Butterworth filter (Fig. 3.6f) extract almost identical patterns of temperature perturbations, with the Butterworth filter inferring slightly larger amplitudes. The phase lines in the Fig. 3.6e and f decrease more slowly in altitude compared to the 3 h running mean method. Below 60 km altitude temperature perturbations are below ± 10 K for both filters and increase to ± 15 K above 60 km altitude.

3.3.2 Statistical performance

From TELMA observations above New Zealand during the period 1 July 2014 to 30 September 2014 the mean E_p per mass (Eq. 2.10) was determined using the four methods of gravity wave extraction discussed previously (Fig. 3.7). The absolute value of E_p varies by as much as one order of magnitude depending on which method is used. The largest relative deviations appear in the lower stratosphere between the 3 h running mean method and the Butterworth filter. Above 65 km altitude all methods

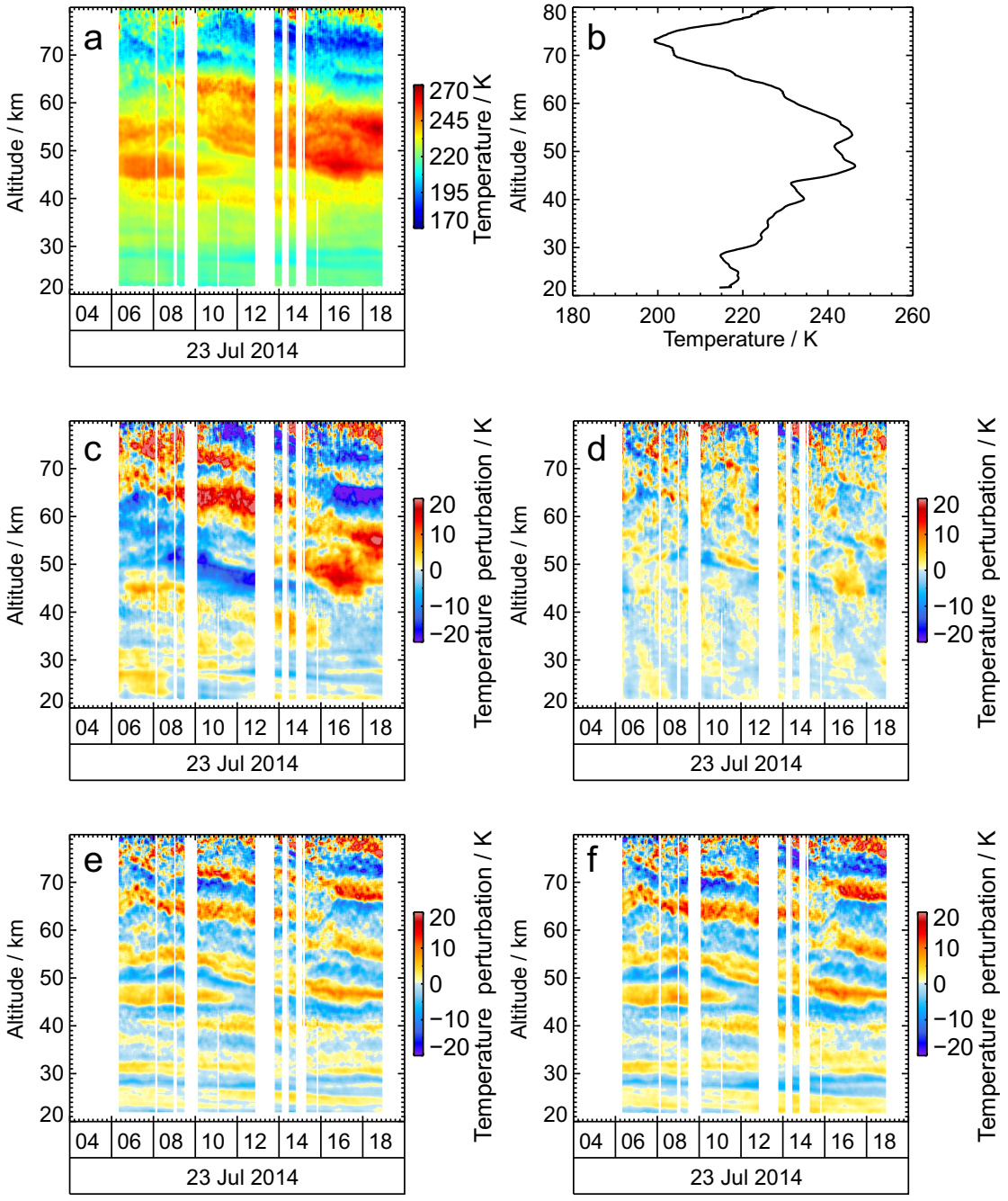

Figure 3.6: Temperature (a), mean temperature profile (b) and derived temperature perturbations obtained by different methods (c)–(f) over Lauder, New Zealand, (45.0° S, 169.7° E) on 23 July 2014. The following methods were used for the different panels: Nightly mean (c), 3 h running mean (d), sliding polynomial fit (e), Butterworth filter (f). Time is given in UTC.

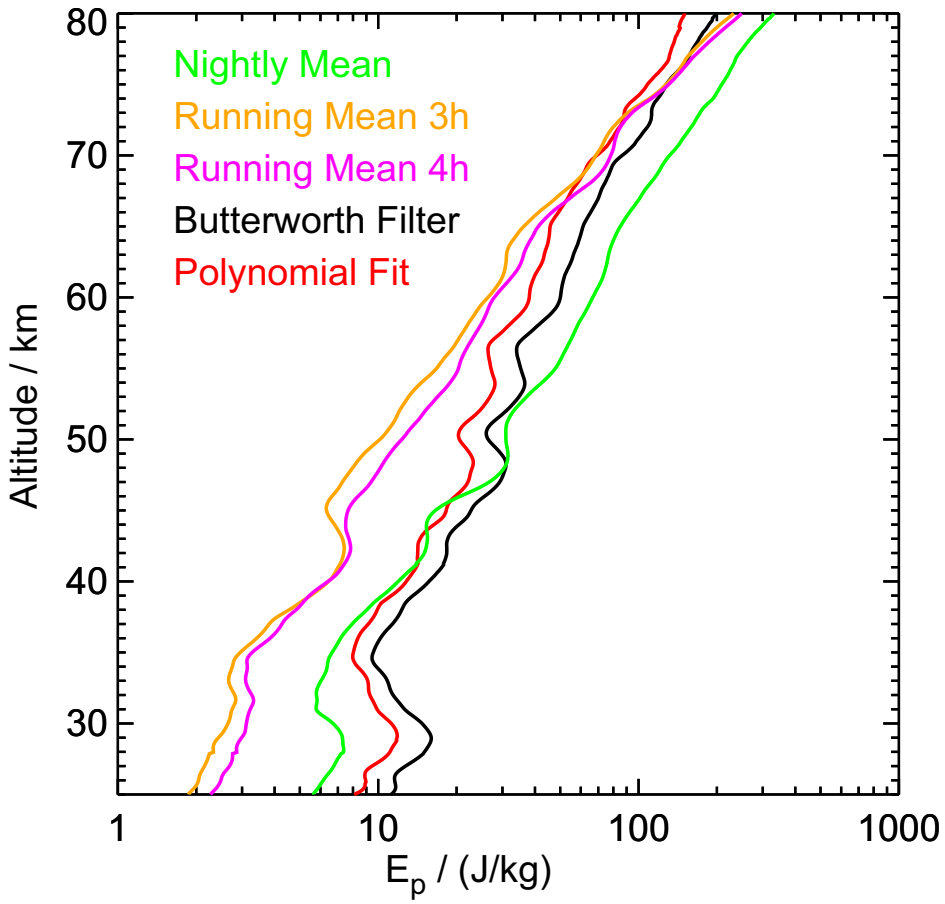

Figure 3.7: Mean gravity wave potential energy density E_p per mass over Lauder, New Zealand, (45.0° S, 169.7° E) between 1 July and 30 September 2014. The methods used to determine E_p are color coded. The profiles were smoothed by a vertical running mean with a window width of 3 km.

produce similar results. A distinct feature of Fig. 3.7 is the larger growth of E_p with altitude if the running mean method is used instead of the vertical filtering methods. Additionally, the 3 h running mean method yields the lowest E_p values. Application of the 4 h running mean shifts the E_p profile towards slightly larger values. Below 45 km altitude the nightly mean method produces values comparable to the sliding polynomial fit and the Butterworth filter. Above 45 km altitude the nightly mean method shows the largest values of all methods. The sliding polynomial fit and the Butterworth filter produce generally similar results, with the Butterworth filter yielding a slightly larger E_p. Another striking feature in Fig. 3.7 is the increase of E_p below 35 km altitude which is detected by both vertical filtering methods. This increase is not detected by the running mean method.

3.4 Discussion

3.4.1 Temporal filters

The nightly mean method has been applied in many studies (e.g. *Gardner et al.*, 1989; *Blum et al.*, 2004; *Rauthe et al.*, 2008; *Ehard et al.*, 2014). The major disadvantage is that a varying length of measurement periods results in a variation of the sensitivity to different timescales. This effect is clearly demonstrated in Fig. 3.3e showing that gravity waves with periods larger than 10 h are significantly underestimated if an 8 h long timeseries is used. If the timeseries is shortened, the cutoff period is smaller as well (not shown) and the spectral response for long period waves is reduced even further. Strictly speaking, this implies that gravity wave analyses of timeseries of different length cannot be compared.

In practice measurement periods vary typically in length between a few hours up to a whole night as weather conditions can change rapidly during an observational period. Moreover, there is a seasonal dependency because most middle atmospheric lidars are capable of measuring in darkness only. This results in shorter measurement periods in summer and longer measurement periods in winter. Hence, the nightly mean method is sensitive to different parts of the gravity wave spectrum depending on weather conditions as well as season. For example, *Rauthe et al.* (2006) compared winter and summer measurements of gravity wave activity determined by the nightly mean method. Their winter measurements were restricted to observational periods of 1.5 h to 12 h and the summer measurements to observational periods of 1.5 h to 3.5 h. Hence, *Rauthe et al.* (2006) limited their analysis to 3 h to 5 h long measurement periods in order to reduce the variation of the spectral response.

The use of the nightly mean method in gravity wave analysis is further complicated by the fact that there are processes besides gravity waves which occur on similar timescales. For example tides with periods of 8, 12 and 24 h are within the sensitivity range of this method. In the analysis of radar data, the removal of tidal signals is a standard procedure (e.g. *Hoffmann et al.*, 2010). With lidar data, however, this is problematic due to generally shorter and often intermittent measurement periods. Figure 3.6c shows an example of a tidal signal extracted with the nightly mean method. The broad descending maximum in temperature perturbations is caused by the semidiurnal tide. Note, that the nightly mean method is not a suitable method for tidal analysis. Tidal signals are generally extracted from lidar measurements by means of a composite analysis (e.g. *Lübken et al.*, 2011).

The running mean method (e.g. *Yamashita et al.*, 2009) tries to compensate for some of the shortcomings of the nightly mean method. The spectral response is limited to timescales on the order of the window width of the running mean – which is typically 3 h – resulting in the suppression of tides and planetary waves. However, due to this

limitation, only a very small part of the gravity wave spectrum is retained in the analysis (e.g. Fig. 3.3e). As stated previously, gravity wave periods can range from about 5 min to 17 h. Thus the limitation to short timescales excludes a major part of the gravity wave spectrum. Figure 3.7 shows that as the length of the running mean window increases, E_p increases as well. Still, gravity waves with long periods are suppressed. Additionally, the running mean method overestimates periods slightly shorter than the chosen window width and shows aliasing effects for even shorter periods (Fig. 3.3e).

The beginning and the end of the measurement period poses an additional problem for the application of the running mean method. At the beginning of the measurement period, a centered running mean of 3 h lacks the first 1.5 h of observations necessary for determining the background temperature. Thus, if in the beginning of the measurement only 1.5 h of data are available for averaging, the spectral response differs at the beginning of the measurement period compared to later times when 3 h of measurements are available. The same is true at the end of the measurement period as well as in the presence of measurement gaps. Thus, when requiring the same spectral response at all times, the "spin-up" time of the running mean method would have to be discarded. However, this would result in a significantly reduced dataset because one window width of data would have to be discarded from each measurement period, in addition to another window width for each measurement gap.

Note, that the resolved high frequency range of the gravity wave spectrum is limited by the sampling frequency of the lidar system which ranges typically between 10 min and 1 h, depending on lidar performance. This is a fundamental limitation to the extractable part of the gravity wave spectrum which affects all methods of extracting gravity wave induced temperature perturbations in the same way. The same holds true for the effective vertical resolution of the temperature profiles.

3.4.2 Spatial filters

Filtering in the spatial domain, either by using the sliding polynomial fit or the Butterworth filter, has the advantage that the spectral response in the time domain is independent of the length of the measurement period and the presence of measurement gaps. This makes it possible to derive temperature perturbations associated with gravity waves from observational periods which are too short to yield meaningful results if temporal filtering methods are applied. In addition, both spatial filtering methods are capable of detecting waves with periods larger than 12 h (Fig. 3.3c and d).

The sliding polynomial fit has been applied in several studies (e.g. *Duck et al.*, 2001; *Alexander et al.*, 2011; *Kaifler et al.*, 2015a). Different authors use temperature data with different altitude resolutions and slightly different parameter setups for L_f, L_w

and γ. The fit length L_f determines the cutoff wavelength of the spectral response. The weighting window length L_w and the e-folding width γ must be adapted to the altitude resolution of the data used. For example, the parameter setup $\gamma = 3\,\mathrm{km}$ and $L_\mathrm{w} = L_\mathrm{f}/3$ used by *Duck et al.* (2001) results in a flat spectral response for their altitude resolution of $\Delta z = 2\,\mathrm{km}$ and fit length $L_\mathrm{f} = 25\,\mathrm{km}$. If a different altitude resolution is chosen, a different set of parameters is needed in order to achieve a flat spectral response in the passband. For the altitude resolution of $\Delta z = 0.1\,\mathrm{km}$ used in this thesis, a flat spectral response was found for $\gamma = 9\,\mathrm{km}$ and $L_\mathrm{w} = 3\,\mathrm{km}$. The fit length of $L_\mathrm{f} = 20\,\mathrm{km}$ was chosen following *Kaifler et al.* (2015a). Additional high-pass filtering, as applied by *Alexander et al.* (2011) or *Kaifler et al.* (2015a), was found to be unnecessary because the long vertical wavelengths are already strongly suppressed by the sliding polynomial fit itself.

The sliding polynomial fit method is sensitive to large changes of the temperature gradient and may falsely overestimate temperature perturbations for example in the presence of mesospheric inversion layers (not shown). The Butterworth filter tends to overestimate sudden changes in the temperature gradient of the measured temperature profile as well. However, the magnitude of the overestimation is generally lower than for the sliding polynomial fit method. Furthermore, the Butterworth filter has the advantage that it can be easily adjusted if a different cutoff wavelength is desired, since its spectral response is independent of the altitude resolution of the analyzed data.

However, one general issue of spatial filtering methods remains: Since the vertical wavelength of gravity waves is proportional to the horizontal wind speed, the extracted gravity wave activity with a spatial filter is depending on the horizontal wind speed as well. Thus, when comparing measurements during different seasons or from different stations, it should be kept in mind that depending on wind conditions different amounts of wave activity will be extracted from the observations when using spatial filtering techniques.

3.4.3 Application to measurement data

All the previously discussed characteristics influence the gravity wave spectrum which is extracted from lidar temperature measurements. This becomes visible if the mean E_p of a set of measurements is computed using different methods as shown in Fig. 3.7. The running mean method extracts only a small part of the gravity wave spectrum and thus shows the lowest E_p values. E_p increases if the window width of the running mean is increased. The nightly mean method yields the largest E_p values at higher altitudes. This can be attributed to the insufficient suppression of tides and other processes unrelated to gravity waves which happen on longer timescales. In the lower stratosphere the sliding polynomial fit method and the Butterworth filter yield the largest E_p values. This is most likely caused by the inclusion of long period waves such

as quasi-stationary mountain waves. These waves have the largest impact on E_p in the lower stratosphere above Lauder during winter (*Kaifler et al.*, 2015b). Above 30 km altitude E_p is reduced. A possible mechanism is that mountain waves with very large amplitudes become unstable at these altitudes and break. This has for example been observed by *Ehard et al.* (2015) who detected a self-induced critical layer around 30 km altitude caused by a strong mountain wave event above northern Scandinavia.

The fact that the Butterworth filter exhibits a lower growth rate of E_p compared to the running mean method (Fig. 3.7) may by evidence that short period gravity waves can propagate more easily to higher altitudes than gravity waves with long periods. This complicates the comparison and interpretation of E_p growth rates (generally expressed in terms of scale heights) of different studies. For example *Rauthe et al.* (2006) deduced an E_p scale height of 9 km to 11 km with the nightly mean method for a mid-latitude site. On the other hand, *Kaifler et al.* (2015a) reported an E_p scale height of approximately 7 km determined with the sliding polynomial fit method for measurements conducted at Antarctica. A large part of the difference in retrieved scale height can be attributed to different wave propagation conditions at the two sites. However, it remains an open question in how far the results are affected by the use of different methods to extract gravity waves.

3.5 Conclusions

Four commonly used methods of extracting gravity wave induced temperature perturbations from lidar measurements were examined. A widely used method – the nightly mean method – relies on filtering in time by subtraction of the nightly mean temperature. Thereby, it is sensitive to all temperature changes occurring on the timescale of the measurement period including temperature changes induced by planetary waves and tides. Because measurement periods can vary substantially in length and the spectral response of the nightly mean method depends on the length of the measurement period, the extracted gravity wave spectrum can vary from observation to observation. This makes the nightly mean method an improper choice for compiling gravity wave statistics.

The second method which relies on filtering in time, the running mean method, provides a more stable spectral response with regard to a varying length of the measurement period. However, it extracts only a small fraction of the gravity wave spectrum, with long period waves being strongly suppressed. Moreover, the running mean method exhibits a variation in the spectral response at the beginning and end of a measurement period as well as in the presence of measurement gaps.

The sliding polynomial fit method is not only capable of extracting waves over a broad range of temporal scales but also suppresses tides and planetary waves due to their

large vertical wavelengths. In addition, it is unaffected by measurement gaps. However, the parameters used for the sliding polynomial fit need to be adjusted to the altitude resolution of the measured temperature profiles in order to provide a flat spectral response in the passband.

The Butterworth filter provides an alternative to the sliding polynomial fit method which is not only easy to implement but also easily adjustable to a desired cutoff wavelength. Also, the filter is largely independent of the altitude resolution while providing all the advantages of the sliding polynomial fit method. Furthermore, sudden changes in the background temperature gradient affect the Butterworth filter less than the sliding polynomial fit method.

Based on the results presented here, two methods are recommended for gravity wave extraction from lidar temperature measurements: the running mean method is the most suitable method if the analysis is focused on short period gravity waves with large vertical wavelengths. Moreover, the running-mean method is largely insensitive to changes of the background horizontal wind field. The gravity wave activity extracted by the Butterworth filter on the other hand can be affected by changes of the horizontal wind field. The Butterworth filter is the method of choice if a broad passband is desired which covers a large part of the gravity wave spectrum. Additional advantages are the insensitivity to measurement gaps, a varying length of observational periods and the altitude resolution of the measured temperature profile. This results in the Butterworth filter being the most robust method for extracting gravity waves from middle atmospheric lidar measurements. Furthermore, mountain waves are generally associated with zero ground based vertical phase velocity and thus an infinite ground based period. Hence, they cannot be extracted by temporal filtering methods such as the running mean method but mountain waves can be extracted by spatial filtering methods, e.g. the Butterworth filter. Because this thesis focuses on the propagation of mountain waves, the 5-th order Butterworth filter with a cutoff wavelength of 15 km is used for gravity wave extraction throughout the rest of this thesis.

4 Capability of resolving middle atmospheric dynamics by the ECMWF IFS

The observational geometry of a ground-based Rayleigh lidar system makes it difficult to interpret the lidar measurements in respect to gravity waves, since all measurements are taken in a purely vertical column and lack all information about the horizontal dimension. As a consequence, the question whether horizontal propagation of mountain waves occurs, cannot be assessed by studying lidar measurements alone. A possibility to assess the horizontal dimensions is to combine the lidar data with modeling data.

Here, data from the integrated forecast system (IFS) of the European Centre for Medium-Range Weather Forecasts (ECMWF) is used for this purpose. Before the model data can be used for gravity wave studies, it has to be evaluated to what extent the ECMWF IFS is capable of resolving middle atmospheric dynamics. This is done in the following by comparing measurements taken by TELMA and CORAL at mid- and high-latitudes during wintertime to ECMWF IFS data

4.1 The ECMWF IFS model

The ECMWF IFS is a hydrostatic global semi-implicit, semi-Lagrangian numerical weather prediction model. The cycle[1] 40r1 which has been operational from 19 November 2013 until 12 May 2015 utilized a linear Gaussian grid with a triangular spectral truncation at wavenumber 1279 (T_L1279) which corresponds to a horizontal resolution of approximately 16 km. In the vertical 137 levels (L137) ranged from the model top at a pressure level of 0.01 hPa (model level 1, roughly 80 km altitude) down to the surface (model level 137). The vertical resolution (Fig. 4.1) is quite coarse in the mesosphere (≈ 2 km) and increases with decreasing altitude.

To avoid wave reflection at the model top, the ECMWF IFS utilizes a sponge layer which dampens wave motions above model level 30 (10 hPa, see Fig. 4.1). Between

[1] See http://www.ecmwf.int/en/forecasts/documentation-and-support/changes-ecmwf-model/ifs-documentation for the detailed documentation of the specific ECMWF IFS cycles.

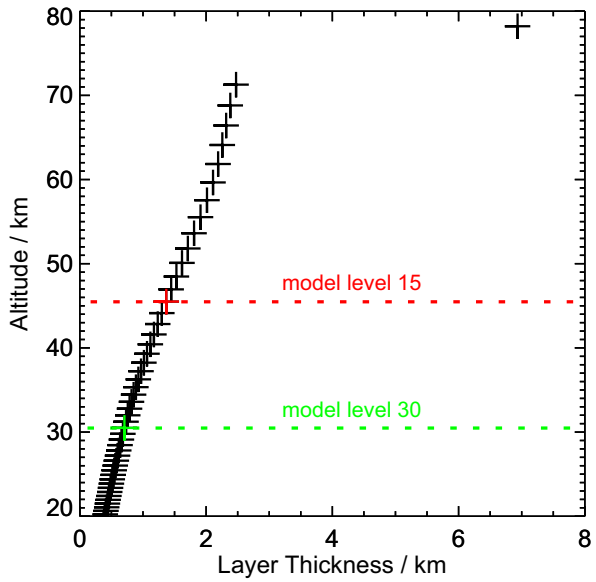

Figure 4.1: Mean model level thickness as a function of altitude of the ECMWF IFS cycle 40r1 (T_L1279, L137) above Lauder during July to September 2014. The red dashed line/cross and green dashed line/cross mark the model levels 15 and 30 (1 hPa, 10 hPa), respectively.

model level 30 and 16, the sponge layer acts only on the shortest horizontal scales within the divergence field of the ECMWF IFS and the damping is very weak (S. Malardel, personal communication). At model level 15 (1 hPa), the so called "hard sponge layer" sets in, which acts on the divergence and the vorticity fields. The damping strength of the hard sponge layer increases quickly with increasing altitude and the scales on which the damping acts increase as well.

Since many physical processes cannot be directly resolved by the ECMWF IFS, parametrizations are introduced to incorporate the effects of these processes, such as convection (*Tiedtke*, 1989; *Bechtold et al.*, 2014), or surface drag and unresolved orographic gravity waves (*Lott and Miller*, 1997; *Beljaars et al.*, 2004). Moreover, a parametrization for non-orographic gravity waves was implemented in the ECMWF IFS in September 2009 which considerably improved the representation of the middle atmosphere (*Orr et al.*, 2010).

4.2 Previous studies examining the ECMWF IFS in the middle atmosphere

The middle atmospheric thermal and dynamical state simulated by the ECMWF IFS was recently investigated by *Le Pichon et al.* (2015). They compared wintertime ground based lidar temperature and wind radiometer measurements conducted at Haute de Provence Observatory (43.9° N, 5.7° E) to the ECMWF IFS cycle 38r2 (T_L1279, L137). They found good agreement in the stratosphere between the ECMWF IFS model and the observations. However, above 60 km altitude, ECMWF IFS temperatures were lower than the measurements (e.g. 10 K at 65 km altitude), while the ECMWF IFS zonal winds were larger than the measurements (e.g. 20 m s^{-1} at 65 km altitude).

Other studies examining the ECMWF IFS in the middle atmosphere focused on the resolved gravity waves directly. One of the first studies comparing stratospheric gravity waves from operational ECMWF IFS analyses with radiosonde observations over the North Atlantic was conducted by *Plougonven and Teitelbaum* (2003). Their radiosonde observations showed large scale inertia gravity waves excited at a jet exit region, which were in agreement with alternating divergence patterns simulated by the ECMWF IFS. However, they noted that the wave amplitude and horizontal wavelength were not well represented by the model, which they attributed to the coarse vertical and horizontal resolution (60 pressure levels up to 1 hPa and 50 km horizontal resolution) at that time. Since then, the horizontal and vertical resolution of the ECMWF IFS has steadily increased over the years (*Bauer et al.*, 2015) and a number of studies have been conducted to compare further observations to the model.

For example, *Wu and Eckermann* (2008) and *Schroeder et al.* (2009) compared satellite measurements of gravity wave activity to the ECMWF IFS model with a resolution of T_L799, L91. Both studies found that the satellite measurements and the model show similar global patterns of gravity wave activity in the stratosphere. However, *Schroeder et al.* (2009) noted that gravity wave amplitudes are too low by a factor of 2 and a Rayleigh damping layer started to damp the gravity waves in the ECMWF IFS above 40 km altitude.

An examination of gravity waves resolved by the ECMWF IFS T_L799, L91 was also carried out by *Preusse et al.* (2014), who applied backward raytracing from 25 km altitude to infer properties and sources of the resolved gravity waves. One of their findings was that the ECMWF IFS underestimates the short horizontal wavelength gravity waves from convective regions, while it overestimates the long horizontal wavelength gravity waves. Furthermore, they noted that tropical gravity waves resolved by the ECMWF IFS on average have too slow horizontal phase speeds.

Another comparison was conducted by *Jewtoukoff et al.* (2015): They compared gravity wave momentum fluxes in the lower stratosphere (at 70 hPa) derived from long duration

superpressure balloon flights around Antarctica to the ECMWF IFS T_L1279, L91. They found that the horizontal structure and intermittency of the ECMWF IFS momentum fluxes agree well with the balloon observations. However, the ECMWF IFS model underestimates the momentum flux values by a factor of 5.

4.3 Comparing the ECMWF IFS to lidar temperature measurements above New Zealand

In the following the ECMWF IFS cycle 40r1 temperature profile is compared to lidar temperature measurements by TELMA above Lauder, New Zealand, during July to September 2014. For the comparison 6 hourly analysis and 1 hourly short-term forecast[2] data are combined to create a continuous hourly data set from the ECMWF IFS cycle 40r1. The comparison is limited to July to September 2014, because the data coverage by the lidar is best during these months (*Kaifler et al.*, 2015b, their Fig. 1). In total 441 h of lidar observations are used for the following comparison.

To enable a direct comparison, the ECMWF IFS temperature data is interpolated horizontally to the position of the lidar (45.0° S, 169.7° E). Furthermore, the ECMWF IFS data is interpolated on a regular vertical grid with a resolution of 500 m, ranging from 0.5 km to 75 km altitude. The lidar temperature data with an effective resolution of 2900 m × 10 min is averaged over one hour and the resulting profiles are interpolated to the same altitude grid as the ECMWF IFS data. As a result of the averaging, the temperature uncertainty of the lidar data is expected to decrease by a factor of $\sqrt{6} \approx 2.4$. The coarse resolution of the lidar data (2900 m) was thereby motivated by the fact that on average the best agreement between the ECMWF IFS and the lidar data was found for this resolution.

In the following the comparison between the ECMWF IFS and the lidar is limited to the altitude range 30 km to 70 km. The lower limit is chosen due to the likely presence of aerosols below this altitude, resulting in unreliable lidar temperatures. The upper limit was chosen because only two ECMWF IFS model levels are located above this altitude (cf. Fig. 4.1), resulting in a considerably lower effective vertical resolution of the ECMWF IFS compared to altitudes lower than 70 km.

4.3.1 Mean thermal state of the ECMWF IFS

The mean temperature of the ECMWF IFS cycle 40r1 above Lauder from July to September 2014 and the corresponding lidar temperature profile are shown in Figure 4.2a

[2]Forecasts with lead times +1, +2, +3, +4, +5, +7, +8, +9, +10, +11 h from the 00 UTC and 12 UTC runs are taken to fill the times between the analysis times 00, 06, 12, and 18 UTC.

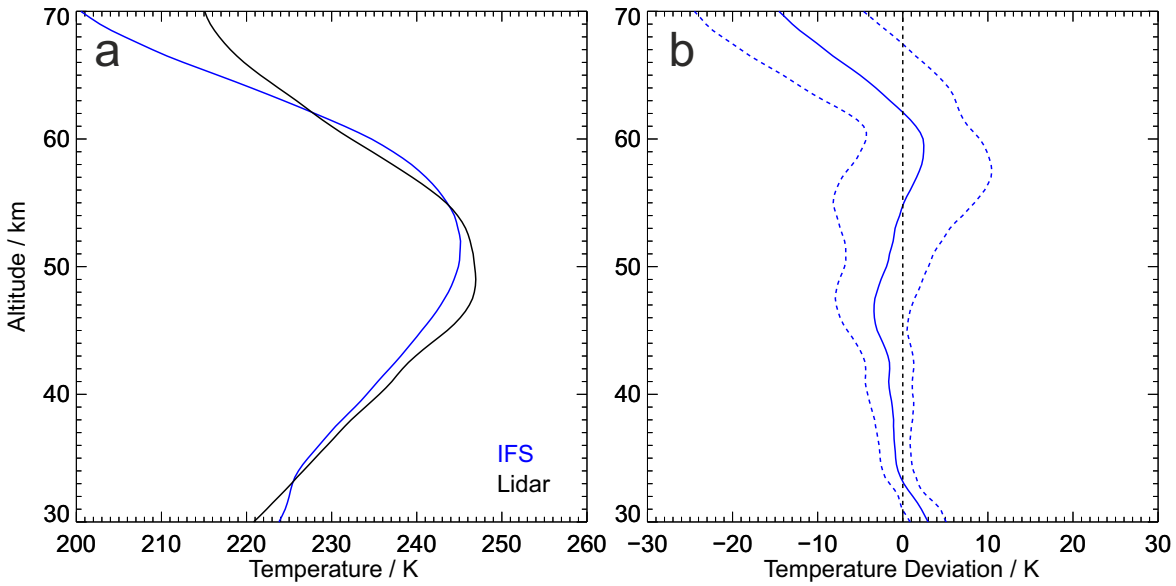

Figure 4.2: Left panel: Mean temperature over Lauder, New Zealand, from July to September 2014 measured by TELMA (black) and simulated by the ECMWF IFS (blue). Right panel: Temperature difference between the ECMWF IFS and the lidar measurements (solid) and standard deviation of the mean difference (dashed lines). Only ECMWF IFS profiles with simultaneous lidar measurements were used.

(see also Appendix A1 by *Gisinger et al.*, 2017). For this comparison only ECMWF IFS profiles with simultaneous lidar measurements were used. The lidar temperature profile exhibits a mean stratopause height of ≈ 48 km with a stratopause temperature of 247 K. In the mesosphere, the temperature decreases with altitude, reaching 215 K at 70 km altitude. The ECMWF IFS profile shows a higher and colder stratopause (52 km, 245 K) than the lidar measurements. In the mesosphere, temperatures decrease rapidly with increasing altitude, reaching 200 K at 70 km altitude. Between 30 and 34 km altitude lidar temperatures are on average lower than ECMWF temperatures. Note, that lidar temperatures in this altitude region might be low biased due to the presence of stratospheric aerosols. Thus, this altitude region is not further considered here.

The deviation between ECMWF IFS cycle 40r1 temperature and the lidar temperature (Fig. 4.2b) shows that ECMWF IFS temperatures are only 1 K to 3 K lower than the lidar temperatures between 34 km and 54 km altitude. At 60 km altitude, ECMWF IFS temperatures are slightly higher (2 K) than the lidar temperatures. Above 60 km altitude the magnitude of the temperature deviation increases rapidly with altitude, resulting in ECMWF temperatures being 15 K lower than the lidar temperatures at 70 km altitude. The standard deviation of the temperature deviation is small in the

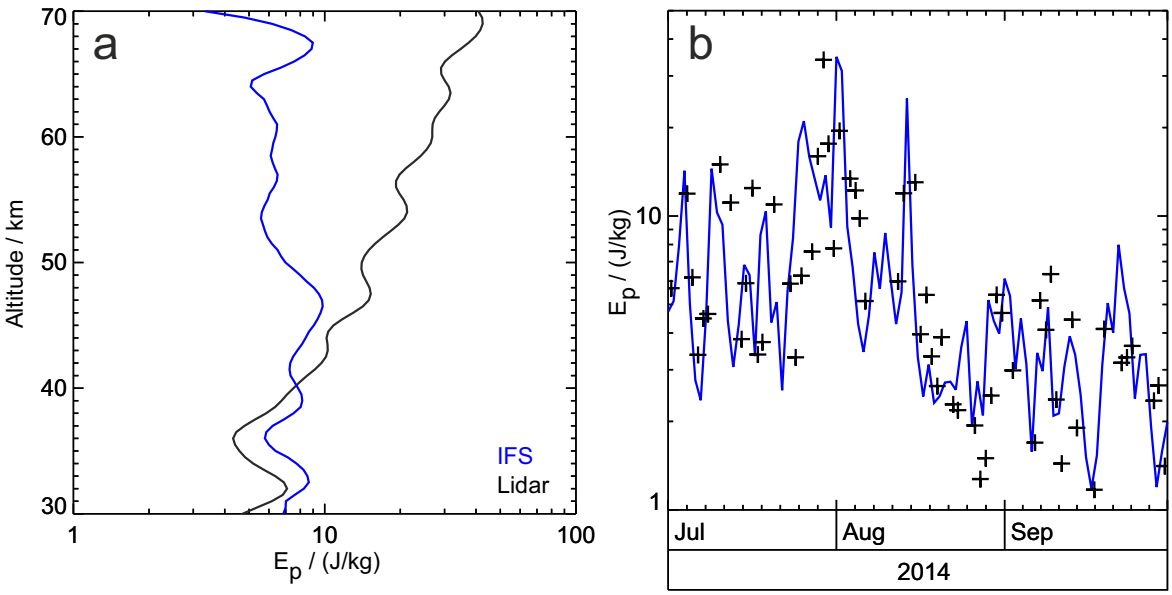

Figure 4.3: Left panel: Mean gravity wave potential energy density E_p above Lauder, New Zealand, from July to September 2014 derived from TELMA measurements (black) and ECMWF IFS simulations (blue). Only ECMWF IFS profiles with simultaneous lidar measurements were used. Right panel: Daily mean E_p between 30 and 40 km altitude over Lauder derived from TELMA measurements (black crosses) and ECMWF IFS simulations (blue line). Here all ECMWF IFS profiles above Lauder from July to September 2014 were used.

stratosphere (≈ 3 K) and increases up to 10 K in the mesosphere.

The temperature deviation profile at Lauder is very similar to the results published by *Le Pichon et al.* (2015) (their Fig. 4), who compared data from the ECMWF IFS cycle 38r2 to ground-based lidar measurements taken at a northern hemisphere mid-latitude site (Haute de Provence Observatory, 43.9° N, 5.7° E). They showed that the ECMWF IFS data agrees well with the lidar observations up to 60 km altitude. Up to the same altitude, the authors found good agreement between the horizontal wind of the ECMWF IFS and wind radiometer measurements (their Fig. 7). The fact that similar results were obtained a mid-latitude site in the northern and southern hemisphere suggests that the ECMWF IFS can be regarded as a good indicator for the mean thermal state of the atmosphere at mid-latitudes up to 60 km altitude.

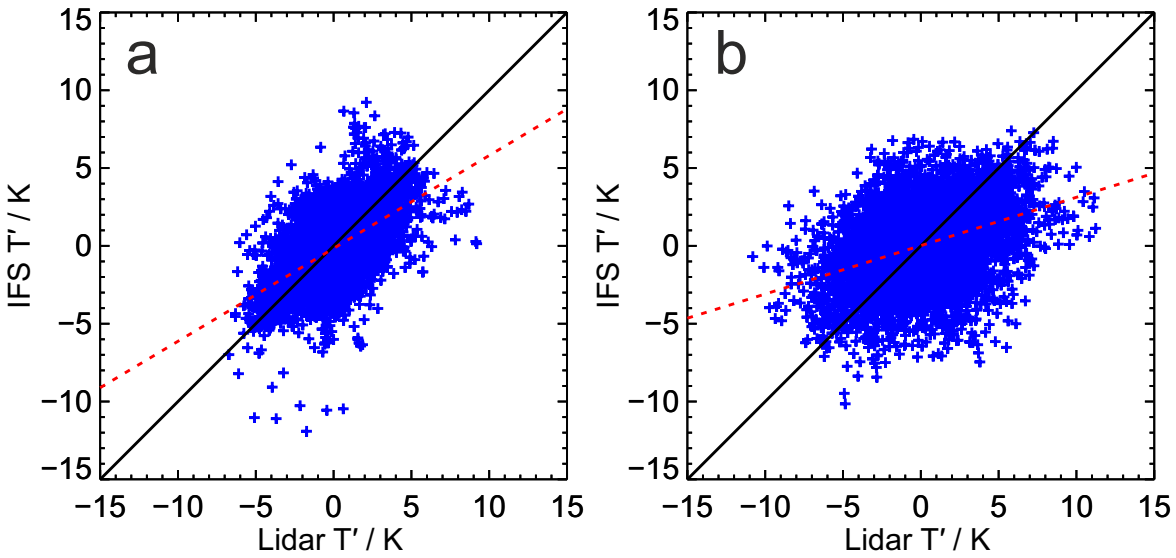

Figure 4.4: Temperature perturbations T' from July to September 2014 derived from TELMA measurements and ECMWF IFS simulations between 30 and 40 km (left panel) and 40 and 50 km altitude (right panel). The black line marks the points where lidar and ECMWF IFS T' are identical. The red dashed line depicts a linear regression. Only ECMWF IFS profiles with simultaneous lidar measurements were used.

4.3.2 Gravity waves resolved by the ECMWF IFS

To test in how far gravity waves are explicitly resolved by the ECMWF IFS, the mean E_p profiles from July to September 2014 derived from the ECMWF IFS and the lidar measurements were calculated (Fig. 4.3a). Only ECMWF IFS profiles with simultaneous lidar observations were used. Both profiles show similar patterns below 40 km altitude. While the lidar E_p increases steadily with altitude above 40 km, the corresponding ECMWF IFS profile remains almost constant. This leads to an increasing deviation between the two E_p profiles, the difference reaching a factor of 4 around 50 km altitude. Note, that the possible low bias of lidar temperatures below 34 km altitude does not substantially influence the calculation of E_p since the dominant contributor to E_p are the temperature perturbations T' which are unaffected by a constant temperature offset. This was verified by recalculating the lidar E_p using the lidar T' and the mean temperature T_0 and N^2 derived from the ECMWF IFS data (cf. Eq. 2.10). While the absolute values of the original and the recalculated E_p profile differ slightly below 34 km, all qualitative features remain.

To examine in how far the ECMWF IFS is capable of reproducing the temporal evolution of gravity wave activity, the daily mean E_p between 30 and 40 km altitude

derived from lidar and ECMWF IFS data is shown in Figure 4.3b. In order to be able to depict a continuous timeline all ECMWF IFS data from July until September 2014 was used. It can be seen that the ECMWF IFS is capable of reproducing several key features of the wave activity above Lauder during winter 2014: The increase of E_p towards the end of July/beginning of August and the decrease of E_p afterwards, as well as the spike in mid August and the following reduction of E_p by an order of magnitude until the beginning of September, are all well resolved by the ECMWF IFS. Also the sudden increase and the following slow decrease of E_p during the second half of September 2014 is well captured by the ECMWF IFS.

Comparing the hourly temperature perturbation profiles from July to September 2014 derived from the ECMWF IFS and the lidar data, it can be seen that both data sets show a better agreement between 30 and 40 km altitude (Fig. 4.4a) than between 40 and 50 km altitude (Fig. 4.4b). The linear Pearson correlation coefficient is 0.57 between 30 and 40 km altitude and 0.39 between 40 and 50 km altitude. A linear regression results in a slope of 0.60 and 0.31, respectively.

Because the mean E_p values of the ECMWF IFS between 30 and 40 km altitude agree well with the lidar observations, the regression slope of 0.60 and the correlation coefficient of 0.57 both indicate that while the mean gravity wave amplitude is well captured by the ECMWF IFS, the simulated gravity waves are sometimes out of phase with the lidar observations. At 40 km to 50 km altitude, decreasing correlation and the decreasing regression slope indicate that both the phase shift between simulated and observed waves increases and the amplitude of the simulated gravity waves decreases as well.

A remarkable case demonstrating the ability of the ECMWF IFS to resolve middle atmospheric gravity waves is presented in Figure 4.5. Differing from the previous comparisons, TELMA measurements with an effective resolution 900 m × 10 min are shown. Figure 4.5 depicts large amplitude gravity waves observed by TELMA within the stratosphere on 1 August 2014 . The ECMWF IFS shows similar gravity wave temperature perturbation patterns up to 50 km altitude. The phase of the gravity waves simulated by the ECMWF IFS is almost identical to the lidar measurements, while the ECMWF IFS amplitude is lower by a factor of 2. However, when using coarser resolved lidar temperature data (2900 m in the vertical[3], compared to a vertical model level resolution of ≈ 1.2 km, cf. Fig.4.1), the amplitudes of the ECMWF IFS and the lidar match almost perfectly. Within the altitude range of 30 km to 40 km (40 km to 50 km), this results in a regression slope of 0.99 (0.77) and a correlation coefficient of 0.66 (0.81). At altitudes above 50 km the ECMWF IFS shows negligible temperature perturbations amplitudes, which are uncorrelated with the lidar measurements.

In summary, it can be said that the IFS is capable of resolving gravity waves to a

[3]this is the same resolution as used in the previous comparisons

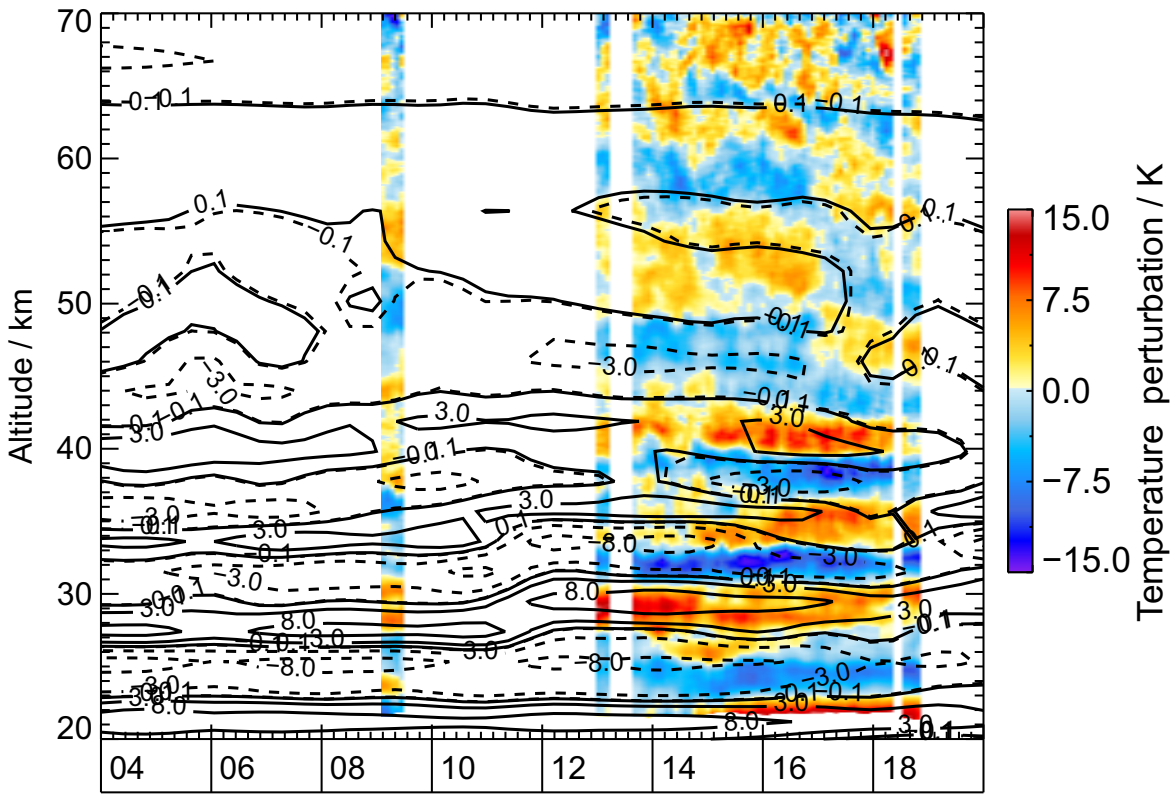

Figure 4.5: Temperature perturbations derived from TELMA measurements (color coded) and ECMWF IFS simulations (black contours) above Lauder, New Zealand, on 1 August 2014. Here TELMA measurements with an effective resolution of 900 m × 10 min were used. ECMWF IFS temperatures were interpolated to a regular altitude grid with 500 m vertical resolution.

great detail below 40 km altitude, where the amount and the temporal evolution of gravity wave potential energy E_p was comparable to lidar measurements at Lauder, New Zealand. At higher altitudes, gravity waves are strongly damped and hence actively removed from the ECMWF IFS simulations due to the presence of the "hard sponge layer". For the case on 1 August 2014, it was demonstrated that even the phase of the simulated gravity waves is in agreement with the lidar measurements. However, not all observations in the time frame July to September 2014 show such a good agreement. In fact, on several days the ECMWF IFS temperature perturbation fields are almost completely uncorrelated with the lidar measurements. An example of such a case is shown for 17 August 2014 in Figure 4.6. Here the correlation coefficient in the altitude range 30 km to 40 km (40 km to 50 km) is −0.03 (0.07). It was tested whether the varying skill of resolving gravity waves by the ECMWF IFS was correlated with the amplitude or the excitation and propagation conditions of the gravity waves.

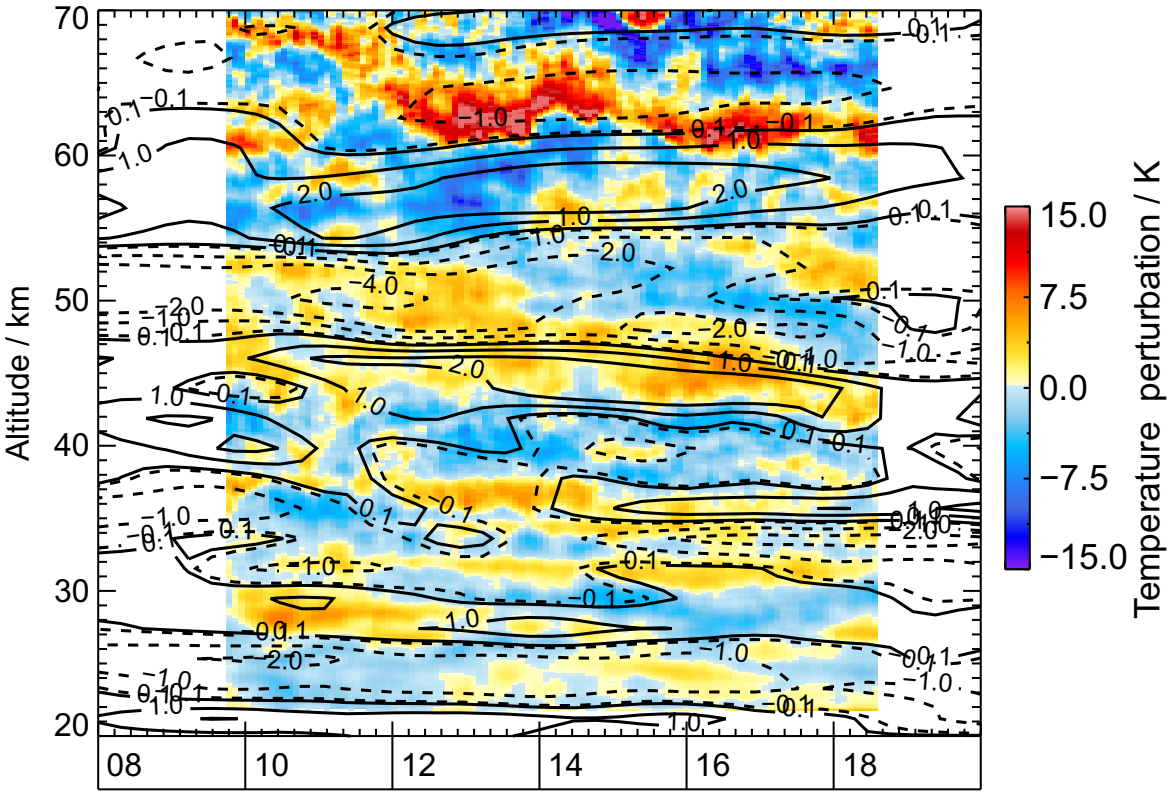

Figure 4.6: Same as Figure 4.5 but for 17 August 2014.

However, these investigations were inconclusive. Hence, the cause for this varying skill of resolving gravity waves by the ECMWF IFS remains unknown.

4.4 The ECMWF IFS horizontal resolution upgrade on 9 March 2016

On 9 March 2016 the new ECMWF IFS cycle 41r2 became operational which changed the grid of the ECMWF IFS from a linear Gaussian grid with triangular spectral truncation to an octahedral grid with a cubic spectral truncation (*Hólm et al.*, 2016). While the spectral resolution remained at wavenumber 1279, the horizontal resolution increased from 16 km to approximately 9 km. This increase of horizontal resolution resulted in a better representation of small scale motions such as gravity waves by the ECMWF IFS (*Malardel and Wedi*, 2016). Since gravity waves have a large influence on the middle atmosphere, it is expected that a better resolved gravity wave spectrum results in more wave drag within the middle atmosphere. More wave drag should yield

higher temperatures simulated by the ECMWF IFS in the middle atmosphere during wintertime, due to an enhanced downwelling over the winterpole.

This hypothesis is investigated by examining data from the operational ECMWF IFS cycle 41r1 with the linear Gaussian grid and the experimental Suite 69 with the cubic octahedral grid (which became cycle 41r2 on 9 March 2016), both with a spectral truncation at wavenumber 1279. In the following the grid and spectral resolution are abbreviated as T_L1279 and $T_{Co}1279$ for cycle 41r1 and the experimental Suite 69, respectively. Both simulations ran parallel from December 2015 until 8 March 2016. Here ECMWF IFS data is compared to Rayleigh lidar temperature measurements by the CORAL lidar conducted from October 2015 to April 2016 in Sodankylä, Finland (67.4° N, 26.6° E) (*Kaifler et al.*, 2017). Only data from December 2015 is used for the comparison, since the data coverage by the CORAL lidar is best during December 2015. The Rayleigh lidar data had a resolution of 2970 m × 10 min. Otherwise, the comparison was undertaken in the same way as described in the previous section.

4.4.1 Evaluating the high-resolution ECMWF IFS

Figure 4.7a shows the mean temperature profile of both the operational ECMWF IFS and the experimental Suite (e-Suite) 69 in comparison to the CORAL lidar data during December 2015. Here only ECMWF IFS profiles with simultaneous lidar measurements were used. The CORAL temperature profile depicts a very broad stratopause between 46 and 58 km altitude with a mean stratopause temperature of 263 K. The operational ECMWF IFS cycle simulates mean stratopause at 50 km altitude with a slightly lower temperature of 257 K. The e-Suite with $T_{Co}1279$ simulates a very sharp stratopause at 48 km altitude with a temperature of 258 K. Above the stratopause, all three data sets show decreasing temperatures in the mesosphere, with the operational ECMWF IFS cycle having the smallest absolute temperature gradient.

Figure 4.7b reveals a remarkable agreement between the operational ECMWF IFS cycle and the lidar data up to an altitude of 44 km (blue line). Within the stratopause region, the operational ECMWF IFS simulates temperatures which are too low by approximately 7 K, while above 65 km altitude the simulated temperatures are slightly too large. The e-Suite 69 (red line, Fig. 4.7b) shows a very good agreement below 41 km altitude. At 43 km altitude the e-Suite 69 temperatures are slightly too large (3 K). Above this altitude, the temperature deviation increases in magnitude and the e-Suite 69 reaches a maximum cold bias of 19 K around 60 km altitude. Above 60 km altitude, the cold bias decreases in magnitude, reaching 8 K at 70 km altitude. Similar to cycle 40r1 above New Zealand, the standard deviation of the differences is small in the stratosphere (4 K) and increases in the mesosphere (10 K).

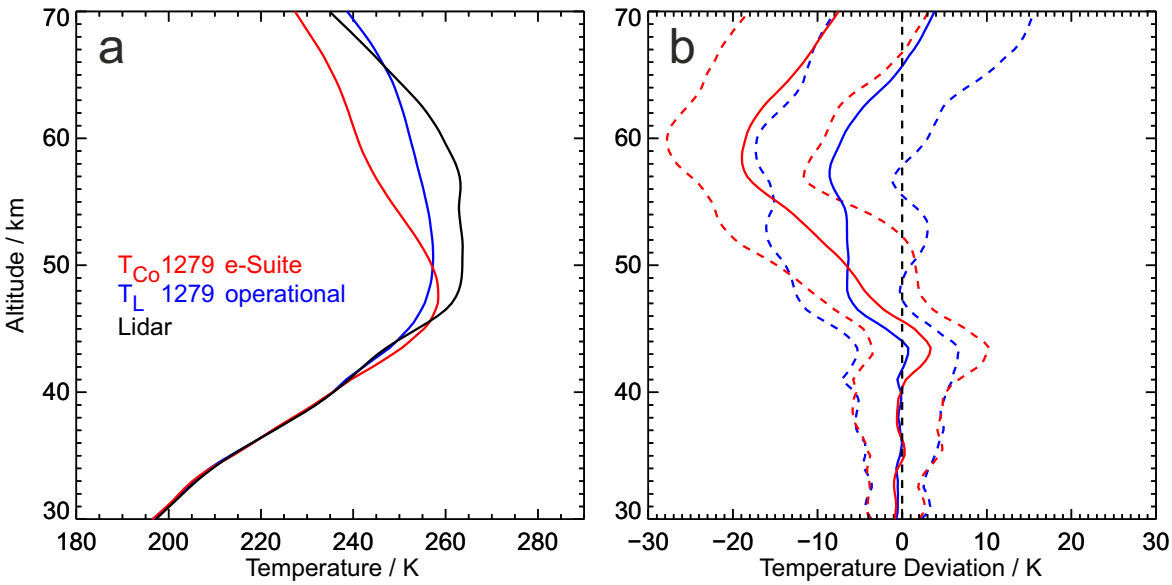

Figure 4.7: Left panel: Mean Temperature profile above Sodankylä during December 2015. Red line: shortterm forecast by the e-Suite 69 ($T_{Co}1279$); Blue line: shortterm forecast by the operational cycle 41r1 (T_L1279). Black line: measurements by the CORAL lidar. Right panel: Temperature deviation (solid lines) and corresponding standard deviations (dashed lines) of the CORAL measurements from the e-Suite 69 (red line) and the operational cycle 41r1 (blue line). Only ECMWF IFS profiles with simultaneous lidar measurements were used.

Comparing the mean E_p profile of the two ECMWF IFS versions to the CORAL measurements (Fig. 4.8a), a similar increase of E_p with increasing altitude between 30 and 40 km altitude can be seen in all three data sets. However, both ECMWF IFS data sets simulate an E_p which is a factor of 2 larger than the E_p derived from CORAL measurements. Above 40 km altitude both ECMWF IFS data sets show strongly decreasing E_p values, with the operational ECMWF IFS cycle showing an even stronger decrease than the e-Suite 69.

Similar to the cycle 40r1 above Lauder (Fig. 4.3b), the e-Suite 69 is capable of reproducing the temporal development of the mean E_p between 30 and 40 km altitude (red line, Fig. 4.8b). In particular the period with enhanced E_p during December 2015 is captured very well by the e-Suite 69, as well as the strong decrease of E_p during January 2016. Additionally, individual events such as the sudden increase of E_p on 15 February 2016 are captured by the e-Suite 69. The mean E_p above Sodankylä simulated by the operational ECMWF IFS cycle 41r1 (blue line, Fig. 4.8b) is rather similar to the e-Suite 69. In particular during December and early January, the differences are almost negligible. Only in the second half of January and the beginning of March does the

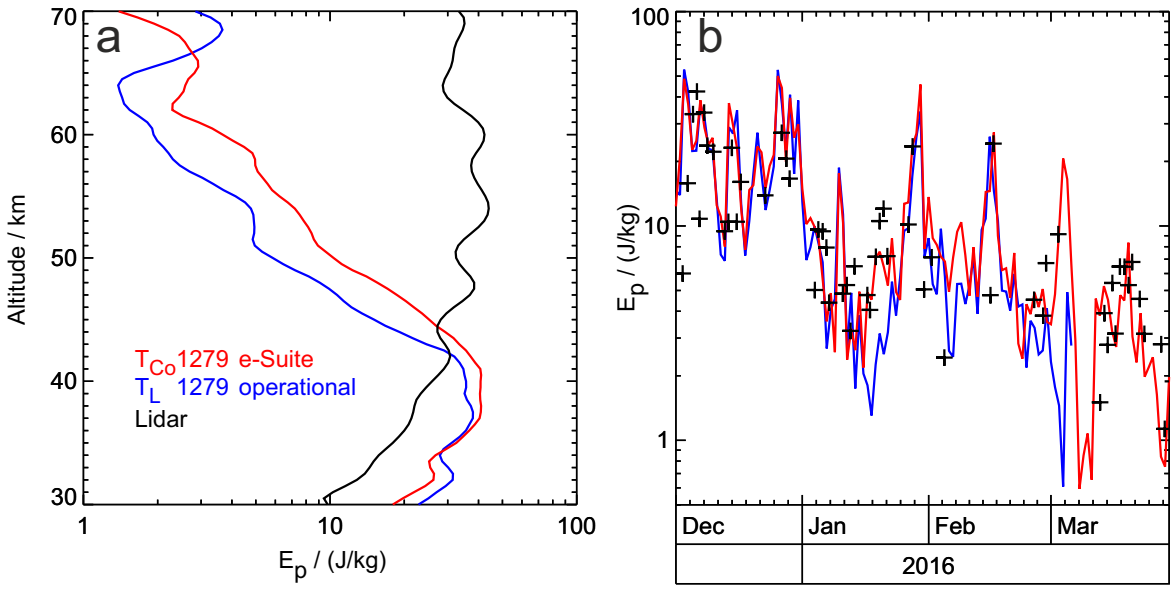

Figure 4.8: Left panel: Mean gravity wave potential energy density E_p above Sodankylä, Finland, during December 2015 derived from CORAL measurements (black), the operational ECMWF IFS cycle 41r1 (blue) and the e-Suite 69 (red). Only ECMWF IFS profiles with simultaneous lidar measurements were used. Right panel: Daily mean E_p between 30 and 40 km altitude over Sodankylä derived from CORAL measurements (black crosses), operational ECMWF IFS cycle 41r1 simulations (T_L1279, blue line) and e-Suite 69 simulations (T_{Co}1279, red line). Here all ECMWF IFS profiles above Sodankylä from December 2015 to March 2016 were used.

operational ECMWF IFS cycle 41r1 simulate considerably lower E_p values between 30 and 40 km altitude, compared to the e-Suite 69. Furthermore, the e-Suite 69 shows a better agreement with the lidar observations during these periods, than the operational ECMWF IFS cycle 41r1.

The here demonstrated capability of resolving lower stratospheric gravity wave activity by the ECMWF IFS e-Suite 69 is in line with the findings of *Dörnbrack et al.* (2016). Using space-borne lidar data (their Figure 1), *Dörnbrack et al.* (2016) showed that the e-Suite 69 resolves orographic gravity waves in the lower stratosphere, which resulted in polar stratospheric cloud formation above Svalbard.

4.4.2 Sensitivity experiments with the ECMWF IFS

At this point the question remains, as to why the e-Suite 69 with the increased horizontal resolution shows significantly colder temperatures within the mesosphere compared

to the operational cycle 41r1. Since several factors have been changed within the ECMWF IFS during the resolution upgrade[4] to $T_{Co}1279$ the source of this additional cold bias remains unknown. Of particular importance is the initial state, i.e. the analysis from which the specific simulations are run. Since the operational cycle 41r1 and the e-Suite 69 both are initialized with different analyses, testruns were carried out in order to investigate the influence of the horizontal grid versus the influence of the different analyses.

For the testruns the week from 10 to 17 December 2014 was chosen, since lidar coverage is best during this week. The testruns have been carried out with the operational cycle 42r1, because the processors at ECMWF were recently upgraded and only cycle 42r1 was ported onto the new processors. To maximize the influence of the dynamical core of the ECMWF IFS, the simulations were conducted with 5 lead days[5]. Like for the previous comparison, the ECMWF IFS data was interpolated to the position of the lidar and only ECMWF IFS profiles with coinciding lidar measurements were used in the comparison. A total of four testruns were carried out with different combinations of the horizontal grid ($T_{Co}1279/T_L1279$) and the two available analyses (e-Suite 69/operational analysis). The notation of the testruns is "$T_{L/Co}1279$ An 01/69", where An 01/69 denotes the operational/e-Suite analysis.

The mean temperature profiles of the four testruns in comparison to the CORAL measurements and the operational ECMWF IFS cycle 41r1 and the e-Suite 69 (the latter two were sampled with 5 lead days as well) are shown in Figure 4.9. The first thing which comes to eye is that all ECMWF IFS simulations, regardless of their grid and analysis, exhibit significantly lower temperatures compared to the lidar measurements above 50 km altitude. Below 45 km altitude, all simulations agree well with the CORAL measurements. The testruns (solid lines), the operational ECMWF IFS and the e-Suite 69 (dashed lines) all exhibit a similar temperature gradient within the middle atmosphere. The only difference is an almost constant temperature offset of 6 K to 8 K above 50 km altitude.

Furthermore, the e-Suite 69 (red dashed line) and the $T_{Co}1279$ An 69 testrun (orange line) yield almost identical mean temperature profiles. This is not astonishing since both simulations are run on the same grid, initialized from the same analysis. The only difference is that the $T_{Co}1279$ An 69 testrun was carried out with cycle 42r1 instead of 41r2, due to the porting of cycle 42r1 onto the recently upgraded processors at ECMWF. The remaining differences between both ECMWF IFS simulations are therefore assumed to be caused by slightly different numerics. In contrast, the T_L1279 An 01 testrun (dark green line) exhibits a mean temperature which is 2 K to 3 K

[4] for a detailed list of changes please see https://software.ecmwf.int/wiki/display/FCST/Detailed+information+of+implementation+of+IFS+cycle+41r2

[5] Hourly outputs after 97 h to 108 h of simulations initialized from the respective 00 UTC or 12 UTC analysis were combined to form a continuous hourly data set.

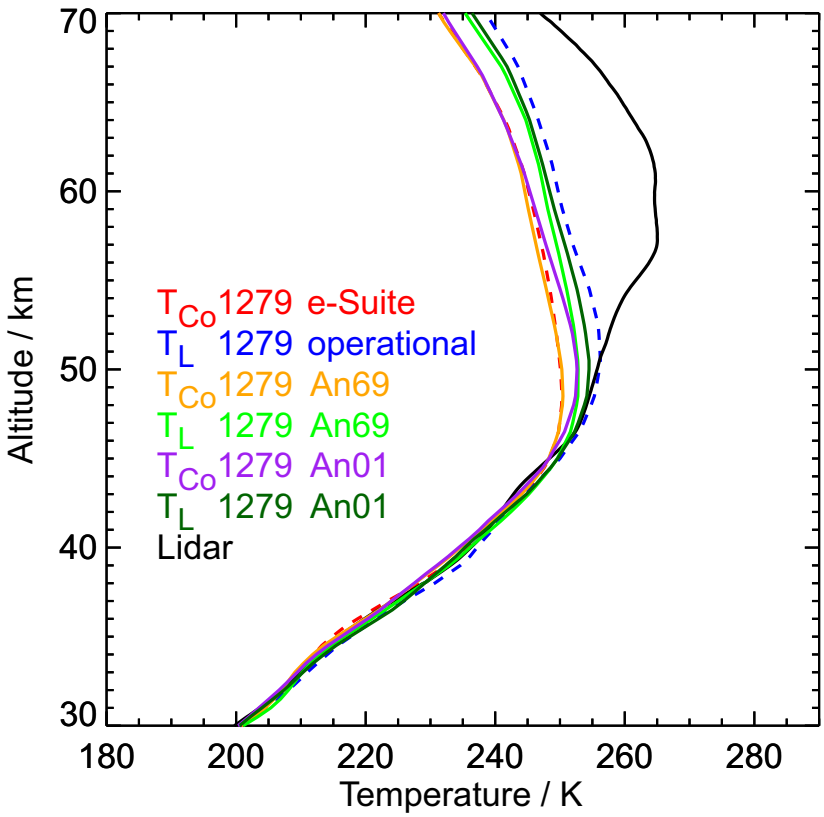

Figure 4.9: Mean Temperature profiles above Sodankylä from 10 to 17 December 2015. Black line: CORAL measurements; red/blue dashed line: e-Suite 69/operational ECMWF IFS cycle 41r1 with 5 lead days; Colored solid lines: ECMWF IFS testruns with 5 lead days. Only ECMWF IFS profiles with simultaneous lidar measurements were used.

lower than the mean temperature of the operational ECMWF IFS cycle 41r1 (blue dashed line), although both simulations run on the same grid and are initialized with the same analysis. A likely cause for the cooling is a slight reduction of the mean ozone concentration within the middle atmosphere in cycle 42r1 compared to 41r1 (S. Malardel, personal communication). This reduction of ozone concentration is expected to result in slightly lower middle atmospheric temperatures due to less absorption of solar ultraviolet radiation by ozone.

The T_L1279 An 69 testrun (light green line) simulates even lower temperatures than the T_L1279 An 01 testrun (dark green line). This indicates that even after 97 h to 108 h of simulation an influence of the initializing analysis remains. The lower temperatures simulated by the T_{Co}1279 An 01 testrun (purple line) compared to the T_L1279 An 01 testrun (dark green line) are contrary to the expected effect of an increased horizontal

resolution. As said previously, a higher horizontal resolution is expected to yield a more realistic representation of gravity waves, which ultimately should yield more wave drag within the middle atmosphere and thus higher temperatures. This seems not to be the case in the $T_{Co}1279$ An 01 testrun. A possible cause for the additional cooling within the middle atmosphere is the reduced horizontal diffusion associated with the $T_{Co}1279$ grid. This is in line with previous tests with varying horizontal diffusion within the ECMWF IFS, which showed a tendency towards lower temperatures when the horizontal diffusion was reduced (S. Malardel, personal communication).

4.5 Summary

Summarizing the previous results, it was shown that the thermal state of the ECMWF IFS cycle 40r1 with a resolution of T_L1279 agrees reasonably well with lidar measurements above New Zealand up to 60 km altitude during wintertime. At higher altitudes, the ECMWF IFS exhibits temperatures which are on average too low. Gravity waves are well resolved by the ECMWF IFS cycle 40r1 up to 45 km altitude (approximately 1 hPa). At higher altitudes the "hard sponge layer" of the ECMWF IFS sets in and strongly dampens gravity waves. Furthermore, it was shown that the ECMWF IFS is capable of reproducing the overall temporal evolution of the gravity wave activity between 30 and 40 km altitude. The capability of resolving individual wave events was demonstrated for the case of 1 August 2014, where the phase of the gravity waves simulated by the ECMWF IFS matched the phase of the waves observed by TELMA almost perfectly up to 50 km altitude. Additionally, it was shown that when the vertical resolution of the lidar is degraded to 2900 m even the amplitudes of the ECMWF IFS and the TELMA measurements are in agreement on 1 August 2014. Additionally, there is a number of cases where the gravity waves simulated by the ECMWF IFS disagree with the lidar observations. An investigation, under which circumstances the ECMWF IFS is capable of simulating the correct gravity waves, was inconclusive.

It was assumed that the recent horizontal resolution upgrade from 16 km to 9 km of the ECMWF IFS would result in a more realistic representation of the middle atmosphere due to a better representation of gravity waves. However, this is not the case. Instead, it was shown that the higher resolution ECMWF IFS exhibits an even stronger cold bias within the middle atmosphere compared to the previous ECMWF IFS cycle, despite the high-resolution ECMWF IFS simulating a slightly larger gravity wave activity within the stratosphere.

Testruns conducted with the ECMWF IFS suggest that several factors contribute to the enhanced mesospheric cold bias of the high-resolution ECMWF IFS: The changed analysis cycle, a change of the mean ozone profile, a reduced horizontal diffusion within the middle atmosphere. Additionally the gravity waves which are explicitly resolved

by the high-resolution version of the ECMWF IFS cannot even reach the mesosphere, since they are filtered out by the sponge layer already at 45 km altitude.

Thus, the ECMWF IFS can be regarded as a very valuable tool when it comes to gravity wave studies up to 45 km altitude. However, at higher altitudes the ECMWF IFS data should be treated with care since the data is influence by the damping formalism of the sponge layer. As a consequence, if higher altitudes are to be studied with the help of model data, a different model than the ECMWF IFS should be used. Possible alternatives might be the NAVGEM reanalysis product (e.g. *Eckermann et al.*, 2016), or the upper atmosphere version of the ICON model (UA-ICON) which is currently developed by the German Weather Service (DWD).

The ECMWF IFS is in particular useful for gravity wave studies when co-located observations of gravity wave parameters e.g. phase and amplitude are available and the skill of the model during the particular case can be evaluated. The model data can then be used to estimate e.g. the propagation direction of gravity waves (at least in the altitude range where the mean state is well reproduced by the model, i.e. below 60 km or 45 km at mid- or high-latitudes, respectively), which cannot be determined from lidar temperature observations alone. Moreover, the model data can be used to extend the lidar temperature profiles to lower altitudes, where the lidar data is not available (cf. *Ehard et al.*, 2016).

5 Horizontal propagation of large-amplitude mountain waves into the polar night jet

The results presented in this chapter have been published by Ehard et al. (2017).

To evaluate whether horizontal propagation of mountain waves can contribute to the missing gravity wave drag at 60° S, TELMA measurements are analyzed, which were taken during the DEEPWAVE campaign (The Deep Propagating Gravity Wave Experiment, *Fritts et al.*, 2016) in New Zealand during austral winter 2014. During DEEPWAVE, a combination of ground-based, airborne, in-situ and satellite measurements was utilized to study the propagation of gravity waves from the troposphere into the middle atmosphere. New Zealand was chosen because it is a hotspot region for gravity waves in wintertime (e.g. *Jiang et al.*, 2005; *Gong et al.*, 2012; *Hoffmann et al.*, 2016). In the southern hemispheric winter, the upper branch of the polar night jet usually extends over New Zealand at altitudes above 30 km to 40 km. This results in stratospheric westerlies, which provide favorable conditions for the propagation of mountain waves deep into the middle atmosphere (*Fritts et al.*, 2016). Furthermore, there is generally a large vertical shear of the horizontal wind above New Zealand. Additionally, the zonal wind in the lower and middle stratosphere increases polewards towards the core of the polar night jet, resulting in a strong meridional shear of the zonal wind.

Dunkerton (1984) stated that such a meridional shear of the zonal wind causes mountain waves to be refracted and subsequently propagate towards the region of increased zonal wind speeds (c.f. Fig. 3 by *Dunkerton*, 1984). Because the refraction and subsequent propagation acts on mountain waves originating to the north and south of the region with increased zonal wind speeds, the mountain waves are focused into this region (cf. *Sato et al.*, 2012, Fig. 5). Following *Dunkerton* (1984), several studies investigated this wave focusing: Utilizing satellite measurements and raytracing calculations over the southern Andes, *Preusse et al.* (2002) illustrated the importance of the wavevector modification for the focusing of orographic waves. By utilizing global satellite observations and raytracing calculations, *Preusse et al.* (2009) found peak values of 15° for the meridional propagation of gravity waves. *Sato et al.* (2009) and *Sato et al.* (2012) demonstrated the refraction of orographic gravity waves simulated by a gravity wave resolving general

circulation model. Moreover, *Sato et al.* (2012) stated that the wave energy from orographic waves can thereby be advected over large horizontal distances. With the combination of mesoscale simulations and raytracing calculations, *Jiang et al.* (2013) identified orographic gravity waves over the southern Andes, which were refracted and propagated zonally downstream over a distance of more than 1000 km. Very recently, *Plougonven et al.* (2017) showed evidence for the occurrence of horizontally propagating non-orographic gravity waves in the lower stratosphere above the Southern Ocean.

This thesis investigates the horizontal propagation of mountain waves over New Zealand on 31 July and 1 August 2014. The date around 1 August 2014 was chosen because of the remarkable agreement between the TELMA measurements and the ECMWF IFS (cf. Fig. 4.5). The TELMA measurements are used to investigate the temporal and vertical evolution of the wave event, while ECMWF IFS data is used to characterize the ambient conditions in the troposphere and lower stratosphere. Raytracing simulations are conducted in order to examine the propagational pathways of the mountain waves. The results are compared to satellite measurements and ECMWF IFS data.

5.1 Meteorological conditions

The synoptic situation during the period between 31 July and 1 August 2014 is characterized by a high pressure system northeast of New Zealand and two consecutive low pressure systems passing the South Island to the southwest (not shown). The nearly stationary pressure difference caused a northwesterly flow at 700 hPa with wind speeds exceeding $30\,\mathrm{m\,s^{-1}}$ above the Southern Alps of New Zealand, resulting in favorable conditions for the excitation of mountain waves (Fig. 5.1a).

At 300 hPa the flow was dominated by a broad tropospheric jet stream with two cores of horizontal winds larger than $70\,\mathrm{m\,s^{-1}}$ to the southwest of the South Island (Fig. 5.1b). The winds at 300 hPa were aligned nearly perpendicular to the main mountain ridges – like the wind at 700 hPa – resulting in minimal directional wind shear throughout the troposphere. During the considered time period, the movement of the low pressure systems shifted the tropospheric jet stream to the northeast, resulting in increasing wind speeds above the South Island.

The altitude of the dynamical tropopause (2 PVU surface, Fig. 5.2), reached large values of up to 17 km towards the northeast of New Zealand. Values as low as 6 km to the southwest cause a strongly tilted tropopause with a tropopause height of about 11 km around Lauder. The resulting sharp separation of polar and subtropical air masses further intensified the horizontal winds above the South Island of New Zealand. As seen in Figure 5.2, the extremely broad jet across New Zealand extends across the strongly tilted dynamical tropopause. This broad jet results from the combination of the polar front jet to the south-west and the subtropical jet stream to the north-east.

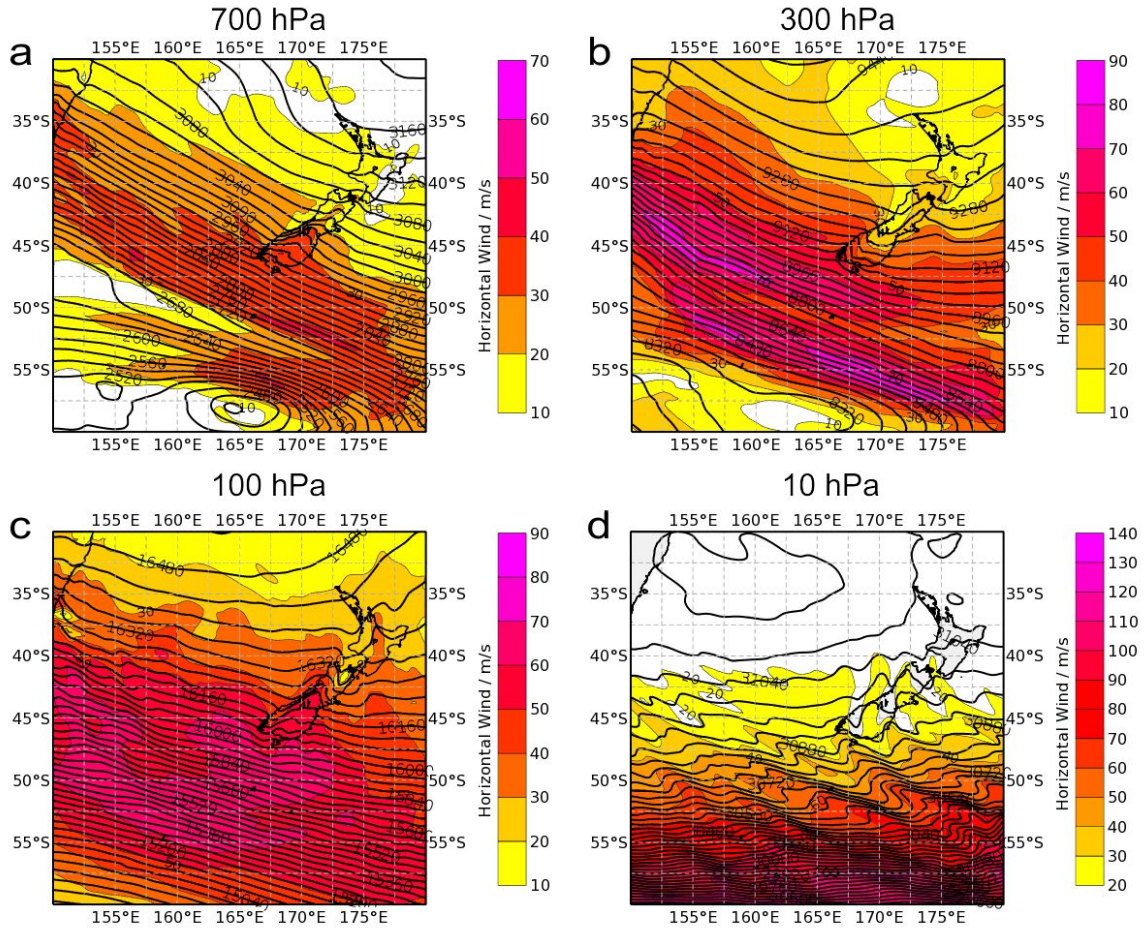

Figure 5.1: Geopotential height (m, solid lines) and horizontal wind speed ($\mathrm{m\,s^{-1}}$, color coded) at 700, 300, 100 and 10 hPa on 31 July 2014 at 1200 UTC. Data is taken from the ECMWF IFS cycle 40r1 ($\mathrm{T_L}1279$).

At 100 hPa the jet stream was still present above the Southern Pacific Ocean (Fig. 5.1c), although the 100 hPa level – corresponding to ≈ 16 km in altitude – is higher than the dynamical tropopause within this region (cf. Fig. 5.2). This branch of the tropopause jet belongs to the subtropical jet which diverted south during this event. The resulting westerly winds above the Southern Island at 100 hPa reached up to $40\,\mathrm{m\,s^{-1}}$ to $60\,\mathrm{m\,s^{-1}}$ on 31 July and 1 August.

In the middle stratosphere the dominant flow pattern was the polar night jet with zonal winds exceeding $120\,\mathrm{m\,s^{-1}}$ south of 55° S (Fig. 5.1d). Towards the north, a remarkably strong meridional gradient reduces the magnitude of the horizontal wind to values close to zero over the Tasman Sea. During the entire period, the horizontal winds at 10 hPa were rather small and on the order of $20\,\mathrm{m\,s^{-1}}$ above the South Island of New

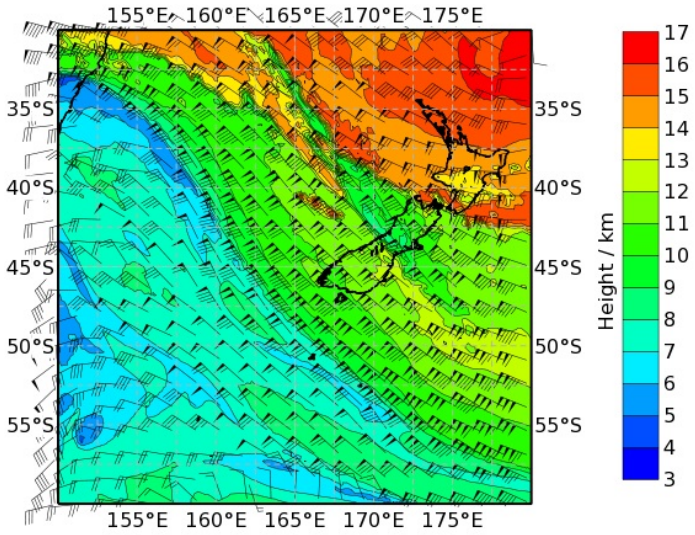

Figure 5.2: Height of the dynamical tropopause (2 PVU surface, km, color coded) and horizontal wind speed ($\mathrm{m\,s^{-1}}$, barbs) on 1 August 2014 at 1200 UTC. Data is taken from the ECMWF IFS cycle 40r1 ($\mathrm{T_L}1279$).

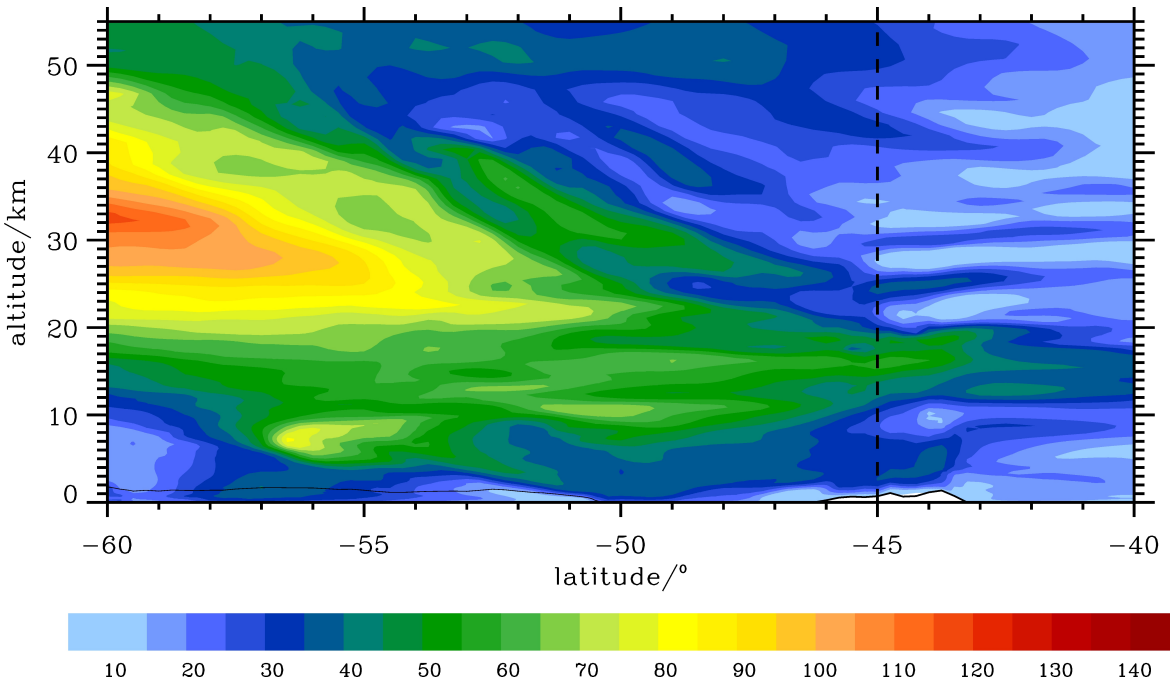

Figure 5.3: Horizontal wind speed ($\mathrm{m\,s^{-1}}$, color coded) along 170° E on 31 July 2014 at 1200 UTC. The black dashed vertical line marks the position of Lauder, New Zealand. Data is taken from the ECMWF IFS cycle 40r1 ($\mathrm{T_L}1279$).

Zealand.

A meridional cross section of the horizontal wind along 170° E is shown in Figure 5.3. Large winds exist throughout the troposphere ($> 20\,\mathrm{m\,s^{-1}}$) and in the lowermost stratosphere ($> 50\,\mathrm{m\,s^{-1}}$), extending from New Zealand towards the South. Horizontal winds above the South Island are reduced above 20 km altitude and a strong meridional gradient of the horizontal wind is induced by the presence of the polar night jet at 60° S. It should be noted that planetary wave activity in this late stage of austral winter displaced the polar vortex to the south, causing the particular meridional distribution of the horizontal wind.

5.2 Results

5.2.1 Lidar measurements

In the time frame 31 July to 1 August 2014, lidar temperature observations with TELMA exhibit a stable and vertically broad stratopause which is located between 40 and 50 km altitude (Fig. 5.4a, b). The stratopause temperature during this period is approximately 250 K.

The gravity wave induced temperature perturbations on 31 July 2014 exhibit phase lines which are almost constant in altitude in the stratosphere (Fig. 5.4c). This pattern is indicative of stationary mountain waves (e.g *Kaifler et al.*, 2015b). The vertical wavelength of these mountain waves is $\lambda_z \approx 4$ km. Maximum amplitudes are detected at 30 km altitude and below. Above this altitude, a structure of larger vertical extent, lower amplitudes and a slightly descending phase line is detected within the stratopause region (40 km to 50 km altitude). The mean E_p profile on 31 July (blue line, Fig. 5.5) exhibits values of $60\,\mathrm{J\,kg^{-1}}$ at 25 km altitude which decrease to $12\,\mathrm{J\,kg^{-1}}$ at 40 km altitude. At roughly 50 km altitude, a region of enhanced E_p is detected, which is related to the wave structure with a descending phase line in the stratopause region.

On 1 August 2014, a stationary, coherent phase line with maximum temperature perturbation amplitudes is observed near 30 km altitude between around 1300 to 1500 UTC (Fig. 5.4d). At the same time, the stationary patterns are disrupted between 35 and 45 km resulting in a more chaotic pattern and reduced temperature perturbations amplitudes. Afterwards, at around 1500 UTC, the temperature perturbation amplitudes at 30 km become attenuated, but stationary phase lines with enhanced temperature perturbation amplitudes form between 35 and 45 km altitude. Above 45 km altitude, temperature perturbation amplitudes are much smaller and the perturbation patterns appear to be less regular. The mean E_p profile on 1 August (black line, Fig. 5.5) shows the largest stratospheric gravity wave activity with values of up to $60\,\mathrm{J\,kg^{-1}}$ between

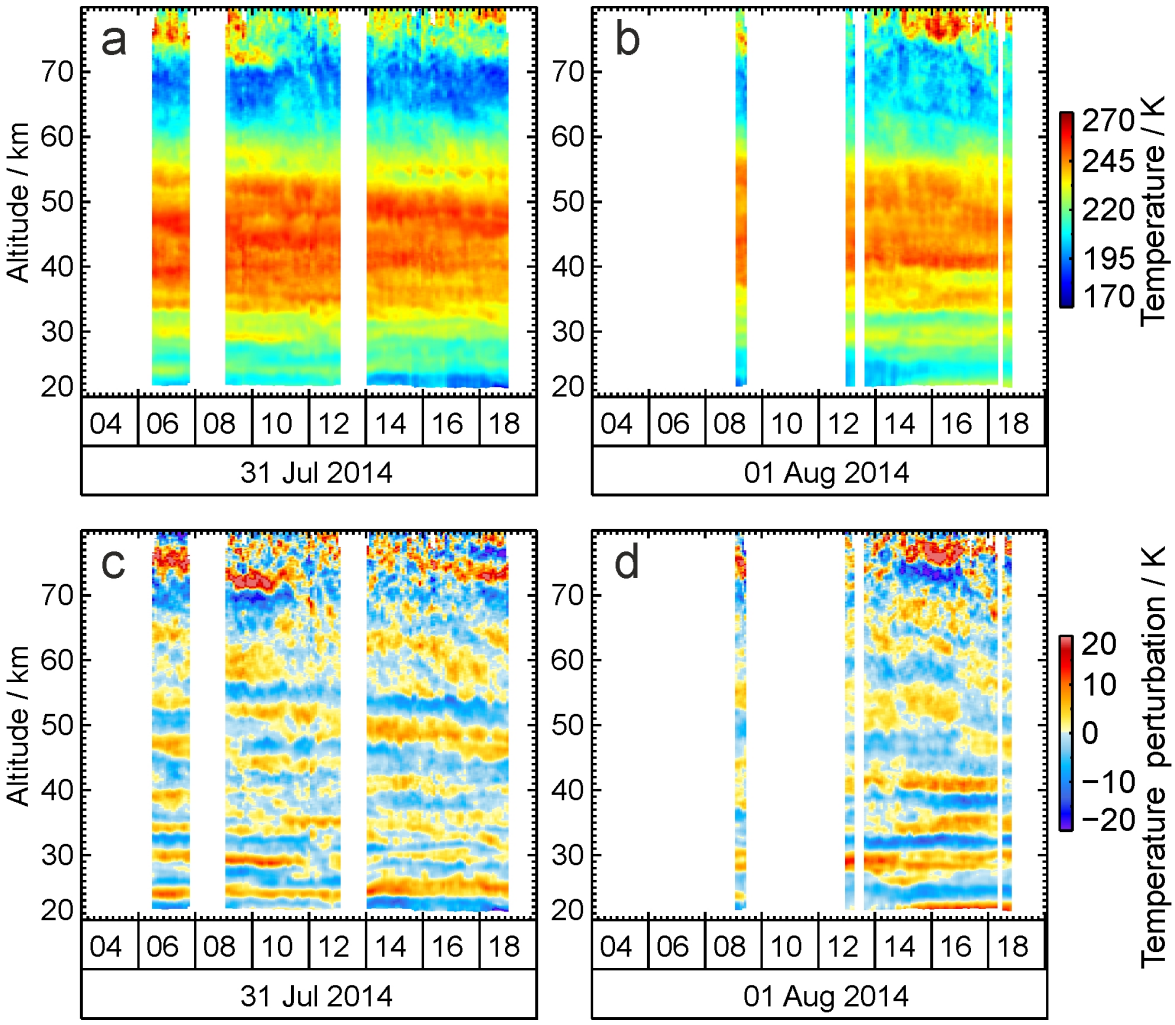

Figure 5.4: Temperatures observed by the TELMA system above Lauder on 31 July and 1 August 2014 (a, b) and the calculated temperature perturbations (c, d).

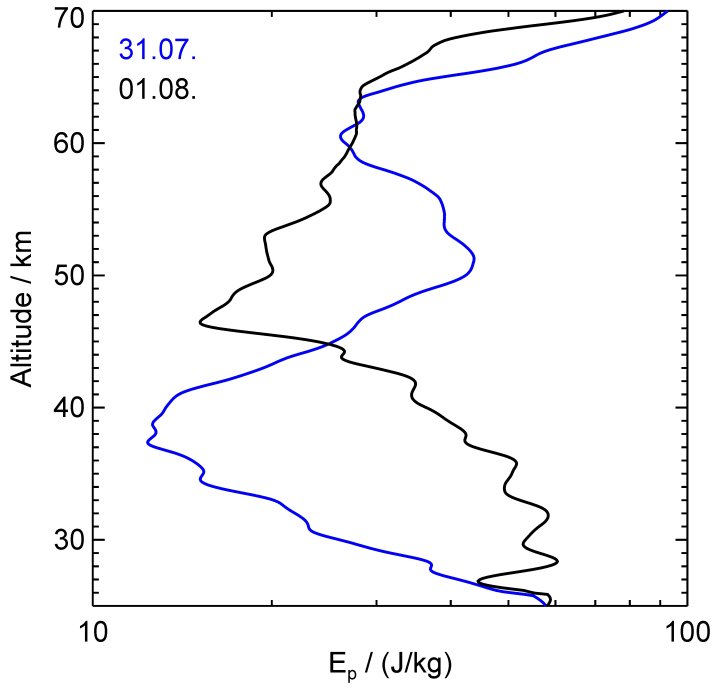

Figure 5.5: Mean E_p per mass profiles observed by the TELMA system above Lauder on 31 July (blue) and 1 August 2014 (black).

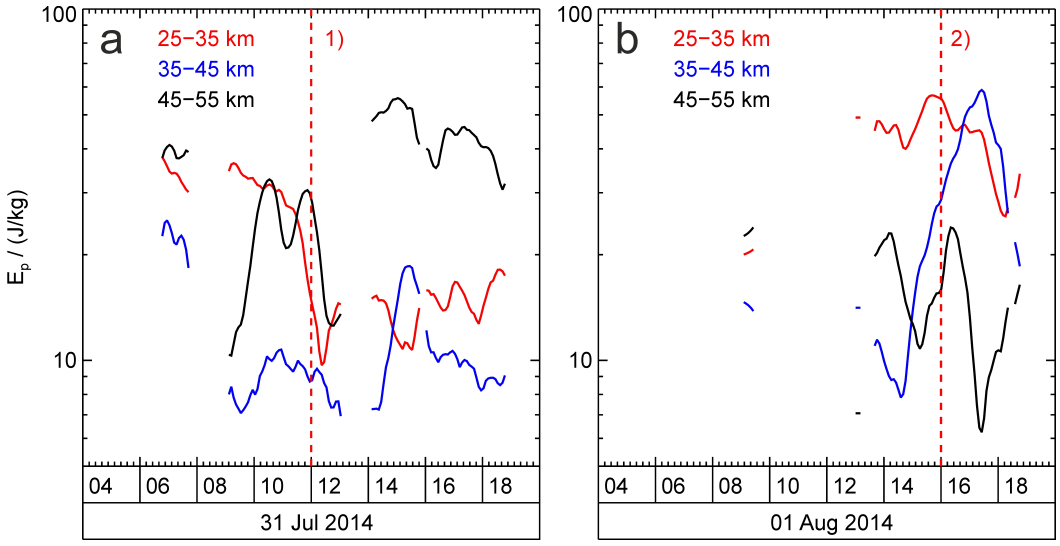

Figure 5.6: E_p per mass as a function of time, averaged over different altitude intervals (color coded) on 31 July (a) and 1 August 2014 (b). The red dashed lines mark the onset of episodes 1 and 2 (see text for details). The data was smoothed by a running mean with a window width of 1 h.

25 and 33 km altitude. Above 33 km altitude E_p decreases and reaches a minimum of 14 J kg^{-1} at 46 km altitude. In the mesosphere, E_p increases gradually with increasing altitude.

The temporal evolution of the gravity wave activity during both days is visible in the evolution of the mean E_p within certain altitude ranges (Fig. 5.6). To simplify the description in the following and to guide the eye in Figure 5.6, two distinct episodes are marked (red dashed lines). Episode 1) marks a sudden decrease of E_p in the altitude range 25 km to 35 km around 1200 UTC on 31 July. Before episode 1), E_p values of 30 J kg^{-1} are observed between 25 and 35 km altitude. Around 1200 UTC on 31 July, E_p values decrease by a factor of 2. In contrast, at 35 km to 45 km E_p values remain at $\approx$ 10 J kg^{-1} throughout the observed period. Elevated E_p values as large as 40 J kg^{-1} at 45 km to 55 km altitude are associated with the wave structure characterized by descending phase lines in the stratopause region.

On 1 August, the mean E_p at 25 km to 35 km altitude remains approximately constant (40 J kg^{-1}) throughout the observational period, while E_p at 35 km to 45 km increases by a factor of 8 around 1600 UTC – the onset of episode 2). Maximum values of 60 J kg^{-1} are observed around 1700 UTC. Above, at 45 km to 55 km altitude, E_p values are significantly lower (10 J kg^{-1} to 20 J kg^{-1}).

5.2.2 ECMWF data

Maps of horizontal divergence derived from the ECMWF IFS at different pressure levels on 31 July 2014 at 1200 UTC are displayed in Figure 5.7. The divergence patterns at other times during the event are very similar and are therefore not shown. Alternating bands of positive and negative horizontal divergence are a suitable indicator for the presence and orientation of gravity waves in model data (e.g. *Plougonven and Teitelbaum*, 2003; *Alexander and Teitelbaum*, 2007).

At 100 hPa, the gravity wave phase lines above the South Island are oriented mostly parallel to the mountain range (Fig. 5.7a). These bands are a typical signature of stationary mountain waves, as their orientation is persistent throughout the entire troposphere up to 100 hPa. With increasing altitude, the phase lines of the mountain waves change towards a north-south orientation above the South Island (Fig. 5.7b,c). At 30 hPa and above, these phase lines extend leeward of the South Island, forming the trailing waves over the Ocean. These leeward extending phase lines are oriented nearly perpendicular to the South Island.

An additional wave packet is simulated over the ocean west and southwest and thus upstream of New Zealand. These upstream waves exhibit phase lines with an orientation similar to the trailing waves above New Zealand. At 100 hPa the upstream waves remain close to Tasmania and the southeast of Australia. With increasing altitude

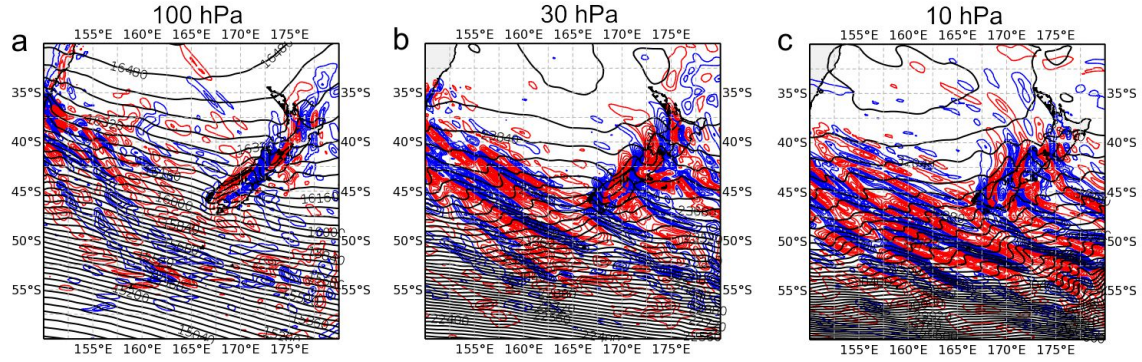

Figure 5.7: Geopotential height (m, black solid lines) and horizontal divergence (pos. values - red, neg. values - blue, increments of $4 \times 10^{-5}\,\mathrm{s}^{-1}$) at 100, 30 and 10 hPa on 31 July 2014 at 1200 UTC. Data is taken from the ECMWF IFS cycle 40r1 ($\mathrm{T_L}1279$).

this wave packet extends towards the southernmost tip of New Zealand. South of New Zealand, when approaching the polar night jet, the upstream waves merge with the trailing waves and individual contributions become indistinguishable.

The temporal and spatial evolution of the wave event is depicted by the Hovmöller diagrams in Figure 5.8. With the temporally increasing horizontal wind above the South Island of New Zealand (Fig. 5.8a), the gravity wave activity as measured by the magnitude of the horizontal divergence increases above New Zealand (Fig. 5.8b). It remains constantly over the South Island indicating the presence of stationary mountain waves, which are detectable up to about 5 hPa ($\approx$ 35 km altitude, Fig. 5.8c). To the east of the South Island, banded divergence patterns represent the downstream impact of the mountain waves. Upstream of New Zealand, another localized source of mountain waves exists over Tasmania where the wave activity starts two days earlier due to the earlier appearance of the jet stream (Fig. 5.8c). Although the gravity waves originating from Tasmania show a zonal downstream propagation, they do not extend over New Zealand in the stratosphere (Fig. 5.8b,c). However, south of New Zealand, within the latitude belt from 45° S to 55° S (Fig. 5.8e,f), stratospheric gravity waves from the two source regions merge and can no longer be distinguished.

Figure 5.9a shows profiles of the horizontal wind from the ECMWF IFS above Lauder as a function of time. Again, the onset of episodes 1) and 2) is marked. In the stratosphere, stacked bands of higher and lower horizontal wind speeds indicate the presence of mountain waves in a similar manner as the temperature perturbations derived from the lidar observations (cf. Fig. 5.4c, d). The pattern is most prominent at 20 km to 30 km altitude between 31 July 1200 UTC and 1 August 1800 UTC. This time frame coincides with the appearance of the elevated subtropical jet stream, which manifests as large horizontal wind speeds at 15 km to 20 km altitude.

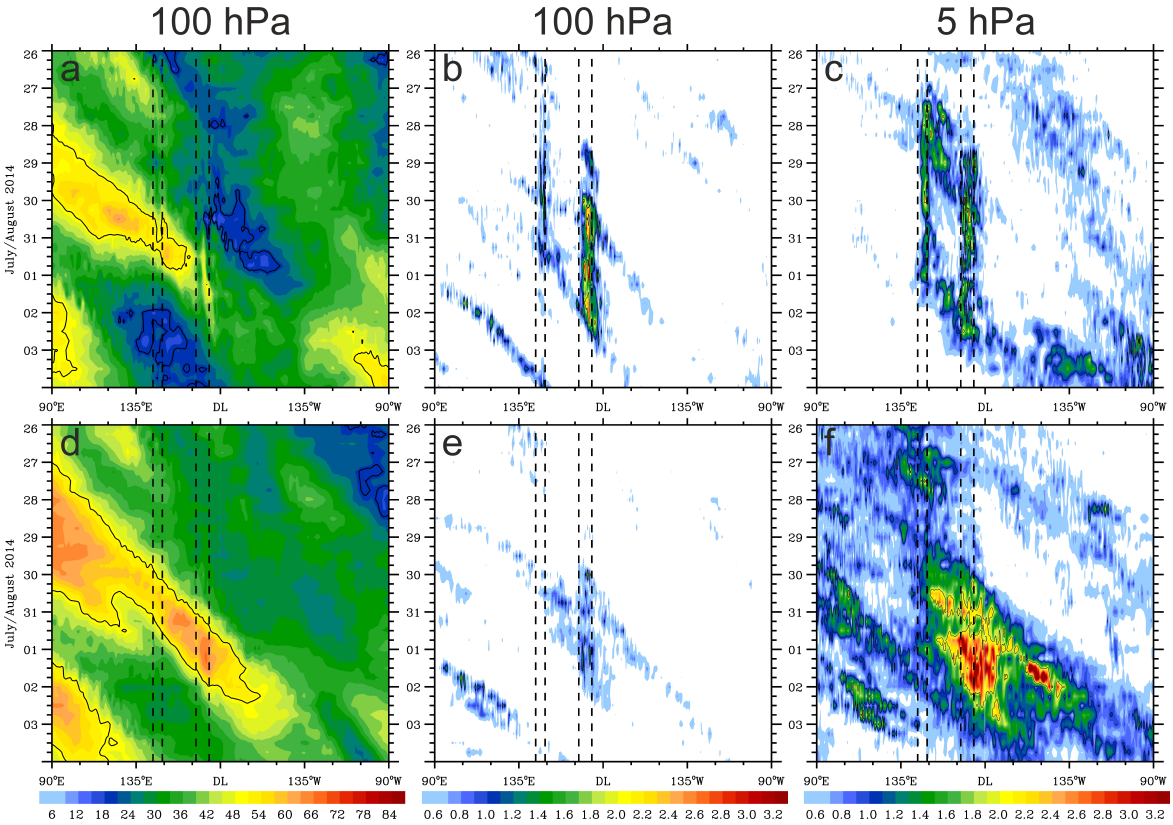

Figure 5.8: Hovmöller diagrams of horizontal wind speed at 100 hPa (left column; $\mathrm{m\,s^{-1}}$, color coded) and absolute horizontal divergence ($10^{-4}\,\mathrm{s^{-1}}$, color coded) at 100 hPa (middle column) and 5 hPa (right column). Upper row: averaged between 40° and 45° S; lower row: averaged between 45° and 55° S. The black dashed lines depict the zonal extent of Tasmania and the South Island of New Zealand. Data is taken from the ECMWF IFS cycle 40r1 ($\mathrm{T_L}1279$).

it applies better to Boussinseq waves.

Large values of $|u'/\overline{u}|$ occur at 20 km to 35 km altitude during episode 1) (31 July 1200 UTC to 1 August 1600 UTC), whereby the largest values are observed on 1 August until 1200 UTC. This time coincides with the occurrence of the banded patterns of reduced horizontal wind speeds (Fig. 5.9a). At the onset of episode 2), $|u'/\overline{u}|$ suddenly decreases in the entire stratosphere. After 1900 UTC a thin layer of enhanced $|u'/\overline{u}|$ values appears at 35 km altitude.

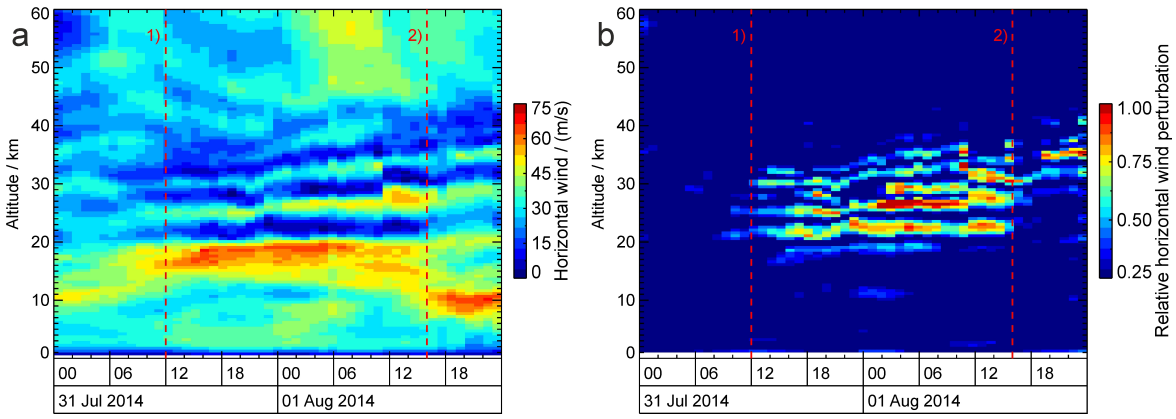

Figure 5.9: Horizontal wind speed above Lauder (a) and relative horizontal wind perturbation $|u'/\overline{u}|$ (b). The red dashed lines mark the onset of episode 1 and 2 (see text for details). Data is taken from the ECMWF IFS cycle 40r1 (T_L1279).

5.2.3 AIRS

The Atmospheric Infrared Sounder (AIRS) on the Aqua satellite is a nadir-pointing infrared spectrometer, measuring in different wavelength bands ranging from 3.74 to 15.4 µm (*Aumann et al.*, 2003). AIRS conducts cross-track scans perpendicular to the flight track with a horizontal scan width of 1600 km and a footprint size of 13 km at nadir.

In this thesis, Level-1 B radiance measurements by the 15.4 µm channels are used, from which brightness temperatures are calculated. The 15.4 µm channels were chosen due to the narrower kernel functions compared to the 4.3 µm channels (Fig. 3 *Hoffmann and Alexander*, 2009). To extract gravity wave perturbations, the brightness temperatures of each scan are smoothed over 33 points along track. A sixth order polynomial across track was fitted to the smoothed brightness temperatures to account for systematic trends, such as limb brightening. Smoothing the result again over 5 (3) points across (along) track and subtracting the result from the raw brightness temperatures yields the gravity wave perturbations[1] with $\lambda_h \leq 500$ km. Due to the combination of the smoothing parameters and the vertical weighting functions of the 15 μm channels, one can observe horizontal and vertical wavelengths of $\lambda_h > 40$ km and $\lambda_z > 12$ km (*Gong et al.*, 2012, cf. Table A1). Since the lidar on the other hand can only observe gravity waves with $\lambda_z < 15$ km, due to the chosen filtering method (cf. Chapter 3), TELMA and AIRS are somewhat complementary in their capabilities of observing the gravity wave spectrum.

[1]The gravity wave perturbations derived from the AIRS data were kindly provided by S. Eckermann

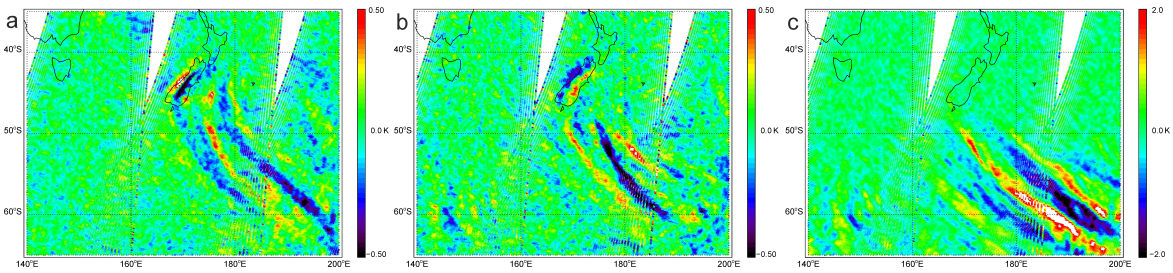

Figure 5.10: Gravity wave perturbations deduced from AIRS Level-1 B radiance measurements on descending orbits at 100 hPa (a), 40 hPa (b) and 3 hPa (c) on 1 August 2014. Note the different color scale in panel (c). AIRS crossed 50° S on 1 August 2014 around 1140, 1320 and 1500 UTC (from east to west). Courtesy of M. Bramberger.

Figure 5.10 shows gravity wave perturbations determined from AIRS Level-1 B brightness temperature measurements for different pressure levels on 1 August 2014. At 40 and 100 hPa (Fig. 5.10a, b) bands of positive and negative radiance temperature perturbations extend over the South Island of New Zealand. Their shape and orientation is very similar to the horizontal divergence patterns from the ECMWF analyses on 31 July (Fig. 5.7a,b) and 1 August 2014 (not shown). Above the 40 hPa level, the mountain waves above New Zealand – previously identified in the lidar observations and the ECMWF data – are not detected by AIRS. This can be explained by the observational filter of AIRS: The 40 hPa layer is located at $\approx$ 23 km altitude, which is above the subtropical jet stream (cf. Fig. 5.9a). The decreasing horizontal wind speed and the increasing stability in the stratosphere cause a decrease of the vertical wavelength of the mountain waves and thus the mountain waves fall below the visibility limit of AIRS.

At 3 hPa (Fig. 5.10c) AIRS radiance temperature perturbations show large amplitude waves between 50° S and 65° S. These waves extend far to the east, starting from 170° E. Phaselines are thereby oriented along the northwest-southeast axis. The orientation and horizontal extent of these gravity waves is thereby similar to the waves simulated by the ECMWF IFS above 10 hPa on 31 July (Fig. 5.7c) and 1 August 2014 (not shown).

5.2.4 Raytracing simulations

Raytraces are calculated with the GROGRAT model (*Marks and Eckermann*, 1995; *Eckermann and Marks*, 1996) in a background atmosphere which consists of temperature and wind fields from the ECMWF IFS analyses up to an altitude of 50 km. Above 40 km

altitude these fields are gradually relaxed to temperature and geostrophic wind fields[2], which were derived from SABER (Sounding of the Atmosphere using Broadband Emission Radiometry) and Aura/MLS (Microwave Limb Sounder) measurements[3]. Switching from ECMWF IFS data to SABER and MLS data above 50 km altitude is motivated by the findings presented in chapter 4, in particular by the presence of the "hard sponge layer" of the ECMWF IFS above 45 km altitude. The top of the background fields is located at 80 km. The explicit time dependence of the raytraces was neglected, meaning the background atmosphere was assumed to be stationary. The prescribed background atmosphere is interpolated on a grid with 2.5° latitude, 3.75° longitude and 2.5 km vertical resolution as done previously by *Preusse et al.* (2014). Integration of the rays is stopped at 75 km altitude to avoid edge effects at the top of the background fields.

Gravity waves were launched within the GROGRAT model at 2.5 km altitude at several locations above the South Island of New Zealand. At the launch level, the gravity waves had zero ground-based phase speed, a horizontal wavelength $\lambda_h = 250$ km and a wave vector orientated perpendicular to the Southern Alps of New Zealand. The launch parameters were thereby estimated from the ECMWF horizontal divergence fields (cf. Fig. 5.7a). Additionally, it was checked that the vertical wavelength and temperature amplitude calculated by GROGRAT are in agreement with the gravity waves observed by the lidar at 30 km to 40 km altitude. An exemplary result of these simulations is shown in Figure 5.11 for 1 August 2014 at 0000 UTC. Note, that in addition to the ray paths, the wave vector at the start and end point (black and red arrows) is plotted as well. In between, the wave vector is oriented mostly perpendicular to the ray paths, resulting in the wave fronts being tangents to the ray paths.

It is evident in Figure 5.11 that the mountain waves propagate northward up to an altitude of 35 km to 40 km. Also, the wave vectors turn slightly into east-west direction within the layer of small horizontal wind speeds between 20 and 40 km altitude (not shown). Above 40 km altitude the waves are refracted southward and the wave vectors change their horizontal direction such that they are pointing to the southwest. This refraction point is associated with increasing horizontal wind speeds due to the presence of the polar night jet south of New Zealand. Above the refraction point the gravity waves propagate downstream to the southeast towards the core of the polar night jet.

[2] A description of the method to derive the geostrophic winds from satellite data can be found in *Ern et al.* (2013).

[3] The temperature geostrophic wind fields were kindly provided by M. Ern

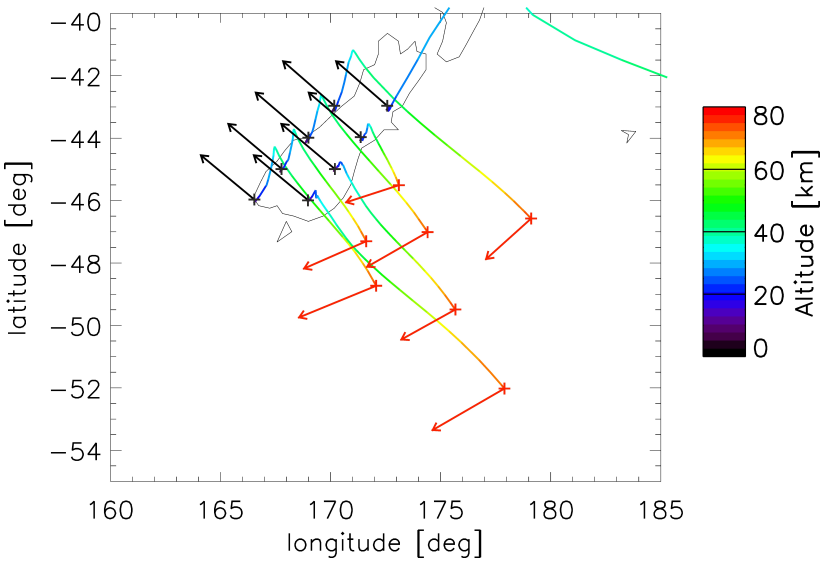

Figure 5.11: Ray traces as a function of altitude (color coded) above the Southern Island of New Zealand at 0000 UTC on 1 August 2014. Gravity waves were launched at 2.5 km altitude with the following set of parameters: $\lambda_h = 250\,\mathrm{km}$, $dir = 140°$, $c = 0\,\mathrm{m\,s^{-1}}$. The black (red) arrows represent the wave vector at the starting (end) point. The crosses mark the starting and end point.

5.3 Discussion

The results presented here indicate that mainly two mechanisms govern the propagation of large-amplitude mountain waves in the middle atmosphere above New Zealand between 31 July and 1 August 2014, as illustrated in Figure 5.12:

1. Gravity wave breaking, most likely due to dynamical instabilities occurring within the stratospheric minimum wind layer and

2. refraction of long-wavelength gravity waves and their subsequent propagation into the polar night jet south of New Zealand.

In the following the relevance of both mechanisms is discussed and their relative importance at different times during the event is evaluated.

The pronounced northwesterly tropospheric winds above New Zealand during 31 July and 1 August 2014 (Fig. 5.9a) provide continuously strong forcing conditions for orographic gravity waves. Additionally, the increase of the horizontal wind speed without significant directional shear, in combination with the elevated subtropical jet stream provides favorable conditions for the vertical propagation of mountain waves into the stratosphere. Lidar temperature perturbations show large-amplitude gravity waves

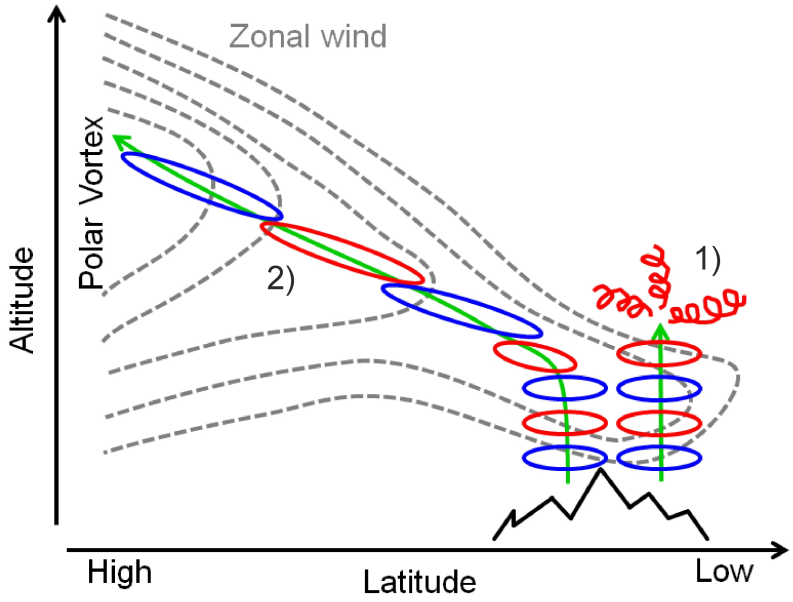

Figure 5.12: Sketch of the pathways of gravity wave propagation above New Zealand during 31 July and 1 August 2014 (green). 1) illustrates the effect of instabilities on the vertical propagation, while 2) marks the case where instabilities are absent and the propagational pathway is dominated by refraction.

with phase lines at constant altitude levels in the stratosphere. These are attributed to nearly stationary, vertically propagating mountain waves excited by the flow across the Southern Alps. The attribution to mountain waves is backed up by the ECMWF IFS, which simulates stationary patterns of horizontal convergence and divergence throughout the troposphere and the lowermost stratosphere, which are oriented parallel to the main mountain ranges of the Southern Alps of New Zealand (Fig. 5.7). These stationary patterns are generally associated with mountain waves (e.g *Alexander and Teitelbaum*, 2007). Furthermore, the observed vertical wavelength $\lambda_z \approx 4\,\mathrm{km}$ agrees very well with a linear estimate of the vertical wavelength of hydrostatic mountain waves propagating into a layer with $u \approx 10\,\mathrm{m\,s^{-1}}$ to $20\,\mathrm{m\,s^{-1}}$ and $N \approx 0.015\,\mathrm{s^{-1}}$ to $0.02\,\mathrm{s^{-1}}$.

A lower stratospheric E_p on 31 July compared to 1 August (Fig. 5.5) was derived. This difference is most likely the result of gravity wave breaking due to the occurrence of instabilities on 31 July. Comparing the temporal evolution of E_p on 31 July (Fig. 5.6a) and the ratio $|u'/\overline{u}|$ (Fig. 5.9b) one can see that the sudden decrease of E_p between 25 and 35 km altitude at the onset of episode 1) is associated with an increase of $|u'/\overline{u}|$ between 20 and 30 km altitude. This increase of $|u'/\overline{u}|$ is caused by the stronger tropospheric forcing of mountain waves, as a result of stronger tropospheric winds, and

the slightly reduced stratospheric winds after 1200 UTC (Fig. 5.9a). Thus, dynamical instabilities most likely control the gravity wave amplitudes in the stratosphere on 31 July 2014.

A different evolution can be observed on 1 August: At the start of episode 2) E_p at 35 km to 45 km altitude increases by a factor of 8 within in one hour (blue line in Fig. 5.6b). At the same time the ratio $|u'/\overline{u}|$ drops throughout the stratosphere. The decrease of $|u'/\overline{u}|$ is mostly caused by the reduction of the tropospheric winds after 1000 UTC on 1 August 2014: These weaker forcing conditions lead to smaller mountain wave amplitudes, which is also visible in the slightly reduced E_p values at 25 km to 35 km after the onset of episode 2). This suggests that the mountain waves can propagate to higher altitudes after 1600 UTC, while the vertical propagation into the upper stratosphere is limited by instabilities at earlier times. Note, that a thin layer of enhanced $|u'/\overline{u}|$ values is simulated at 35 km altitude after 1900 UTC on 1 August. The layer indicates a possible breaking region. However, no lidar observations exist to verify this assumption.

At this point it remains an open question, why no mountain waves are observed by the lidar above 45 km altitude after the onset of episode 2). One possibility is that the mountain waves simply break above 45 km altitude. However, there are no indications for instabilities in the ECMWF model at these altitudes. Furthermore, the raytracing simulations suggest that horizontal propagation plays a major role (Fig. 5.11): The stationary mountain waves launched at 2.5 km altitude remain localized above the Southern Island of New Zealand up to an altitude of ≈ 40 km where they are refracted and propagate quickly to the southeast. When the mountain waves leave the sounding volume of the lidar, they can no longer be observed by TELMA and a sudden drop of the measured E_p around 40 km to 50 km altitude is expected. This is consistent with the lidar observations on 1 August 2014.

The refraction of gravity waves around 45 km altitude and their subsequent propagation to the southeast can be understood by examining the raytracing equation of the meridional wavenumber (Eq. 2.26): The meridional shear of the zonal wind caused by the presence of the polar night jet south of New Zealand induces a change of the meridional wave number. This turns the wave vector to the southwest (cf. Fig. 5.11). As a result the horizontal group velocity is no longer completely compensated by the horizontal wind and the mountain waves propagate southeastward towards the center of the polar night jet (cf. Fig. 6 by *Sato et al.*, 2012).

To quantify the contribution of the refracted mountain waves to the middle atmospheric momentum budget, the momentum flux was calculated from the raytracing simulations. The raytracing simulations show a mean momentum flux of the refracted mountain waves at 70 km altitude of $20\,\mathrm{m^2\,s^{-2}}$. Satellite measurements show average momentum fluxes at 70 km altitude around 50° S during July of approximately $1\,\mathrm{m^2\,s{-}2}$ (*Ern et al.*, 2011). This is more than an order of magnitude smaller than the momentum flux of

the here analyzed refracted mountain waves. Thus, the here analyzed event is likely to have had a significant impact on the middle atmospheric momentum budget.

At this point no explanation can be given for the temperature perturbations observed by the lidar on 31 July and 1 August 2014, which are not associated with mountain waves. These small temperature fluctuations with short vertical extent, visible for example above 50 km altitude on 1 August (Fig. 5.4d), form a background wave activity, which appears throughout all our measurements in the absence of distinct wave patterns (c.f. right panel of Fig. 2 by *Kaifler et al.*, 2015b). More research is needed in order to quantify this background wave activity. One possibility for the particular gravity wave with a descending phase line around 50 km altitude on 31 July (Fig. 5.4c) is that it is not excited at New Zealand but simply propagates through our observational volume.

In summary, it is argued that both mechanisms – 1) breaking of gravity waves and 2) wave refraction – determine the propagation of gravity waves into the middle atmosphere during 31 July and 1 August 2014, as illustrated in Figure 5.12. The propagation through the lower stratosphere is, in this case, mainly governed by instabilities. This conclusion is in agreement with the picture drawn by *Kaifler et al.* (2015b) who stated that mountain waves can propagate to mesospheric altitudes under two conditions: 1) weak to moderate forcing conditions to avoid wave overturning and breaking at lower altitudes, and 2) sufficiently strong stratospheric wind speeds to avoid critical level filtering and to reduce the likeliness of instabilities.

The propagation pathway from the upper stratosphere into the mesosphere on 1 August 2014 was found to be governed by wave refraction. Above the refraction point (≈ 40 km altitude), the gravity waves propagated southeastward into the polar night jet. This process results in low mesospheric E_p observed by the lidar above New Zealand on 1 August 2014.

The here presented analysis focused only on the hydrostatic mountain waves with long horizontal wavelengths, which was motivated by the mountain waves simulated by the ECMWF IFS. However, aircraft observations during DEEPWAVE revealed a large fraction of mountain waves with short horizontal wavelengths ($\lambda_h \leq 100$ km) during several observational periods (*Smith et al.*, 2016). To investigate the possibility whether mountain waves with small λ_h contribute to the waves observed by TELMA or AIRS in the stratosphere, raytracing simulations with $\lambda_h \leq 100$ km were conducted (not shown). These shorter mountain waves show almost no horizontal propagation above the point of refraction. This is in agreement with *Sato et al.* (2012) who stated that refracted orographic waves with long horizontal wavelengths are advected over much larger horizontal distances, due to their lower vertical group velocity. Thus, the mountain waves with small λ_h can neither explain the gravity waves visible in the stratospheric AIRS observations south of 50° S (Fig. 5.10c), nor the sudden absence

of mountain waves above 45 km altitude in the lidar observations after the onset of episode 2).

Note, that the refracted mountain waves originating from New Zealand cannot explain the AIRS observations of gravity wave activity in the upper stratosphere south of 50° S. For one, the refraction occurs at altitudes too high to coincide with the AIRS observations. Additionally, the vertical wavelength of the refracted gravity waves remains roughly at 5 km to 8 km throughout the middle atmosphere and is thus considerably shorter than the AIRS visibility limit.

One possibility to explain the enhanced gravity waves activity observed by AIRS south of 50° S (Fig. 5.10c) are the upstream gravity waves visible e.g. in the ECMWF IFS horizontal divergence fields (Fig. 5.7) or the Hovmöller diagrams (Fig. 5.8). These wave packets are collocated with the tropospheric jet stream (cf. Fig. 5.8a,d) which passes over Tasmania and Southeast Australia before it turns southward towards New Zealand. Thus, it is likely that these waves are either orographic waves excited at Tasmania or Australia, or that they are associated with the unbalanced motions of the jet stream, or they constitute a superposition of both source processes. It is noteworthy that these waves do not propagate over the Southern Island of New Zealand but remain to the south over the ocean (cf. Fig. 5.8c,f). Hence, they cannot be observed by TELMA. As a consequence, the upstream gravity waves were not further investigated in this thesis.

5.4 Conclusion

A large-amplitude mountain wave event which occurred over New Zealand between 31 July and 1 August 2014 was investigated. Strong northwesterly winds in the troposphere excited intense mountain waves at the Southern Alps of New Zealand. The presence of the elevated subtropical jet stream extending across the dynamical tropopause into the lower stratosphere provided favorable conditions for the propagation of gravity waves into the stratosphere.

It was found that the propagation of mountain waves into the middle atmosphere during the analyzed period is determined by two factors: 1) Instabilities cause wave breaking and thus limit the propagation of mountain waves into the upper stratosphere at the beginning of the investigated period. 2) At later times, the mountain waves can propagate into the upper stratosphere, but are refracted by the strong meridional shear of the zonal wind and propagate downstream towards the polar night jet.

Thus, it is shown by a combination of observational data and simulations, that horizontal propagation of mountain waves originating at New Zealand is occurring in the atmosphere. Furthermore, the raytracing simulations showed mean momentum fluxes

of the refracted mountain waves of $20\,m^2\,s^{-2}$ at 70 km altitude, which is an order of magnitude larger than mean momentum flux values observed by satellites in that height and latitude region. Models relying on single-column gravity wave parametrization schemes deposit this momentum at 45° S, while the evidence presented in this thesis suggests a southward transport to at least 50° S.

At this point it remains an open question how important these horizontally propagating mountain waves are for the middle atmospheric momentum budget, in particular when it comes to the question of the missing gravity wave drag at 60° S (*McLandress et al.*, 2012). Points which have to be addressed to answer this question are, for example, how often do these horizontally propagating mountain waves occur, what is the total effect on the middle atmospheric momentum budget and what is the average distance these waves can propagate? The implied statistical analysis requires extensive observations at multiple sites, which are not available to date. Based on the case study presented here, it is likely that the horizontally propagating mountain waves contribute to a reduction of the problem of the missing gravity wave drag at 60° S. This reasoning is supported by a recent study of *Amemiya and Sato* (2016), who developed a new parametrization scheme which takes into account horizontal propagation of orographic gravity waves. With this new parametrization *Amemiya and Sato* (2016) were able to improve the representation of the southern hemispheric middle atmosphere in their model, proving that horizontally propagating gravity waves can improve the situation of the missing gravity wave drag at 60° S in current global atmospheric models.

A further implication of the here presented results concerns the interpretation of lidar measurements. When interpreting lidar measurements, horizontal propagation of gravity waves is often neglected. The here presented results indicate that horizontal propagation should be considered when it comes to interpreting lidar measurements. Otherwise, if a decrease of gravity wave potential energy with altitude is observed, it cannot be distinguished whether the gravity waves break or whether they propagate out of the observational volume.

6 Summary

By transporting energy and momentum, atmospheric gravity waves have a strong impact on global circulation patterns within the middle atmosphere. However, due to their small horizontal scales gravity waves cannot be resolved explicitly by many global atmospheric models. Therefore, the effect of gravity waves on the middle atmosphere has to be parametrized in most models. Due to limited computational resources these gravity wave parametrizations are largely simplified, e.g. it is assumed that gravity waves propagate purely in the vertical (so called single column approximation).

However, several recent studies showed simulations in which mountain waves were able to not only propagate vertically but also horizontally. Since these studies do not include any observations to prove the validity of the simulations for the real atmosphere, this thesis combined ground-based lidar observations and simulations to investigate the following hypothesis: "Mountain waves originating at New Zealand can propagate horizontally away from their source region into the polar night jet. This horizontal propagation results in a cross-meridional transport of gravity wave momentum flux."

This hypothesis was assessed with the help of ground-based lidar temperature measurements taken at Lauder, New Zealand (45.0° S, 169.7° E). Since several methods of extracting gravity waves from lidar measurements currently exist, the first question investigated in this thesis was

1) **Which method is most suitable to extract signatures of gravity waves from Rayleigh lidar temperature measurements?**

It was found that the most suitable method for this purpose is the application of a Butterworth filter in the vertical domain, because it is insensitive to measurements gaps and temporal resolution of the lidar data, and it covers a large part of the gravity wave spectrum, most importantly also including mountain waves.

Due to the measurement geometry of the lidar, horizontal propagation of gravity waves cannot be assessed based on lidar measurements alone. To investigate the horizontal domain, data from the integrated forecast system (IFS) of the European Centre for Medium-Range Weather Forecasts (ECMWF) was used. In order to identify the altitude region in which the ECMWF IFS can be regarded reliable, the ECMWF IFS was compared to lidar temperature measurements to investigate the second question

2) To what extent are middle atmospheric dynamics resolved by the ECMWF IFS?

It was found that over New Zealand the mean dynamical state of the ECMWF IFS is reliable up to 60 km altitude. For a high latitude site in Finland, good agreement was found up to 45 km altitude. Comparing the mean gravity wave activity simulated by the ECMWF IFS to lidar measurements, it was found that both agree well up to 45 km altitude. Above 45 km altitude resolved gravity waves are removed by the sponge layer of the ECMWF IFS. Within the height range of 30 km to 40 km, the ECMWF IFS is also capable of resolving the temporal development of gravity wave activity. Especially good agreement between the ECMWF IFS and the lidar data was found for a large amplitude mountain wave event over Lauder, New Zealand, on 1 August 2014, where even the phases of the observed mountain waves matched the phases simulated by the ECMWF IFS up to ≈ 50 km altitude.

As a consequence of the latter results, it was chosen to further investigate the mountain wave event over Lauder, New Zealand, around 1 August 2014, with a special focus on the third question

3) Do the large amplitude mountain waves exited above New Zealand during 31 July and 1 August 2014 propagate towards the south?

It was found that the propagation of mountain waves into the middle atmosphere during 31 July and 1 August 2014 was determined by two factors: 1) Instabilities caused wave breaking and thus limited the propagation of mountain waves into the upper stratosphere at the beginning of the investigated period. 2) At later times the mountain waves were able to propagate into the upper stratosphere, but were refracted by the strong meridional shear of the zonal wind. This caused the mountain waves to propagate horizontally over several degrees in latitude and longitude towards the polar night jet. Additionally, it was shown that the momentum flux of this mountain wave event at 70 km altitude was an order of magnitude larger than zonal mean values observed by satellites.

Thus, the hypothesis of this thesis "Mountain waves originating at New Zealand can propagate horizontally away from their source region into the polar night jet. This horizontal propagation results in a cross-meridional transport of gravity wave momentum flux" could be verified. However, the overall importance of this process for the middle atmospheric momentum budget still has to be investigated. It remains an open question how often situations comparable to the case studied in this thesis occur and how large the mean observed momentum flux is which is caused by the refracted mountain waves. Further observations are needed to answer these questions. One way to observe these processes is utilizing airborne Rayleigh lidar measurements conducted in the vicinity of the polar night jet. Such an airborne lidar system is

currently developed by the German Aerospace Center (DLR) and is scheduled to conduct such observations in the near future.

Bibliography

Alexander, M., and H. Teitelbaum (2007), Observation and analysis of a large amplitude mountain wave event over the Antarctic peninsula, *J. Geophys. Res.*, *112*, D21,103, doi:10.1029/2006JD008368.

Alexander, M., M. Geller, C. McLandress, S. Polavarapu, P. Preusse, F. Sassi, K. Sato, S. Eckermann, M. ern, A. hertzog, Y. Kawatani, M. Pulido, T. Shaw, M. Sigmond, R. Vincent, and S. Watanabe (2010), Recent developments in gravity-wave effects in climate models and the global distribution of gravity-wave momentum flux from observations and models, *Q. J. R. Meteorol. Soc.*, *136*, 1103–1124, doi:10.1002/qj.637.

Alexander, M. J., and A. W. Grimsdell (2013), Seasonal cycle of orographic gravity wave occurrence above small islands in the Southern Hemisphere: Implications for effects on the general circulation, *J. Geophys. Res.*, *118*(20), 11,589–11,599, doi:10.1002/2013jd020526.

Alexander, S., A. Klekociuk, and D. Murphy (2011), Rayleigh lidar observations of gravity wave activity in the winter upper stratosphere and lower mesosphere above Davis, Antarctica (69°S, 78°E), *J. Geophys. Res.*, *116*, D13,109, doi:10.1029/2010JD015164.

Amemiya, A., and K. Sato (2016), A New Gravity Wave Parameterization Including Three-Dimensional Propagation, *Journal of the Meteorological Society of Japan*, *94*(3), 237–256, doi:10.2151/jmsj.2016-013.

Aumann, H., M. Chahine, C. Autier, M. Goldberg, E. Kalnay, L. McMillin, H. Revercomb, P. Rosenkrant, W. Smith, D. Staelin, L. Strow, and J. Susskind (2003), AIRS/AMSU/HSB on the Aqua mission: Design, science objectives, data products, and processing systems, *IEEE Trans. Geosci. Remote Sens.*, *41*(2), 253–264.

Baldwin, M. P., and T. J. Dunkerton (2001), Stratospheric Harbingers of Anomalous Weather Regimes, *Science*, *294*(5542), 581–584, doi:10.1126/science.1063315.

Baldwin, M. P., L. J. Gray, T. J. Dunkerton, K. Hamilton, P. H. Haynes, W. J. Randel, J. R. Holton, M. J. Alexander, I. Hirota, T. Horinouchi, D. B. A. Jones, J. S. Kinnersley, C. Marquardt, K. Sato, and M. Takahashi (2001), The quasi-biennial oscillation, *Rev. Geophys.*, *39*(2), 179–229, doi:10.1029/1999rg000073.

Bauer, P., A. Thorpe, and G. Brunet (2015), The quiet revolution of numerical weather prediction, *Nature*, *525*, 47–55, doi:10.1038/nature14956.

Bechtold, P., N. Semane, P. Lopez, J.-P. Chaboureau, A. Beljaars, and N. Bormann (2014), Representing Equilibrium and Nonequilibrium Convection in Large-Scale Models, *J. Atmos. Sci.*, *71*(2), 734–753, doi:10.1175/jas-d-13-0163.1.

Becker, E. (2011), Dynamical Control of the Middle Atmosphere, *Space Sci. Rev.*, *168*(1-4), 283–314, doi:10.1007/s11214-011-9841-5.

Behrendt, A. (2005), *Temperature Measurements with Lidar, in LIDAR: Range–Resolved Optical Remote Sensing of the Atmosphere*, 1st ed., 273–321 pp., Springer.

Beljaars, A. C. M., A. R. Brown, and N. Wood (2004), A new parametrization of turbulent orographic form drag, *Quart. J. Roy. Meteor. Soc.*, *130*(599), 1327–1347, doi:10.1256/qj.03.73.

Blum, U., K. H. Fricke, G. Baumgarten, and A. Schöch (2004), Simultaneous lidar observations of temperatures and waves in the polar middle atmosphere on the east and west side of the Scandinavian mountains: A case study on 19/20 January 2003, *Atmos. Chem. Phys.*, *4*, 809–816, doi:10.5194/acpd-4-969-2004.

Bölöni, G., B. Ribstein, J. Muraschko, C. Sgoff, J. Wei, and U. Achatz (2016), The Interaction between Atmospheric Gravity Waves and Large-Scale Flows: An Efficient Description beyond the Nonacceleration Paradigm, *J. Atmos. Sci.*, *73*(12), 4833–4852, doi:10.1175/jas-d-16-0069.1.

Brasseur, G., and S. Solomon (2005), *Aeronomy of the Middle Atmosphere*, 1402032846, 3rd ed., Springer.

Bretherton, F., and C. Garrett (1969), Wavetrains in inhomogeneous moving media, *Proc. R. Soc. London*, *A 302*, 529–554.

Chane-Ming, F., F. Molinaro, J. Leveau, P. Keckhut, and A. Hauchecorne (2000), Analysis of gravity waves in the tropical middle atmosphere over La Reunion Island (21°S, 55°E) with lidar using wavelet techniques, *Ann. Geophys.*, *18*, 485–498, doi:10.1007/s00585-000-0485-0.

Chanin, M.-L., and A. Hauchecorne (1981), Lidar observation of gravity and tidal waves in the stratosphere and mesosphere, *J. Geophys. Res.*, *86*(C10), 9715–9721.

Charney, J. G., and P. G. Drazin (1961), Propagation of planetary-scale disturbances from the lower into the upper atmosphere, *J. Geophys. Res.*, *66*(1), 83–109, doi:10.1029/jz066i001p00083.

Cohen, N. Y., E. P. Gerber, and O. Bühler (2014), What Drives the Brewer–Dobson Circulation?, *J. Atmos. Sci.*, *71*(10), 3837–3855, doi:10.1175/jas-d-14-0021.1.

Dörnbrack, A., S. Gisinger, M. C. Pitts, L. R. Poole, and M. Maturilli (2016), Multilevel cloud structures over Svalbard, *Mon. Wea. Rev.*, doi:10.1175/mwr-d-16-0214.1.

Duck, T., J. Whiteway, and A. Carswell (2001), The Gravity Wave-Arctic Stratospheric Vortex Interaction, *J. Atmos. Sci.*, *58*, 3581–3596.

Dunkerton, T. (1984), Inertia-gravity waves in the stratosphere, *J. Atmos. Sci.*, *41*(23), 3396–3404.

Eckermann, S. D., and C. J. Marks (1996), An idealized ray model of gravity wave-tidal interactions, *J. Geophys. Res.*, *101*(D16), 21,195–21,212, doi:10.1029/96jd01660.

Eckermann, S. D., D. Broutman, J. Ma, J. D. Doyle, P.-D. Pautet, M. J. Taylor, K. Bossert, B. P. Williams, D. C. Fritts, and R. B. Smith (2016), Dynamics of Orographic Gravity Waves Observed in the Mesosphere over the Auckland Islands during the Deep Propagating Gravity Wave Experiment (DEEPWAVE), *J. Atmos. Sci.*, *73*(10), 3855–3876, doi:10.1175/jas-d-16-0059.1.

Ehard, B., P. Achtert, and J. Gumbel (2014), Long-term lidar observations of wintertime gravity wave activity over northern Sweden, *Ann. Geophys.*, *32*, 1395–1405, doi:10.5194/angeo-32-1395-2014.

Ehard, B., B. Kaifler, N. Kaifler, and M. Rapp (2015), Evaluation of methods for gravity wave extraction from middle-atmospheric lidar temperature measurements, *Atmos. Meas. Tech.*, *8*(11), 4645–4655, doi:10.5194/amt-8-4645-2015.

Ehard, B., P. Achtert, A. Dörnbrack, S. Gisingar, J. Gumbel, M. Khaplanov, M. Rapp, and J. Wagner (2016), Combination of lidar and model data for studying deep gravity wave propagation, *Mon. Wea. Rev.*, *144*(1), 77–98, doi:10.1175/MWR-D-14-00405.1.

Ehard, B., B. Kaifler, A. Dörnbrack, P. Preusse, S. Eckermann, M. Bramberger, S. Gisinger, N. Kaifler, B. Liley, J. Wagner, and M. Rapp (2017), Horizontal propagation of large-amplitude mountain waves into the polar night jet, *J. Geophys. Res.*, doi:10.1002/2016JD025621.

Ern, M., P. Preusse, J. C. Gille, C. L. Hepplewhite, M. G. Mlynczak, J. M. Russell, and M. Riese (2011), Implications for atmospheric dynamics derived from global observations of gravity wave momentum flux in stratosphere and mesosphere, *J. Geophys. Res.*, *116*(D19), doi:10.1029/2011jd015821.

Ern, M., P. Preusse, S. Kalisch, M. Kaufmann, and M. Riese (2013), Role of gravity waves in the forcing of quasi two-day waves in the mesosphere: An observational study, *J. Geoph. Res. Atmos.*, *118*, 3467–3485, doi:10.1029/2012JD018208.

Fritts, D., and M. Alexander (2003), Gravity wave dynamics and effects in the middle atmosphere, *Rev. Geophys.*, *41(1)*, 1003, doi:10.1029/2001RG000106.

Fritts, D., R. Smith, M. Taylor, J. Doyle, S. E. A. Dörnbrack, M. Rapp, B. Williams, P.-D. Pautet, K. Bossert, N. Criddle, C. Reynolds, P. Reinecke, M. Uddstrom, M. Revell, R. Turner, B. Kaifler, J. Wagner, T. Mixa, C. Kruse, A. Nugent, C. Watson, S. Gisinger, S. Smith, J. Moore, W. Brown, J. Haggerty, A. Rockwell, B. Stossmeister, S. Williams, G. Hernandez, D. Murphy, A. Klekociuk, I. Reid, and J. Ma (2016), The Deep Gravity Wave Experiment (DEEPWAVE): An Airborne and Ground-Based Exploration of Gravity Wave Propagation and Effects from their Sources throughout the Lower and Middle Atmosphere, *Bull. Amer. Meteorol. Soc.*, *97*(3), 425–453, doi:10.1175/BAMS-D-14-00269.1.

Fritts, D. C., and P. K. Rastogi (1985), Convective and dynamical instabilities due to gravity wave motions in the lower and middle atmosphere: Theory and observations, *Radio Sci.*, *20*(6), 1247–1277, doi:10.1029/rs020i006p01247.

Gardner, C. S., M. S. Miller, and C. H. Liu (1989), Rayleigh Observations of Gravity Wave Activity in the Upper Stratosphere at Urbana, Ilinois, *J. Atmos. Sci.*, *46*(12), 1838–1854.

Gerber, E. P., A. Butler, N. Calvo, A. Charlton-Perez, M. Giorgetta, E. Manzini, J. Perlwitz, L. M. Polvani, F. Sassi, A. A. Scaife, T. A. Shaw, S.-W. Son, and S. Watanabe (2012), Assessing and Understanding the Impact of Stratospheric Dynamics and Variability on the Earth System, *Bull. Amer. Meteor. Soc.*, *93*(6), 845–859, doi:10.1175/bams-d-11-00145.1.

Gisinger, S., A. Dörnbrack, V. Matthias, J. Doyle, S. Eckermann, B. Ehard, L. Hoffmann, B. Kaifler, C. Kruse, and M. Rapp (2017), Atmospheric Conditions during the Deep Propagating Wave Experiment (DEEPWAVE), *Mon. Wea. Rev.*, submitted.

Gong, J., D. Wu, and S. Eckermann (2012), Gravity wave variances and propagation derived from AIRS radiances, *Atmos. Chem. Phys.*, *12*, 1701–1720, doi:10.5194/acp-12-1701-2012.

Hamilton, K., R. J. Wilson, and R. S. Hemler (1999), Middle Atmosphere Simulated with High Vertical and Horizontal Resolution Versions of a GCM: Improvements in the Cold Pole Bias and Generation of a QBO-like Oscillation in the Tropics, *J. Atmos. Sci.*, *56*(22), 3829–3846, doi:10.1175/1520-0469(1999)056<3829:maswhv>2.0.co;2.

Hasha, A., O. Bühler, and J. Scinocca (2008), Gravity Wave Refraction by Three-Dimensionally Varying Winds and the Global Transport of Angular Momentum, *J. Atmos. Sci.*, *65*(9), 2892–2906, doi:10.1175/2007jas2561.1.

Hauchecorne, A., and M. Chanin (1980), Density and temperature profiles obtained by lidar between 35 and 70 km, *Geophys. Res. Lett.*, *7*, 565–568, doi:10.1029/GL007i008p00565.

Hendricks, E. A., J. D. Doyle, S. D. Eckermann, Q. Jiang, and P. A. Reinecke (2014), What Is the Source of the Stratospheric Gravity Wave Belt in Austral Winter?, *Journal of the Atmospheric Sciences*, *71*(5), 1583–1592, doi:10.1175/jas-d-13-0332.1.

Hindley, N. P., C. J. Wright, N. D. Smith, and N. J. Mitchell (2015), The southern stratospheric gravity wave hot spot: individual waves and their momentum fluxes measured by COSMIC GPS-RO, *Atmos. Chem. Phys.*, *15*(14), 7797–7818, doi:10.5194/acp-15-7797-2015.

Hoffmann, L., and M. Alexander (2009), Retrieval of stratospheric temperatures from Atmospheric Infrared Sounder radiance measurements for gravity wave studies, *J. Geophys. Res.*, *114*(D7), doi:10.1029/2008jd011241.

Hoffmann, L., X. Xue, and M. Alexander (2013), A global view of stratospheric gravity wave hotspots located with Atmospheric Infrared Sounder observations, *J. Geophys. Res. Atmos.*, *118*, 416–434, doi:10.1029/2012JD018658.

Hoffmann, L., A. W. Grimsdell, and M. J. Alexander (2016), Stratospheric gravity waves at Southern Hemisphere orographic hotspots: 2003–2014 AIRS/Aqua observations, *Atmos. Chem. Phys.*, *16*(14), 9381–9397, doi:10.5194/acp-16-9381-2016.

Hoffmann, P., E. Becker, W. Singer, and M. Placke (2010), Seasonal variation of mesospheric waves at northern middle and high latitudes, *J. Atmos. Solar-Terr. Phys.*, *72*, 1068–1079, doi:10.1016/j.jastp.2010.07.002.

Hólm, E., R. Forbes, S. Lang, L. Magnusson, and S. Malardel (2016), New model cycle brings higher resolution, *ECMWF Newsletter*, *147*, 14–19.

Holton, J., and M. Alexander (2000), The role of waves in the transport circulation of the middle atmosphere, *Geophys. Monogr.*, *123*, 21–35, doi:10.1029/GM123p0021.

Jewtoukoff, V., A. Hertzog, R. Plougonven, A. de la Camara, and F. Lott (2015), Comparison of gravity waves in the southern hemisphere derived from balloon observations and the ECMWF analyses, *J. Atmos. Sci.*, *72*(9), 3449–3468, doi:10.1175/JAS-D-14-0324.1.

Jiang, J., S. Eckermann, D. Wu, K. Hocke, B. Wang, J. Ma, and Y. Zhang (2005), Seasonal variation of gravity wave sources from satellite observation, *Adv. Space Res.*, *35*, 1925–1932, doi:10.1016/j.asr.2005.01.099.

Jiang, Q., J. Doyle, and A. Reinecke (2013), A modeling study of stratospheric waves over the southern andes and drake passage, *J. Atmos. Sci.*, *70*, 1668–1689, doi:10.1175/JAS-D-12-0180.1.

Kaifler, B., F.-J. Lübken, J. Höffner, R. Morris, and T. P. Viehl (2015a), Lidar observations of gravity wave activity in the middle atmosphere over Davis (69°S, 78°E), Antarctica, *J. Geophys. Res. Atmos.*, *120*(10), 4506–4521, doi:10.1002/2014JD022879.

Kaifler, B., N. Kaifler, B. Ehard, A. Dörnbrack, M. Rapp, and D. Fritts (2015b), Influences of source conditions on mountain wave penetration into the stratosphere and mesosphere, *Geophys. Res. Lett.*, *42*, 9488–9494, doi:10.1002/2015GL066465.

Kaifler, N., B. Kaifler, B. Ehard, S. Gisinger, A. Dörnbrack, M. Rapp, R. Kivi, A. Kozlovsky, M. Lester, and B. Liley (2017), Observational indications of downward-propagating gravity waves in middle atmosphere lidar data, *J. Atmos. Solar-Terr. Phys.*, revised.

Kidston, J., A. A. Scaife, S. C. Hardiman, D. M. Mitchell, N. Butchart, M. P. Baldwin, and L. J. Gray (2015), Stratospheric influence on tropospheric jet streams, storm tracks and surface weather, *Nature Geosci.*, *8*(6), 433–440, doi:10.1038/ngeo2424.

Le Pichon, A., J. Assink, P. Heinrich, E. Blanc, A. Charlton-Perez, C. Lee, P. Keckhut, A. Hauchecorne, R. Rüfenacht, N. Kämpfer, D. Drob, P. Smets, L. Evers, L. Ceranna, C. Pilger, O. Ross, and C. Claud (2015), Comparison of co-located independent ground-based middle atmospheric wind and temperature measurements with numerical weather prediction models, *J. Geophys. Res. Atmos.*, *120*(16), 8318–8331, doi:10.1002/2015JD023273.

Lighthill, J. (1978), *Waves in fluids*, 1st ed., University Press, Cambridge.

Lindzen, R. (1981), Turbulence and stress owing to gravity wave and tidal breakdown, *J. Geophys. Res.*, *86*, 9707–9714, doi:10.1029/JC086iC10p09707.

Lott, F., and M. J. Miller (1997), A new subgrid-scale orographic drag parametrization: Its formulation and testing, *Quart. J. Roy. Meteor. Soc.*, *123*(537), 101–127, doi:10.1002/qj.49712353704.

Lübken, F.-J., J. Höffner, T. Viehl, B. Kaifler, and R. Morris (2011), First measurements of thermal tides in the summer mesopause region at Antarctic latitudes, *Geophys. Res. Lett*, *38*, L24,806, doi:10.1029/2011GL050045.

Malardel, S., and N. P. Wedi (2016), How does subgrid-scale parametrization influence nonlinear spectral energy fluxes in global NWP models?, *J. Geophys. Res.*, *121*(10), 5395–5410, doi:10.1002/2015JD023970.

Marks, C., and S. Eckermann (1995), A three-dimensional nonhydrostatic ray-tracing model for gravity waves: formulation and preliminary results for the middle atmosphere, *J. Atmos. Sci.*, *52*(11), 1959–1984, doi:10.1175/1520-0469(1995)052<1959:ATDNRT>2.0.CO;2.

McLandress, C. (1998), On the importance of gravity waves in the middle atmosphere and their parameterization in general circulation models, *J. Atmos. Solar-Terr. Phys.*, *60*(14), 1357–1383, doi:10.1016/s1364-6826(98)00061-3.

McLandress, C., T. G. Shepherd, S. Polavarapu, and S. R. Beagley (2012), Is Missing Orographic Gravity Wave Drag near 60°S the Cause of the Stratospheric Zonal Wind Biases in Chemistry–Climate Models?, *J. Atmos. Sci.*, *69*(3), 802–818, doi:10.1175/jas-d-11-0159.1.

Mzé, N., A. Hauchecorne, P. Keckhut, and M. Thetis (2014), Vertical distribution of gravity wave potential energy from long-term Rayleigh lidar data at a northern middle-latitude site, *J. Geoph. Res. Atmos.*, *119*(21), 12,069–12,083, doi:10.1002/2014JD022035.

Nappo, C. J. (2002), *An Introduction to Atmospheric Gravity Waves*, 2nd ed., Academic Press.

Orr, A., P. Bechtold, J. Scinocca, M. Ern, and M. Janiskova (2010), Improved Middle Atmosphere Climate and Forecasts in the ECMWF Model through a Nonorographic Gravity Wave Drag Parameterization, *J. Climate*, *23*(22), 5905–5926, doi:10.1175/2010jcli3490.1.

Plougonven, R., and H. Teitelbaum (2003), Comparison of a large-scale inertia-gravity wave as seen in the ECMWF analyses and from radiosondes, *Geophys. Res. Lett*, *30*(18), 1954, doi:10.1029/2003GL017716.

Plougonven, R., and F. Zhang (2014), Internal gravity waves from atmospheric jets and fronts, *Rev. Geophys.*, *52*(1), 33–76, doi:10.1002/2012RG000419.

Plougonven, R., A. de la Cámara, V. Jewtoukoff, A. Hertzog, and F. Lott (2017), On the relation between gravity waves and wind speed in the lower stratosphere over the Southern Ocean, *J. Atmos. Sci.*, doi:10.1175/jas-d-16-0096.1.

Preusse, P., A. Dörnbrack, S. Eckermann, M. Riese, B. Schaeler, J. Bacmeister, D. Broutman, and K. Grossmann (2002), Space-based measurements of stratospheric mountain waves by CRISTA 1. Sensitivity, analysis method, and a case study, *J. Geoph. Res.*, *107*(D23), 8178, doi:10.1029/2001JD000699.

Preusse, P., S. Eckermann, M. Ern, J. Oberheide, R. Picard, R. Roble, G. Riese, J. Russell III, and M. Mlynczak (2009), Global ray tracing simulations of the SABER gravity wave climatology, *J. Geophys. Res.*, *114*(D8), doi:10.1029/2008JD011214.

Preusse, P., M. Ern, P. Bechtold, S. Eckermann, S. Kalisch, Q. Trinh, and M. Riese (2014), Characteristics of gravity waves resolved by ECMWF, *Atmos. Chem. Phys.*, *14*, 10,483–10,508, doi:10.5194/acp-14-10483-2014.

Rauthe, M., M. Gerding, J. Höffner, and F.-J. Lübken (2006), Lidar temperature measurements of gravity waves over Kühlungsborn (54°N) from 1 to 105 km: A winter-summer comparison, *J. Geophys. Res.*, *111*, D24,108, doi:10.1029/2006JD007354.

Rauthe, M., M. Gerding, and F.-J. Lübken (2008), Seasonal changes in gravity wave activity measured by lidars at mid-latitudes, *Atmos. Chem. Phys.*, *8*, 6775–6787, doi:10.5194/acp-8-6775-2008.

Remsberg, E. E., B. T. Marshall, M. Garcia-Comas, D. Krueger, G. S. Lingenfelser, J. Martin-Torres, M. G. Mlynczak, J. M. Russell, A. K. Smith, Y. Zhao, C. Brown, L. L. Gordley, M. J. Lopez-Gonzalez, M. Lopez-Puertas, C.-Y. She, M. J. Taylor, and R. E. Thompson (2008), Assessment of the quality of the Version 1.07 temperature-versus-pressure profiles of the middle atmosphere from TIMED/SABER, *J. Geophys. Res.*, *113*(D17), doi:10.1029/2008jd010013.

Sato, K., S. Watanabe, Y. Kawatani, Y. Tomikawa, K. Miyazaki, and M. Takahashi (2009), On the origins of mesospheric gravity waves, *Geophys. Res. Lett.*, *36*, L19,801, doi:10.1029/2009GL039908.

Sato, K., S. Tateno, S. Watanabe, and Y. Kawatani (2012), Gravity wave characteristics in the southern hemisphere revealed by a high-resolution middle-atmospheric general circulation model, *J. Atmos. Sci.*, *69*, 1378–1396, doi:10.1175/JAS-D-11-0101.1.

Schroeder, S., P. Preusse, M. Ern, and M. Riese (2009), Gravity waves resolved in ECMWF and measured by SABER, *Geophys. Res. Lett.*, *36*, L10,805, doi:10.1029/2008GL037054.

Sica, R., and A. Haefele (2015), Retrieval of temperature from a multiple-channel rayleigh-scatter lidar using optimal estimation method, *Appl. Opt.*, *54*(8), 1872–1889, doi:10.1364/AO.54.001872.

Smith, R., A. Nugent, C. Kruse, D. Fritts, J. Doyle, S. E. M. Taylor, A. Dörnbrack, M. Uddstrom, W. Cooper, P. Romashkin, J. Jensen, and S. Beaton (2016), Stratospheric gravity wave fluxes and scales during DEEPWAVE, *J. Atmos. Sci.*, *73*(7), 2851–2869, doi:10.1175/JAS-D-15-0324.1.

Sutherland, B. (2010), *Internal Gravity Waves*, 1st ed., Cambridge University Press.

Tiedtke, M. (1989), A Comprehensive Mass Flux Scheme for Cumulus Parameterization in Large-Scale Models, *Mon. Wea. Rev.*, *117*(8), 1779–1800, doi:10.1175/1520-0493(1989)117<1779:acmfsf>2.0.co;2.

Warner, C. D., and M. E. McIntyre (1996), On the Propagation and Dissipation of Gravity Wave Spectra through a Realistic Middle Atmosphere, *Journal of the Atmospheric Sciences*, *53*(22), 3213–3235, doi:10.1175/1520-0469(1996)053<3213:otpado>2.0.co;2.

Waters, J., L. Froidevaux, R. Harwood, R. Jarnot, H. Pickett, W. Read, P. Siegel, R. Cofield, M. Filipiak, D. Flower, J. Holden, G. Lau, N. Livesey, G. Manney, H. Pumphrey, M. Santee, D. Wu, D. Cuddy, R. Lay, M. Loo, V. Perun, M. Schwartz, P. Stek, R. Thurstans, M. Boyles, K. Chandra, M. Chavez, G.-S. Chen, B. Chudasama,

R. Dodge, R. Fuller, M. Girard, J. Jiang, Y. Jiang, B. Knosp, R. LaBelle, J. Lam, K. Lee, D. Miller, J. Oswald, N. Patel, D. Pukala, O. Quintero, D. Scaff, W. V. Snyder, M. Tope, P. Wagner, and M. Walch (2006), The Earth observing system microwave limb sounder (EOS MLS) on the aura Satellite, *IEEE Trans. Geosci. Remote Sens.*, *44*(5), 1075–1092, doi:10.1109/tgrs.2006.873771.

Weitkamp, C. (2005), *LIDAR: range-resolved optical remote sensing of the atmosphere*, Springer.

Whiteway, J., T. Duck, D. Donovan, J. Bird, S. Pal, and A. Carswell (1997), Measurements of gravity wave activity within and around the Arctic stratospheric vortex, *Geophys. Res. Lett.*, *24*(11), 1387–1390.

Whiteway, J. A., and A. I. Carswell (1995), Lidar observations of gravity wave activity in the upper stratosphere over Toronto, *J. Geophys. Res.*, *100*, 14,113–14,124, doi:10.1029/95JD00511.

Wilson, R., M. Chanin, and A. Hauchecorne (1991), Gravity waves in the middle atmosphere observed by Rayleigh lidar: 2. Climatology, *J. Geophys. Res.*, *96*(D3), 5169–5183, doi:10.1029/90JD02231.

Wu, D., and S. Eckermann (2008), Global Gravity Wave Variances from Aura MLS: Characteristics and Interpretation, *J. Atmos. Sci.*, *65*(12), 3695–3718, doi:10.1175/2008JAS2489.1.

Yamashita, C., X. Chu, H. Liu, P. J. Espy, G. J. Nott, and W. Huang (2009), Stratospheric gravity wave characteristics and seasonal variations observed by lidar at the South Pole and Rothera, Antarctica, *J. Geophys. Res.*, *114*, D12,101, doi:10.1029/2008JD011472.

Acknowledgments

First and foremost, my thanks go to Markus Rapp for the supervision of this thesis. Thank you for your support, encouragement and for focusing the scientific aim of my thesis. I am particularly grateful for all the opportunities to participate in international measurement campaigns and to visit several international conferences, workshops and the FDSE summer school in Cambridge.

This thesis would not have been possible without the support of Bernd Kaifler. Thank you for answering all my questions, for reading my articles over and over again and for putting me back on track when I needed it.

Moreover I want to thank Andreas Dörnbrack for the many scientific discussions we had, for showing me the exciting world of numerical simulations and most of all for getting me into contact with so many colleagues at various conferences.

My thanks also go to Peter Preusse for the quick answers to my questions regarding the GROGRAT model and to Sylvie Malardel for the discussions regarding the ECMWF IFS model and for conducting the testruns with the ECMWF IFS.

I am grateful for the support of the NIWA staff at Lauder who made the 4 months in New Zealand a very pleasant time. My special thanks go to Ayoe Buus Hansen and Wills Dobson: without you I wouldn't have lasted that long down there!

Furthermore, I want to thank the entire middle atmosphere group at DLR: Thank you for the countless scientific discussions and the joyful times together at various conferences.

Thanks also to the entire Lidar group at DLR who made the coffee break a very interesting and refreshing time of the day.

Special thanks go to my past and present office mates: Thanks for all the work related discussions and the equally important slightly off-topic talks we had!

Last, but not least, I want to thank my friends and family who supported me throughout my studies.